

STUDIES OF ^1H NUCLEAR MAGNETIC RESONANCE
RELAXATION IN HUMAN CORTICAL BONE:
FROM *EX VIVO* SPECTROSCOPY TO
CLINICAL IMAGING METHODS

By

R. Adam Horch

Dissertation

Submitted to the Faculty of the
Graduate School of Vanderbilt University
in partial fulfillment of the requirements

for the degree of

DOCTOR OF PHILOSOPHY

in

Biomedical Engineering

December, 2011

Nashville, Tennessee

Approved By:

Mark D. Does, Ph. D., Chair

Jeffrey S. Nyman, Ph. D.

Daniel F. Gochberg, Ph. D.

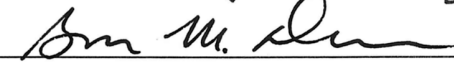
Bruce M. Damon, Ph. D.

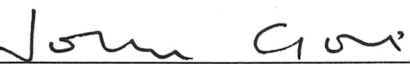
John C. Gore, Ph. D.











Date:

11/9/2011

11/9/2011

11/9/2011

11/9/2011

11-9-11

Copyright © 2011 by Robert Adam Horch

All Rights Reserved

Dedicated to my Mother, my center, and my guide,

Frances Ybañez Horch

ACKNOWLEDGEMENTS

I am immeasurably grateful to Mark D. Does, Jeffry S. Nyman, Daniel F. Gochberg, John C. Gore, Richard D. Dortch, and Ken Wilkens, whose valuable insights and contributions made this work possible. Additionally, I am grateful to Morgan Evans (LaVergne High School) and Troy Brown (Vanderbilt University, Class of 2011), whose summertime laboratory assistance was instrumental to the timely progression of this work. I would like to thank Sasidhar Tadanki (Vanderbilt University) for numerous insights on RF coil design, and the countless others at the Vanderbilt University Institute for Imaging Science who have made my time here the best of my life.

Finally, this work would not have been possible without generous financial support from: the NIH, Grant # EB001744 & EB001452; the NSF, Grant # 0448915; the Vanderbilt University Discovery Grant Program; the National Science Foundation's Graduate Student Fellowship Program; and the Department of Defense's National Defense Science and Engineering Graduate Fellowship, Air Force Office of Scientific Research 32 CFR 168a.

TABLE OF CONTENTS

	Page
ACKNOWLEDGEMENTS.....	iv
LIST OF TABLES.....	ix
LIST OF FIGURES.....	x
INTRODUCTION.....	xii
CHAPTER 1 The Case for Clinical Magnetic Resonance Imaging of Human Cortical Bone.....	1
1.1 — <i>Cortical Bone Micro-anatomy: The Biophysical Bases for Bone Imaging</i>	2
1.2 — <i>Cortical Bone Imaging in Today's Clinic</i>	5
1.3 — <i>Assessing Fracture Resistance: Going Beyond X-rays and Bone Mineral Content</i>	9
1.4 — <i>Potential for MRI-based Cortical Bone Diagnostic Imaging</i>	13
1.5 — <i>References</i>	16
CHAPTER 2 Prerequisites for Nuclear Magnetic Resonance of Cortical Bone.....	24
2.1 — <i>Background and Introduction: The RF Coil Problem</i>	25
2.2 — <i>Experimental Methods: NMR Measurements and Coil Designs</i>	27
2.3 — <i>Experimental Findings: RF Coil Background Signals and Self- portraits</i>	32
2.4 — <i>Discussion: Considerations of Coil Materials and Placement</i>	37
2.5 — <i>Conclusions</i>	41
2.6 — <i>References</i>	43

CHAPTER 3	Biophysical Basis of Transverse Relaxation in Cortical Bone.....	45
3.1	— <i>Background and Introduction: A Basis for Bone NMR</i>	45
3.2	— <i>Experimental Methods: Human cortical bone preparation</i>	47
3.3	— <i>Experimental Methods: Micro-computed tomography (μCT)</i>	48
3.4	— <i>Experimental Methods: NMR measurements</i>	49
3.5	— <i>Experimental Methods: NMR Data Fitting</i>	52
3.6	— <i>Experimental Findings: Decomposition of the Bulk Bone NMR Signal</i>	53
3.7	— <i>Discussion: Micro-anatomical Origins of Bone NMR Signals</i>	59
3.8	— <i>Conclusions</i>	65
3.9	— <i>References</i>	67
CHAPTER 4	Biomechanical Significance of the Cortical Bone T_2 Distribution.....	70
4.1	— <i>Background and Introduction: The Material Role of Bone NMR</i>	70
4.2	— <i>Experimental Methods: Human cortical bone processing</i>	72
4.3	— <i>Experimental Methods: NMR</i>	73
4.4	— <i>Experimental Methods: μCT</i>	75
4.5	— <i>Experimental Methods: Mechanical Testing</i>	76
4.6	— <i>Experimental Findings: Correlates to Mechanical Properties</i>	77
4.7	— <i>Discussion: Potential for MRI-based Fracture Risk Assessment</i>	82
4.8	— <i>Conclusions</i>	85
4.9	— <i>References</i>	86

CHAPTER 5	Clinical Methods for Bound/Pore Water-discriminated Imaging of Cortical Bone.....	88
5.1	— <i>Background and Introduction: The Need for Bound/Pore Water Discrimination.....</i>	89
5.2	— <i>Theory: A Model for the NMR Lineshape of Water in Cortical Bone.....</i>	90
5.3	— <i>Theory: T₂ Selective Adiabatic RF pulses.....</i>	92
5.4	— <i>Theory: Ultra-short Echo Time Pulse Sequences.....</i>	94
5.5	— <i>Theory: Double Adiabatic Full Passage (DAFP) Pulse Sequence.....</i>	97
5.6	— <i>Theory: Adiabatic Inversion Recovery (AIR) Pulse Sequence.....</i>	98
5.7	— <i>Theory: Absolute Water Concentration.....</i>	99
5.8	— <i>Experimental Methods Overview.....</i>	100
5.9	— <i>Experimental Methods: Human cortical bone preparation.....</i>	100
5.10	— <i>Experimental Methods: Mechanical Testing.....</i>	101
5.11	— <i>Experimental Methods: NMR.....</i>	102
5.12	— <i>Experimental Methods: Data Analysis.....</i>	104
5.13	— <i>Experimental Findings.....</i>	108
5.14	— <i>Discussion (overview).....</i>	116
5.15	— <i>Discussion: A Model for Bound and Pore Water Transverse Relaxation in Human Cortical Bone.....</i>	117
5.16	— <i>Discussion: Current Bone MRI Methods with Non-selective Imaging.....</i>	118
5.17	— <i>Discussion: AFP Pulses for Bound Water Selection.....</i>	119
5.18	— <i>Discussion: DAFP for Pore Water-Selective Imaging.....</i>	120
5.19	— <i>Discussion: AIR for Bound Water-Selective Imaging.....</i>	121
5.20	— <i>Discussion: Correlations to Mechanical Properties.....</i>	122
5.21	— <i>Conclusions.....</i>	124
5.22	— <i>References.....</i>	125
CHAPTER 6	The Future of Cortical Bone Magnetic Resonance.....	130
6.1	— <i>Whole Bone Fracture Assessment.....</i>	131
6.2	— <i>Bone Matrix MRI: Going Beyond Mechanical Properties.....</i>	133
6.3	— <i>Requirements for Practical Cortical Bone MRI in the Clinic.....</i>	136
6.4	— <i>Final Thoughts.....</i>	138
6.5	— <i>References.....</i>	139

APPENDIX I	Experiences with High Power Loop-gap RF Coil	
	Design and Bench Testing.....	141
AI.1	— <i>Coil Selection and Design</i>	141
AI.2	— <i>Tuning, Matching, and Balancing on the Bench-top</i>	144
AI.3	— <i>Final Checks</i>	150
AI.4	— <i>References</i>	151
APPENDIX II	Considerations for Processing Human Cortical Bone	
	Tissue.....	152
APPENDIX III	Applying Cortical Bone Water Characterization	
	Methods to Other Tissues: A Case Study of	
	Myelinated Nerves.....	158
AIII.1	— <i>Background and Introduction</i>	158
AIII.2	— <i>Experimental Methods: NMR</i>	160
AIII.3	— <i>Experimental Methods: Nerve Tissue Processing</i>	162
AIII.4	— <i>Experimental Methods: Tissue Phantom Preparations</i>	164
AIII.5	— <i>Experimental Findings</i>	165
AIII.6	— <i>Discussion: Ultrashort-T_{2s} from the Myelin Membranes</i>	173
AIII.7	— <i>Conclusions</i>	182
AIII.8	— <i>Acknowledgements</i>	182
AIII.9	— <i>References</i>	183

LIST OF TABLES

	Page	
TABLE 2.1	Material selections in the three loop-gap coil variants.....	31
TABLE 2.2	Sources of background signal in different loop-gap configurations.....	33
TABLE 4.1	Summary of Pearson's r^2 for pairwise correlations between imaging measures (^1H NMR and X-ray) and mechanical properties.....	81
TABLE 5.1	Combinations of adiabatic full passage pulse parameters.....	103
TABLE AIII.1	Observed uT_2 ^1H signal size in myelinated nerves and myelin extract, compared to expected mammalian myelin membrane ^1H content.....	176

LIST OF FIGURES

	Page
FIGURE 1.1 Bone matrix schematic.....	3
FIGURE 2.1 3D CTI of a human femur segment in a conventional volume imaging coil at 30 μ s TE.....	28
FIGURE 2.2 Loop-gap resonator schematic.....	29
FIGURE 2.3 Maximum intensity projections (MIPs) from 3D CTI of different loop-gap coil configurations.....	35
FIGURE 2.4 Effects of RF coil shielding on background signal.....	36
FIGURE 2.5 Low- ^1H coils available on the in-house small animal magnets.....	42
FIGURE 3.1 Wideline NMR and multiexponential T_2 spectroscopy of human cortical bone specimens.....	54
FIGURE 3.2 2D T_1 - T_2 Spectra.....	56
FIGURE 3.3 2-D exchange spectroscopy (REXSY) representative of all human cortical bone specimens.....	57
FIGURE 3.4 Effects of D_2O immersion on resonance and multiexponential T_2 spectra of cortical bone specimens.....	58
FIGURE 3.5 Postulated biophysical origins of NMR signal relaxation components in human cortical bone.....	60
FIGURE 4.1 NMR/ μ CT/mechanical testing study overview.....	72
FIGURE 4.2 Representative μ CT.....	76
FIGURE 4.3 Mechanical testing analysis.....	77
FIGURE 4.4 Summary of T_2 spectra measured from 40 human cortical bone samples.....	79
FIGURE 4.5 Correlations of measured peak stress and T_2 spectral component amplitudes and avBMD measured by μ CT.....	80
FIGURE 4.6 Adiabatic T_2 -selective suppression.....	85

FIGURE 5.1	A model of the water ^1H NMR lineshapes in human cortical bone.....	92
FIGURE 5.2	Simulated effects of a sech AFP pulse on cortical bone water longitudinal magnetization.....	93
FIGURE 5.3	Proposed ultra-short echo time-based approaches for MRI of cortical bone net, pore, and bound water content.....	95
FIGURE 5.4	Observed effects of a sech AFP pulse on cortical bone water longitudinal magnetization.....	110
FIGURE 5.5	Bi-exponential fitting for bound/pore water separation in the T_2^* domain.....	111
FIGURE 5.6	Signal contents and correlations to gold standard measures for the uTE, DAFP, and AIR methods.....	113
FIGURE 5.7	Mechanical property correlations to steady state signals across specimens.....	115
FIGURE AI.1	200 MHz loop-gap probehead schematic and component layout.....	142
FIGURE AI.2	Bench-top setup for probehead testing with a 4-port network analyzer.....	146
FIGURE AI.3	Network analyzer traces from the 20mm, 200.25 MHz loop-gap for tuning, matching, and balancing.....	149
FIGURE AII.1	Diamond saw setup.....	154
FIGURE AII.2	Drill press setup.....	156
FIGURE AIII.1	Representative T_2 spectra from... [myelin and non-myelin sources].....	166
FIGURE AIII.2	T_2 - T_2 exchange spectroscopy (REXSY) spectra from frog nerve and the bovine brain myelin extract.....	169
FIGURE AIII.3	Rapid relaxation in myelin extract and in sciatic nerve and phantoms.....	172
FIGURE AIII.4	Expected biological myelin ^1H fractions, by molecular source.....	179

INTRODUCTION

This dissertation focuses on augmenting the capabilities of clinical bone diagnostics by exploring ^1H nuclear magnetic resonance (NMR) and magnetic resonance imaging (MRI) methods for human cortical bone characterization. In doing so, the overall goal is to advance our understanding of ^1H NMR relaxation in human cortical bone to the point that diagnostically-relevant parameters may be extracted from *in vivo* bone MRI measurements. Along these lines, Chapter 1 provides motivation for cortical bone MRI by reviewing the limitations of current clinical X-ray diagnostics and highlighting the complementary capabilities of MRI. Chapter 2 describes NMR hardware developments necessary for a rigorous, relaxation-based characterization of cortical bone NMR signals. Such characterization was used to determine the micro-anatomical origins of cortical bone NMR signal components, as presented in Chapter 3. Chapter 4 demonstrates the diagnostic relevance of these signal components by comparing them to various bone mechanical properties. Chapter 5 presents clinically practical methods for quantitative, diagnostic bone MRI. Finally, Chapter 6 concludes with thoughts on the future of the field. Collectively, this work represents a biophysical basis for cortical bone MRI, which stands ready for translation to clinical practice and research studies.

CHAPTER 1

The Case for Clinical Magnetic Resonance Imaging of Human Cortical Bone

As little as 15 years ago, most clinical radiologists and medical imaging research scientists likely would have dismissed the notion of *in vivo* magnetic resonance imaging (MRI) for human cortical bone. While the physical phenomenon of nuclear magnetic resonance (NMR), which underpins MRI, is just as applicable to cortical bone as it is to the soft tissues that have become mainstays of clinical MRI, there were some key technological limitations of most MRI scanners at the time that produced large signal voids in cortical bone—no matter what scan settings the MRI technician tried. MRI technology has since advanced, and modern hardware now allows for the direct imaging of cortical bone. In fact, researchers have developed a variety of methods for such imaging. Although MRI is still not a widely considered method for cortical bone imaging, the notion of clinical bone MRI has begun to gain traction in the research community. However, in order to become a routine standard of care, MRI must first demonstrate clear advantages over current bone imaging in the clinic, which is dominated by a single imaging modality that has been used to visualize bones since the late 19th century: X-rays.

In the following sections, relevant cortical bone micro-anatomy is surveyed, and current X-ray-based clinical practices for bone imaging are reviewed, with emphases on capabilities and limitations. In light of the limitations of X-rays, the case for moving beyond such imaging of cortical bone is presented, as motivated by the importance of X-ray-invisible non-mineral components to bone integrity. Finally, modern developments in MRI that enable cortical bone visualization are discussed, focusing on their potential for clinical imaging.

1.1 — Cortical Bone Micro-anatomy: The Biophysical Bases for Bone Imaging

Cortical bone-related contrast in X-ray and MRI imaging has biophysical origins that stem from bone's unique micro-anatomy, which is reviewed in (1-3) and summarized in the following. Cortical bone is a complex composite of nano- and micro-anatomical components including collagen matrix, calcium phosphate mineral crystals, lipids, and porous spaces such as Haversian canals and the lacunar-canalicular system. These structures are generally arranged in repeating cylindrical units (100's of μm in diameter) called osteons (Fig 1.1), which are oriented parallel to the long bone axis.

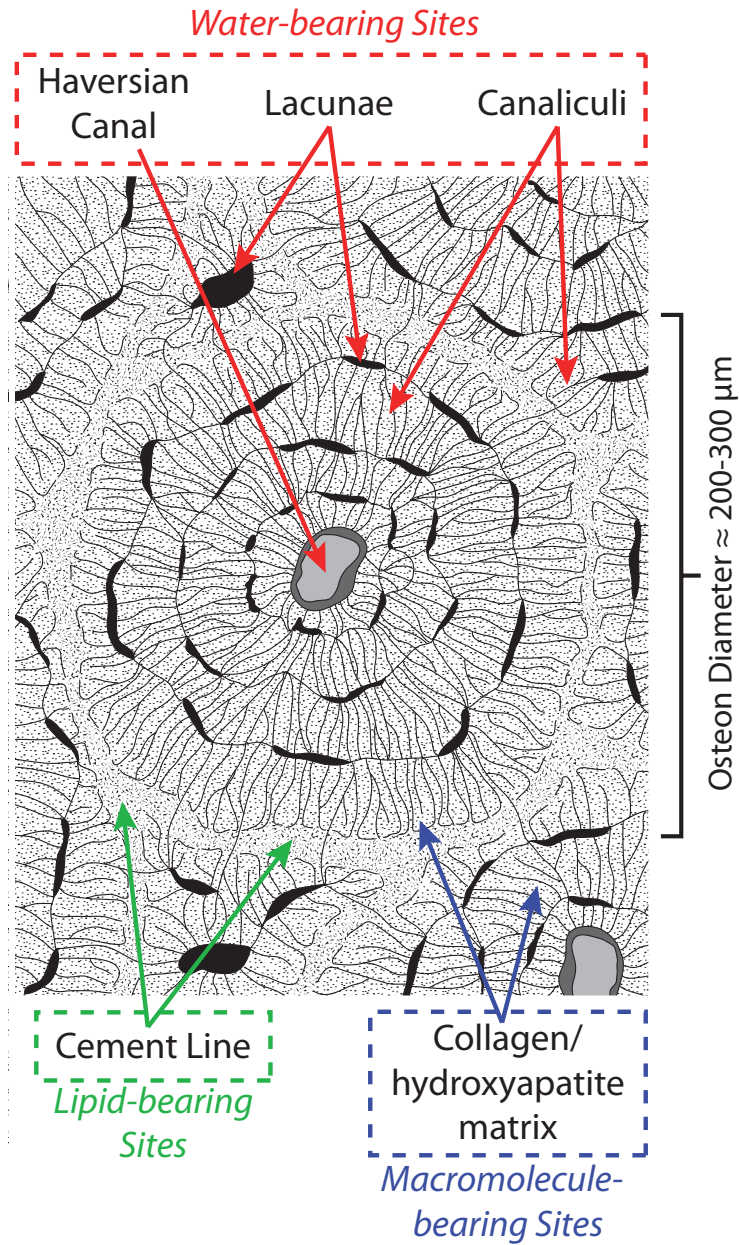


FIGURE 1.1 *Bone matrix schematic.* Expected biophysical distribution of osteonal water, lipid, and macromolecule-bearing proton sites in human cortical bone are identified in red, green, and blue, respectively. The primary nano- and microstructures housing each of these sites are given in dashed boxes.

Each osteon houses mineralized matrix surrounding a central Haversian canal (10's to 100's of μm in diameter), which in turn forms the majority of

osteonal porosity and hosts vessels and nerves. Osteons are frequently interconnected via lateral Volkmann canals ($\approx 10 \mu\text{m}$ -scale), which bridge neighboring Haversian canals and assist with inter-osteonal fluid flows. Small pores called lacunae ($\approx 1 \mu\text{m}$ -scale) are distributed throughout each osteon and contain osteocytes, the cellular components of cortical bone responsible for recruiting other cells for matrix formation (osteoblasts) or resorption (osteoclasts). To facilitate nutrient and fluid transport among bioactive sites in the osteon and support cell signaling via the transverse processes of osteocytes, a network of canaliculi ($\approx 0.1 \mu\text{m}$ -diameter passageways) serves to interconnect lacunae and Haversian canals. Portions of the osteon outside of porous spaces consist of a dense collagen matrix laden with calcium phosphate nanocrystals (similar in form to hydroxyapatite), which represents cortical bone's inorganic mineral phase. Finally, lipids can be found in the cement line spaces between osteons, which are transition zones between regions of bone formation and resorption.

At present, all of these micro-anatomical features occur on spatial scales comparable to or smaller than the practical resolutions of clinical X-ray and MRI images, so contrast in both cases arises from a spatial average of osteonal components. As will be discussed further below, X-rays are chiefly sensitive to

the bone mineral phase, so the density and distribution of calcium phosphate nanocrystals throughout the bone matrix is the primary contributor to X-ray contrast. ^1H NMR and MRI, on the other hand, are sensitive to variations in the proton molecular environment, and it is useful to examine the different ^1H sources in cortical bone. Each of the cortical bone micro-anatomical components includes one or more distinct proton micro-environments, which differ according to their local chemical, magnetic and electrical milieu. For example, the collagen component is host to both hydrogen-bound surface water and covalently-bound protein backbone protons. Submicron to millimeter-scale porous spaces in the lacuno-canalicular system contain water with varying degrees of motional freedom. Finally, lattice defect sites in the calcium phosphate crystals host several populations of intercalated water molecules and surface hydroxyl sites (4-5), however, this quantity of protons is negligible compared to that within the pore spaces and collagen matrix. Since each of these proton sources contributes to the net NMR signal on a stoichiometric basis, MRI signal contributions from cortical bone are expected to be dominated by protons in the non-mineral phases.

1.2 — Cortical Bone Imaging in Today's Clinic

The current clinical bone diagnostic climate is one thoroughly dominated by X-ray imaging. This is because, since Wilhelm Röntgen's early X-ray photographs

(6), the contrast in X-ray-based images has been recognized as predominantly arising from compact bone. Because X-ray imaging is fundamentally a transmission method, whereby contrast is generated by a spatially varying absorption of X-ray photons during transit of the imaged tissue, the sharp image contrast from bone arises from its radio-opacity relative to surrounding soft tissues. The electron-dense calcium phosphate-based minerals in bone tissue provide the source of this relative opacity. As such, cortical bone absorbs X-rays upwards of five-times more efficiently than soft tissue (7), so, in practice, X-ray imaging is only sensitive to the mineralized portion of bone tissues.

The sensitivity of X-rays to bone mineral content provides a biophysical basis for several X-ray imaging strategies currently in routine clinical practice. Digital or chemical film X-rays are one of the cheapest and most ubiquitous medical imaging procedures, and they excel at depicting two-dimensional projections of bone morphology (8). However, quantitative imaging of bone mineral content with this method is problematic, as large amounts of surrounding soft tissue can provide significant bias (9). To mitigate soft tissue contributions, dual-energy X-ray absorptiometry (DXA, formerly DEXA) was developed for quantitative imaging of bone mineral density (10).

DXA consists of two plain film X-rays collected separately at different X-ray energy levels. Due to the stronger dependence of absorption on X-ray energy level in bone than in soft tissues, a subtraction of the two images tends to cancel soft tissue contributions to give an image of predominantly bone mineralization. By calibrating to phantoms of known mineral density (11,12), DXA images can be converted to quantitative measures of bone mineralization. Diagnostic utility is established by comparing a patient's results to previously-established population-wide measures using the metric of areal bone mineral density (aBMD), which is the DXA-observed bone mineral content normalized to the bone area projected onto the DXA image. Statistical tools are used to score aBMD measures (13), such as the T-score (fractional number of standard deviations above/below the mean population aBMD) or Z-score (likewise, but relative to age-matched population aBMD) (14). These scores give clinicians hard numbers to assess bone mineral deficiency, which is conventionally linked to an increase in overall fracture risk. Because of its rapid, unambiguous results and low point-of-care costs, DXA has become the preeminent bone quantitation tool in use by clinicians today.

Despite its clinical popularity, DXA suffers a key fundamental flaw: the DXA score does not predict which individuals will fracture (15-18). This poor

fracture prediction stems from both DXA imaging dimensionality limitations and, perhaps more critically, the fact that bone mineral density (the only output of DXA) is not the only determinant of fracture risk.

DXA images are limited to two-dimensional projections through a variety of prognostic skeletal sites, such as the forearm, hip, femur, and vertebral bodies (19-23). Given their two-dimensional nature, standard DXA scans do not account for patient-specific variation in bone thickness or volume. Since there is a (potentially highly) nonlinear relationship between bone volume and projection area, this unaccounted third dimension is a source of disparity when comparing measurements from patients of significantly different bone thickness (24). A patient with slender, properly-mineralized bones might have the same DXA score as a patient with large, poorly-mineralized (i.e. highly porous) bones. And both of these patients might score deficient compared to a patient of normal bone size and mineral content. Clinicians attempt to counter this problem by incorporating risk factors such as age (hence the Z-score), gender, weight, body mass index, or other gross anatomical measures into the interpretation of DXA scores, thereby using surrogates for the missing third dimension (25). However, this is a limited approach and does not account for ethnic variations, etc., prompting the World Health Organization to established DXA criteria only

centered around middle-aged white women, which is a commonly-studied population (26,27).

More recently, fully three-dimensional analogs to DXA have emerged in the form of quantitative computed tomography (QCT) (28,29), which use calibrated CT techniques to generate measures of volumetric bone mineral density (vBMD). Given the added expense of CT hardware, QCT has yet to become as widespread as DXA even though it provides a solution to DXA's missing imaging dimension. Although not widely practiced, the current state-of-the-art involves coupling QCT-based bone geometry measures to patient-specific finite element modeling for mechanical property prediction (30-33). Although this results in an improved ability to predict mechanical response, QCT still shares the same fundamental limitation as DXA: as X-ray-based measures, they are primarily sensitive to mineralization, and mineral content is not the only contributor to bone fracture resistance.

1.3 — Assessing Fracture Resistance: Going Beyond X-rays and Bone Mineral Content

As previously mentioned, cortical bone contains two other dominant constituents in addition to its mineral phase: collagen and water, which collectively occupy at least one third of cortical bone's mass fraction (34). Thus, a purely mineral-based characterization of bone is incomplete on both micro-

anatomic and bulk mass bases. It should therefore come as no surprise that mineral content is not the only contributor to fracture resistance, as both collagen and water are critically important. Currently, the mineral phase is viewed as contributing to bone stiffness and bone's initial elastic response to mechanical stimuli (35,36), while collagen provides essential resistance to fracture propagation via toughening and resilience after prolonged loading (37-42). Given that collagen is a well-hydrated biomolecule, the biomechanical role of water is also implicit to that of collagen.

The importance of bone's non-mineral components to fracture risk can be separately seen in the natural aging process, bone disease, and laboratory experiments. The decrease of bone fracture resistance is an inescapable consequence of aging and arises from a multitude of micro-anatomical and physiological changes in bone tissue. A common trend is the overall decrease in bone density associated with a loss of mineral content (16,36,43). Accompanying this are 1) a decrease in mechanically-stabilizing enzymatic crosslinks throughout the bone collagen matrix (40,41,44,45), and 2) an increase in oxidative stress-related advanced glycation endproducts that accumulate non-enzymatic crosslinks in bone's collagen phase, similar to those occurring with diabetes mellitus (46-50). These and other age-related changes create disruptions in bone's

collagen matrix structure and crosslink status, which are deleteriously linked to bone mechanical properties (40,44,51-53). Therefore, individuals of considerably different ages can have similar bone mineral content but markedly different fracture risk because of altered collagen status. As such, the bone mineral-centric DXA method cannot wholly explain age-related changes in fracture resistance (15,16).

In the case of non-mineral bone components' involvement in disease, the spectrum of conditions known as osteogenesis imperfecta (OI) manifests when a genetic anomaly disrupts the ability of collagen to fold properly and assume its mechanically-useful structural confirmation (54-56). While it causes a number of tolerated systemic effects outside the skeletal system, OI manifests in bone by creating catastrophic brittleness to the point of facile fracturing and, in severe cases, perinatal fatality. Depending on the OI type, normal or even elevated bone mineral density is observed as there are presumably vacancies in the defective collagen matrix for additional mineralization (57), and associated alterations to bone mineral crystal size have also been noted (58,59). Thus, DXA-visible net mineral content is not the only factor behind the compromised bone biomechanics in OI, providing another example of the collagen phase's importance to bone fracture risk.

Finally, the significance of water to bone mechanics can be demonstrated in the laboratory via bone dehydration experiments. While its physiological significance still remains unclear, water loss in bone causes an increase in bone brittleness and a decrease in bone fracture resistance metrics such as work to fracture (60,61). Additionally, the nature of these mechanical changes depends on the mechanism of water removal (heat vs. vacuum drying), suggesting different biomechanical roles for tightly and loosely-bound water in bone. For example, loosely-bound water such as that found in porous spaces has been linked to bone's viscoelastic properties via a hydraulic effect distributed through bone's porous structures (1). Such findings illustrate the biomechanical importance of bone matrix hydration.

In the provided examples of aging, OI, and bone dehydration, changes to non-mineral components cause key biomechanical deficits which are not apparent from mineral-centric, X-ray-based contrast. Thus, to assess the complete bone mechanical response and generate a complete picture of fracture risk, one should quantify the X-ray-invisible non-mineral components of bone. MRI has the potential to do so, as demonstrated below.

1.4 — Potential for MRI-based Cortical Bone Diagnostic Imaging

While X-rays have poor sensitivity to collagen and water content, ^1H NMR is broadly sensitive to protons throughout bone, including those situated on its non-mineral components. Thus, NMR measures of bone collagen and/or water offer novel information that X-rays cannot provide and can be used to potentially improve the prediction of bone fracture resistance. The challenge at hand is to develop clinically-practical MRI techniques capable of depicting such non-mineral components in human cortical bone *in vivo*.

As previously noted, modern advances in MRI technology have enabled the clinical imaging of non-mineral components in cortical bone. These advances have primarily consisted of faster hardware switching between radio frequency (RF) transmission (T) and reception (R) signal pathways, the former being necessary for MRI signal generation and the latter for image formation. This faster T/R switching is critical for bone imaging, since the predominant bone MRI signal decays over time (i.e. relaxes) orders of magnitude faster than most soft tissues. Thus, older MRI scanners with slower switching suited for soft tissues simply could not acquire enough bone MRI signal for image formation prior to its complete relaxation. The nature and implications of relaxation in cortical bone are the predominant subjects of the later chapters herein, but it is sufficient for

now to note that MRI data can be collected on modern scanners at the same timescale as, or faster than, the bone signal relaxation processes, and this capability has spawned a variety of imaging methods. In the following discussion of these methods, it is assumed that the reader has familiarity with basic MRI concepts; if this is not the case, consider consulting the following excellent references (roughly in order of increasing depth and complexity): (62-66).

MRI scanner protocols which utilize the rapid T/R switching times necessary for bone imaging are broadly referred to as ultra-short echo time (uTE) methods (67,68). The echo time (TE) in the context of uTE imaging typically refers to the time between the midpoint of RF pulse transmission and the start of signal acquisition, and TE values of less than $\approx 0.5-1.0$ milliseconds garner the uTE moniker (for comparison, conventional values of TE used in soft tissue MRI are on the order of 10 ms, or longer). uTE imaging methods commonly achieve such short echo times by foregoing the relatively lengthy gradient slice rewind and cartesian imaging gradient phase-encoding periods conventional to soft tissue MRI, instead favoring 3D volume imaging (or half-pulse slice selection) and center-out (e.g. radial half-spoke) image encoding strategies. Despite sharing these commonalities, three distinct uTE methods have arisen for cortical bone

imaging: 1) conventional uTE, 2) purely phase-encoded imaging, and 3) imaging with gapped excitation and acquisition.

Conventional uTE is analogous to conventional gradient echo imaging, combining fast T/R switching with three dimensional radial half-spoke frequency encoding and non-selective hard excitation pulses to achieve a TE limited chiefly by T/R switching speed (80 μ s and shorter TEs have been demonstrated on clinical hardware (69)). Slice-wise two dimensional uTE imaging has been demonstrated with excitation half-pulses using methods such as variable-rate selective excitation (69-71), leading to practical scan times over reduced imaging volumes. Purely phase-encoded imaging includes methods, such as single-point ramped imaging with T₁ enhancement (SPRITE) (72), ramp up imaging gradients prior to a short ($\approx 10 \mu$ s) hard RF excitation (not slice selective) such that phase encoding occurs during the TE period, after which a single datum is collected. Such methods tend to be lengthy, as an excitation pulse is needed for each imaging datum, and TE is limited by gradient strength and imaging resolution constraints. Water and fat suppressed projection imaging (WASPI) (73) combines this phase encoding with conventional uTE frequency encoding, forming a hybrid sequence that shortens scan times and achieves shorter echo times. Finally, imaging with gapped excitation and acquisition proceeds by interleaving

transmit and receive periods in the presence of an imaging gradient and has been implemented under adiabatic conditions using so-called frequency-swept imaging with Fourier transformation (SWIFT) (74). Such imaging places tremendous demands on the T/R switching mechanism, both in duty cycle and switching speed, but nonetheless achieves the shortest apparent TE ($\approx 4 \mu\text{s}$ or less) of all uTE methods. (The MRI purist would note that all of these uTE methods sample the initial MRI signal, or free induction decay, rather than a spin or gradient echo, and thus the uTE moniker is a misnomer and the notion of echo times in this context is misleading.)

Each of the aforementioned uTE methods has been successfully demonstrated for *in vivo* MRI of the non-mineral components in human cortical bone (73-79), in some cases providing quantitative measures of proton density (80-82). The resulting images provide provocative contrast that prompt the question as to what types of clinically diagnostic information can be gained in addition to the mineralization data provided by X-rays. Despite this rich field of productive imaging methods, the diagnostic potential of bone MRI remains relatively unexplored and is evaluated in detail in the following chapters.

1.5 — References

1. Cowin S. Bone poroelasticity. *Journal of Biomechanics* 1999;32(3):217-238.

2. Olszta M, Cheng X, Jee S, Kumar R, Kim Y, Kaufman M, Douglas E, Gower L. Bone structure and formation: A new perspective. *Materials Science & Engineering R-Reports* 2007;58(3-5):77-116.
3. Weiner S, Wagner H. The material bone: Structure mechanical function relations. *Annu Rev Mater Sci* 1998;28:271-298.
4. Cho G, Wu Y, Ackerman J. Detection of hydroxyl ions in bone mineral by solid-state NMR spectroscopy. *Science* 2003;300(5622):1123-1127.
5. Wilson E, Awonusi A, Morris M, Kohn D, Tecklenburg M, Beck L. Highly ordered interstitial water observed in bone by nuclear magnetic resonance. *Journal of Bone and Mineral Research* 2005;20(4):625-634.
6. Glasser O. Wilhelm Conrad Rontgen and the Early History of the Roentgen Rays. *The American Journal of the Medical Sciences* 1934;187(4):566.
7. Ma C, Seuntjens JP. Mass-energy absorption coefficient and backscatter factor ratios for kilovoltage x-ray beams. *Physics in Medicine and Biology* 1999;44:131-143.
8. Yochum T, Rowe LJ. *Yochum and Rowe's Essentials of Skeletal Radiology*: Lippincott Williams & Wilkins 2005. 1800 p.
9. Kuiper JW, van Kuijk C, Grashuis JL, Ederveen AG, Schütte HE. Accuracy and the influence of marrow fat on quantitative CT and dual-energy X-ray absorptiometry measurements of the femoral neck in vitro. *Osteoporosis International* 1996;6(1):25-30.
10. Cullum ID, Ell PJ, Ryder JP. X-ray dual-photon absorptiometry: a new method for the measurement of bone density. *The British Journal of Radiology* 1989;62(739):587-592.
11. Orwoll ES, Oviatt SK. Longitudinal precision of dual-energy x-ray absorptiometry in a multicenter study. The Nafarelin/Bone Study Group. *Journal of Bone and Mineral Research* 1991;6(2):191-197.
12. Genant HK, Grampp S, Glüer CC, Faulkner KG, Jergas M, Engelke K, Hagiwara S, van Kuijk C. Universal standardization for dual x-ray absorptiometry: patient and phantom cross-calibration results. *Journal of Bone and Mineral Research* 1994;9(10):1503-1514.
13. Yochum T, Rowe LJ. *Yochum and Rowe's Essentials of Skeletal Radiology*: Lippincott Williams & Wilkins 2005. 1800 p.

14. Carey JJ, Delaney MF, Love TE, Richmond BJ, Cromer BA, Miller PD, Manilla-McIntosh M, Lewis SA, Thomas CL, Licata AA. DXA-Generated Z-Scores and T-Scores May Differ Substantially and Significantly in Young Adults. *Journal of Clinical Densitometry* 2007;10(4):351-358.
15. Kanis JA, Johnell O, Oden A, Dawson A, de Laet C, Jonsson B. Ten year probabilities of osteoporotic fractures according to BMD and diagnostic thresholds. *Osteoporosis International* 2001;12(12):989-995.
16. Russo C, Lauretani F, Bandinelli S, Bartali B, Di Iorio A, Volpato S, Guralnik J, Harris T, Ferrucci L. Aging bone in men and women: beyond changes in bone mineral density. *Osteoporosis International* 2003;14(7):531-538.
17. Ott SM. When Bone Mass Fails to Predict Bone Failure. *Calcified Tissue International*. Volume 53; 1993. p S7-S13.
18. Schuit S, van der Klift M, Weel A, de Laet C. Fracture incidence and association with bone mineral density in elderly men and women: the Rotterdam Study. *Bone* 2004;34:195-202.
19. Grampp S, Genant HK, Mathur A, Lang P, Jergas M, Takada M, Glüer CC, Lu Y, Chavez M. Comparisons of noninvasive bone mineral measurements in assessing age-related loss, fracture discrimination, and diagnostic classification. *Journal of Bone and Mineral Research* 1997;12(5):697-711.
20. Myers E, Hecker A, Rooks D, Hipp J. Geometric variables from DXA of the radius predict forearm fracture load in vitro. *Calcified Tissue International* 1993;52:199-204.
21. Ebbesen E, Thomsen J, Beck-Nielsen H. Lumbar vertebral body compressive strength evaluated by dual-energy X-ray absorptiometry, quantitative computed tomography, and ashing. *Bone* 1999;25:713-724.
22. Cheng X, Lowet G, Boonen S. Prediction of vertebral and femoral strength in vitro by bone mineral density measured at different skeletal sites. *Journal of Bone and Mineral Research* 1998;13:1439-1443.
23. Bouxsein ML, Muller ME, Webber CE. Predicting the failure load of the distal radius. *Osteoporosis International* 2003;14(4):345-352.
24. Lochmuller E, Miller P, Burklein D, Wehr U, Rambeck W, Eckstein F. In situ femoral dual-energy X-ray absorptiometry related to ash weight, bone size and density, and its relationship with mechanical failure loads of the proximal femur. *Osteoporosis International* 2000;11(4):361-367.

25. Kanis J, Oden A, Johnell O, Jonsson B, de Laet C, Dawson A. The burden of osteoporotic fractures: a method for setting intervention thresholds. *Osteoporosis International* 2001;12(5):417-427.
26. Kanis J, Alexeeva L, Bonjour J, Burkhardt P, Christiansen C, Cooper C, Delmas P, Johnell O, Johnston C, Kanis J, Khaltaev N, Lips P, Mazzuoli G, Melton L, Meunier P, Seeman E, Stepan J, Tosteson. Assessment of Fracture Risk and Its Application to Screening for Postmenopausal Osteoporosis - Synopsis of a Who Report. *Osteoporosis International* 1994;4(6):368-381.
27. Thomas E, Richardson J, Irvine A, Hassell A, Hay E. Osteoporosis: what are the implications of DEXA scanning "high risk" women in primary care? *Family Practice* 2003;20(3):289-293.
28. Lochmüller E-M, Müller R, Kuhn V, Lill CA, Eckstein F. Can novel clinical densitometric techniques replace or improve DXA in predicting bone strength in osteoporosis at the hip and other skeletal sites? *Journal of Bone and Mineral Research* 2003;18(5):906-912.
29. Genant H, Engelke K, Fuerst T. Noninvasive assessment of bone mineral and structure: state of the art. *Journal of Bone and Mineral Research* 1996;11(6):707-730.
30. Yosibash Z, Padan R, Joskowicz L, Milogrom C. A CT-based high-order finite element analysis of the human proximal femur compared to in-vitro experiments. *Journal of Biomechanical Engineering* 2007;129:297-309.
31. Cody D, Gross G, Hou F, Spencer H, Goldstein S, Fyhrie D. Femoral strength is better predicted by finite element models than QCT and DXA. *Journal of Biomechanics* 1999;32:1013-1020.
32. Yosibash Z, Trabelsi N, Milgrom C. Reliable simulations of the human proximal femur by high-order finite element analysis validated by experimental observations. *Journal of Biomechanics* 2007;40(16):3688-3699.
33. Schileo E, Taddei F, Malandrino A, Cristofolini L, Viceconti M. Subject-specific finite element models can accurately predict strain levels in long bones. *Journal of Biomechanics* 2007;40(13):2982-2989.
34. Gong J, Arnold J, Cohn S. Composition of Trabecular and Cortical Bone. *The Anatomical Record Part A: Discoveries in Molecular, Cellular, and Evolutionary Biology* 1964;149:325-331.

35. Singer K, Edmondston S, Day R, Breidahl P, Price R. Prediction of Thoracic and Lumbar Vertebral Body Compressive Strength - Correlations with Bone-Mineral Density and Vertebral Region. *Bone* 1995;17(2):167-174.
36. Smith CB, Smith DA. Relations Between Age, Mineral Density and Mechanical Properties of Human Femoral Compacta. *Acta Orthopaedica* 1976;47(5):496-502.
37. Boskey A, Wright T, Blank R. Collagen and bone strength. *Journal of Bone and Mineral Research* 1999;14:330-335.
38. Martin RB, Ishida J. The relative effects of collagen fiber orientation, porosity, density, and mineralization on bone strength. *Journal of Biomechanics* 1989;22(5):419-426.
39. Viguet-Carrin S, Garnero P, Delmas PD. The role of collagen in bone strength. *Osteoporosis International* 2005;17(3):319-336.
40. Zioupos P, Currey J, Hamer A. The role of collagen in the declining mechanical properties of aging human cortical bone. *Journal of Biomedical Materials Research*. Volume 45; 1999. p 108-116.
41. Zioupos P. Ageing human bone: Factors affecting its biomechanical properties and the role of collagen. *Journal of Biomaterials Applications* 2001;15(3):187-229.
42. Burr D. The contribution of the organic matrix to bone's material properties. *Bone* 2002;31:8-11.
43. Ebbesen E, Thomsen J, Beck-Nielsen H, Nepper-Rasmussen H, Mosekilde L. Age- and gender-related differences in vertebral bone mass, density, and strength. *Journal of Bone and Mineral Research* 1999;14(8):1394-1403.
44. Wang X, Shen X, Li X, Agrawal C. Age-related changes in the collagen network and toughness of bone. *Bone* 2002;31(1):1-7.
45. Oxlund H, Barckman M, Ortoft G, Andreassen T. Reduced Concentrations of Collagen Cross-Links Are Associated with Reduced Strength of Bone. *Bone*. Volume 17; 1995. p S365-S371.
46. Brownlee M. Advanced Protein Glycosylation in Diabetes and Aging. *Annual Review of Medicine* 1995;46:223-234.
47. Verzijl N, DeGroot J, Oldehinkel E, Bank R, Thorpe S, Baynes J, Bayliss M, Bijlsma J, Lafeber F, TeKoppele J. Age-related accumulation of Maillard reaction products in human articular cartilage collagen. *Biochemical Journal* 2000;350:381-387.

48. Wolff S, Jiang Z, Hunt J. Protein Glycation And Oxidative Stress In Diabetes-Mellitus And Aging. *Free Radical Biology and Medicine* 1991;10(5):339-352.
49. Ulrich P, Cerami A. Protein glycation, diabetes, and aging. *Recent progress in hormone research* 2001;56(1):1.
50. Paul R, Bailey A. Glycation of collagen: the basis of its central role in the late complications of ageing and diabetes. *The International Journal of Biochemistry & Cell Biology* 1996;28(12):1297-1310.
51. Tang SY, Zeenath U, Vashishth D. Effects of non-enzymatic glycation on cancellous bone fragility. *Bone* 2007;40(4):1144-1151.
52. Schwartz A. Diabetes mellitus: Does it affect bone? *Calcified Tissue International* 2003;73(6):515-519.
53. Santana R, Xu L, Chase H, Amar S, Graves D, Trackman P. A role for advanced glycation end products in diminished bone healing in type 1 diabetes. *Diabetes* 2003;52(6):1502-1510.
54. Rauch F, Glorieux FH. Osteogenesis imperfecta. *The Lancet* 2004;363(9418):1377-1385.
55. Sykes B, Ogilvie D, Wordsworth P, Anderson J, Jones N. Osteogenesis Imperfecta Is Linked to Both Type-I Collagen Structural Genes. *Lancet* 1986;2(8498):69-72.
56. Bonadio J, Holbrook K, Gelinas R. Altered triple helical structure of type I procollagen in lethal perinatal osteogenesis imperfecta. *Journal of Biological Chemistry* 1985;260:1734-1742.
57. Boyde A, Travers R, Glorieux F. The mineralization density of iliac crest bone from children with osteogenesis imperfecta. *Calcified Tissue International* 1999;64:185-190.
58. Vetter U, Eanes E, Kopp J, Termine J, Robey P. Changes in Apatite Crystal Size in Bones of Patients with Osteogenesis Imperfecta. *Calcified Tissue International* 1991;49(4):248-250.
59. Fratzl P, Paris O, Klaushofer K. Bone mineralization in an osteogenesis imperfecta mouse model studied by small-angle x-ray scattering. *Journal of Clinical Investigation* 1996;97:396-402.
60. Nyman J, Roy A, Shen X, Acuna R, Tyler J, Wang X. The influence of water removal on the strength and toughness of cortical bone. *J Biomech* 2006;39(5):931-938.

61. Sedlin E. Factors affecting the determination of the physical properties of femoral cortical bone. *Acta Orthopaedica Scandinavica* 1966;37:29-48.
62. Hornak JP. *The Basics of MRI*. <http://www.cis.rit.edu/htbooks/mri/>; 1996.
63. Nishimura DG. *Principles of magnetic resonance imaging*; 1996. 223 p.
64. Haacke E, Brown R, Thompson M, Venkatesan R. *Magnetic resonance imaging: physical principles and sequence design*: New York: A John Wiley and Sons; 1999.
65. Bernstein MA, King KF, Zhou XJ. *Handbook of MRI pulse sequences*. Academic Press; 2004. 1017 p.
66. Blumich B. *NMR imaging of materials*: Oxford University Press; 2000. 541 p.
67. Robson M, Gatehouse P, Bydder M, Bydder G. Magnetic resonance: An introduction to ultrashort TE (UTE) imaging. *Journal Of Computer Assisted Tomography* 2003;27(6):825-846.
68. Gatehouse P, Bydder G. Magnetic resonance imaging of short T-2 components in tissue. *Clinical Radiology* 2003;58(1):1-19.
69. Tyler DJ, Robson MD, Henkelman RM, Young IR, Bydder GM. Magnetic resonance imaging with ultrashort TE (UTE) PULSE sequences: technical considerations. *Journal of Magnetic Resonance Imaging* 2007;25(2):279-289.
70. Conolly S, Nishimura D, Macovski A, Glover G. Variable-rate selective excitation. *Journal of Magnetic Resonance (1969)* 1988;78(3):440-458.
71. Pauly J, Conolly S, Nishimura D, Macovski A. Slice-selective excitation for very short T2 species. *Proceedings of the SMRM 8th Annual Meeting, Amsterdam, The Netherlands* 1989:28.
72. Balcom B, MacGregor R, Beyea S, Green D, Armstrong R, Bremner T. Single-point ramped imaging with T-1 enhancement (SPRITE). *Journal of Magnetic Resonance Series A* 1996;123(1):131-134.
73. Wu Y, Ackerman J, Chesler D, Graham L, Wang Y, Glimcher M. Density of organic matrix of native mineralized bone measured by water- and fat-suppressed proton projection MRI. *Magnetic Resonance in Medicine* 2003;50(1): 59-68.
74. Idiyatullin D, Corum C, Park J, Garwood M. Fast and quiet MRI using a swept radiofrequency. *Journal of Magnetic Resonance* 2006;181(2):342-349.

75. Robson MD, Bydder GM. Clinical ultrashort echo time imaging of bone and other connective tissues. *NMR in Biomedicine* 2006;19(7):765-780.
76. Reichert ILH, Robson MD, Gatehouse PD, He T, Chappell KE, Holmes J, Girgis S, Bydder GM. Magnetic resonance imaging of cortical bone with ultrashort TE pulse sequences. *Magnetic Resonance Imaging* 2005;23(5):611-618.
77. Wu Y, Dai G, Ackerman J, Hrovat M, Glimcher M, Snyder B, Nazarian A, Chesler D. Water- and fat-suppressed proton projection MRI (WASPI) of rat femur bone. *Magnetic Resonance in Medicine* 2007;57(3):554-567.
78. Techawiboonwong A, Song H, Wehrli F. In vivo MRI of submillisecond T-2 species with two-dimensional and three-dimensional radial sequences and applications to the measurement of cortical bone water. *NMR in Biomedicine* 2008;21(1):59-70.
79. Weiger M, Hennel F, Pruessmann KP. Sweep MRI with Algebraic Reconstruction. *Magnetic Resonance in Medicine* 2010;64(6):1685-1695.
80. Techawiboonwong A, Song H, Leonard M, Wehrli F. Cortical bone water: In vivo quantification with ultrashort echo-time MR imaging. *Radiology* 2008;248(3):824-833.
81. Du J, Carl M, Bydder M, Takahashi A, Chung CB, Bydder GM. Qualitative and quantitative ultrashort echo time (UTE) imaging of cortical bone. *Journal of Magnetic Resonance* 2010;207(2):304-311.
82. Cao H, Ackerman J, Hrovat M, Graham L, Glimcher M, Wu Y. Quantitative Bone Matrix Density Measurement by Water- and Fat-Suppressed Proton Projection MRI (WASPI) With Polymer Calibration Phantoms. *Magnetic Resonance in Medicine* 2008;60(6):1433-1443.

CHAPTER 2

Prerequisites for Nuclear Magnetic Resonance of Cortical Bone

There are a handful of scanner and hardware prerequisites that need to be met prior to conducting NMR/MRI studies in human cortical bone. As previously mentioned, an NMR system with rapid T/R-switching is required to capture the fast-relaxing cortical bone signals. The Varian small animal imaging systems used herein have switching times as low as 4 μ s, which is more than sufficient for cortical bone studies. Common pulse sequences used to characterize the relatively slow relaxation in soft tissues need to be accelerated for cortical bone measurements, which requires some reprogramming on the Varian systems but is otherwise a straightforward task. Finally, the RF coil portion of the signal acquisition pathway needs to be made compatible for these types of measurements, which may require a considerable overhaul/redesign and is the focus of this chapter. Such is the case because conventional MRI coils are typically not designed for studies of rapidly relaxing species—they often contain proton-rich construction materials which may contribute confounding ^1H background signal during short- T_2 measurements. An example of this is shown herein. Separately, a loop-gap style coil was used to compare different coil

construction materials and configurations with respect to observed ^1H background signal sizes in a small animal imaging system. Background signal sources were spatially identified and quantified in a number of different coil configurations. It was found that the type and placement of structural coil materials around the loop-gap resonator, as well as the coil's shielding configuration, are critical determinants of the coil's background signal size. Although this study employed a loop-gap resonator design, these findings are directly relevant to standard volume coils commonly used for MRI.

2.1 — Background and Introduction: The RF Coil Problem

Modern magnetic resonance imaging techniques, such as the aforementioned ultra-short Echo Time (uTE) imaging (1), Sweep Imaging with Fourier Transformation (SWIFT) (2), and Water- and fat-suppressed projection MR imaging (WASPI) (3), allow the use of MRI for studying short- T_2 signals, such as ^1H signal from cartilage and cortical bone. Such imaging is sensitive to numerous background ^1H signals that are commonly overlooked in conventional MRI due to their short T_2 characteristics. For example, the proton-rich engineering plastics (4,5), adhesives, and lubricating oils present in standard RF coils may present a significant background signal when imaging on the timescales necessary for detecting short- T_2 signals. Similarly, other fast-relaxing ^1H sources throughout

the magnet bore may present problematic background signals, because their broad lineshapes may be excited by an RF pulse well off-resonance. Therefore, unwanted fast-relaxing background signals may originate from large areas both inside and outside the RF coil. With such a broad spatial distribution, components of the background signal may fold-over into the imaging field of view, confounding the underlying signal of interest. While gradient- and RF-based spatial selection techniques may avoid background signals in some cases, it is often impractical to maintain sensitivity to short- T_2 s with these techniques due to gradient strength and RF power deposition limits. Thus, for MRI of short- T_2 signals, it is desirable to minimize or shield all physical sources of background ^1H rather than relying on pulse sequence methods for filtering out the background NMR signal.

Herein, we identify and characterize background signal sources observable in a standard small bore imaging system and discuss approaches to lessen the contribution to short T_2 imaging, a requirement of cortical bone MRI. Additional coil design and practical testing experiences are presented in Appendix I. Given the widespread use of ^1H -bearing materials for in-bore MRI hardware, these results will aid investigators in devising effective means for

improving data quality by reducing background signal across a broad range of coil designs and short- T_2 pulse sequences.

2.2 — Experimental Methods: NMR Measurements and Coil Designs

All NMR studies were performed at 200 MHz using a 4.7T 31-cm horizontal bore Varian magnet (Varian Inc, Palo Alto, CA). The magnet bore was equipped with two concentrically nested gradient inserts: an outer 210 mm i.d. set, and an inner 120 mm i.d. set. All imaging measurements in this study used the outer gradient set, which allowed an imaging field of view large enough to include the inner gradient set. Constant time imaging (CTI), wherein every point in k-space is acquired at the same time, TE, after excitation (6), was used to acquire both 2D projections and full 3D images. Acquisition parameters included: 500 μ s gradient settling time prior to 4 μ s duration 20° hard excitation pulses, 15 μ s or 30 μ s TE (defined between midpoint of the excitation pulse and start of acquisition), a single-point acquisition at 1.25 MHz bandwidth, and 15 ms TR.

In order to demonstrate the background signal effects in a representative short- T_2 imaging scenario, 3D images of a 4.5 cm long segment of human cadaveric femur were acquired using a standard 63 mm i.d. birdcage-style coil (Varian Inc, Palo Alto, CA) with 30 μ s TE. A 10 cm x 10 cm x 15.2 cm field-of-view (FOV) (large enough to include the entire RF coil, Fig 2.1) was encoded with 50 x

50 x 76 samples in k-space. Data were zero-padded by 2x prior to reconstruction, resulting in 1 mm isotropic resolution. To mimic typical imaging where the FOV is only large enough to encompass the sample, a second 3D image was reconstructed after the k-space data were sub-sampled by a factor of 2x.

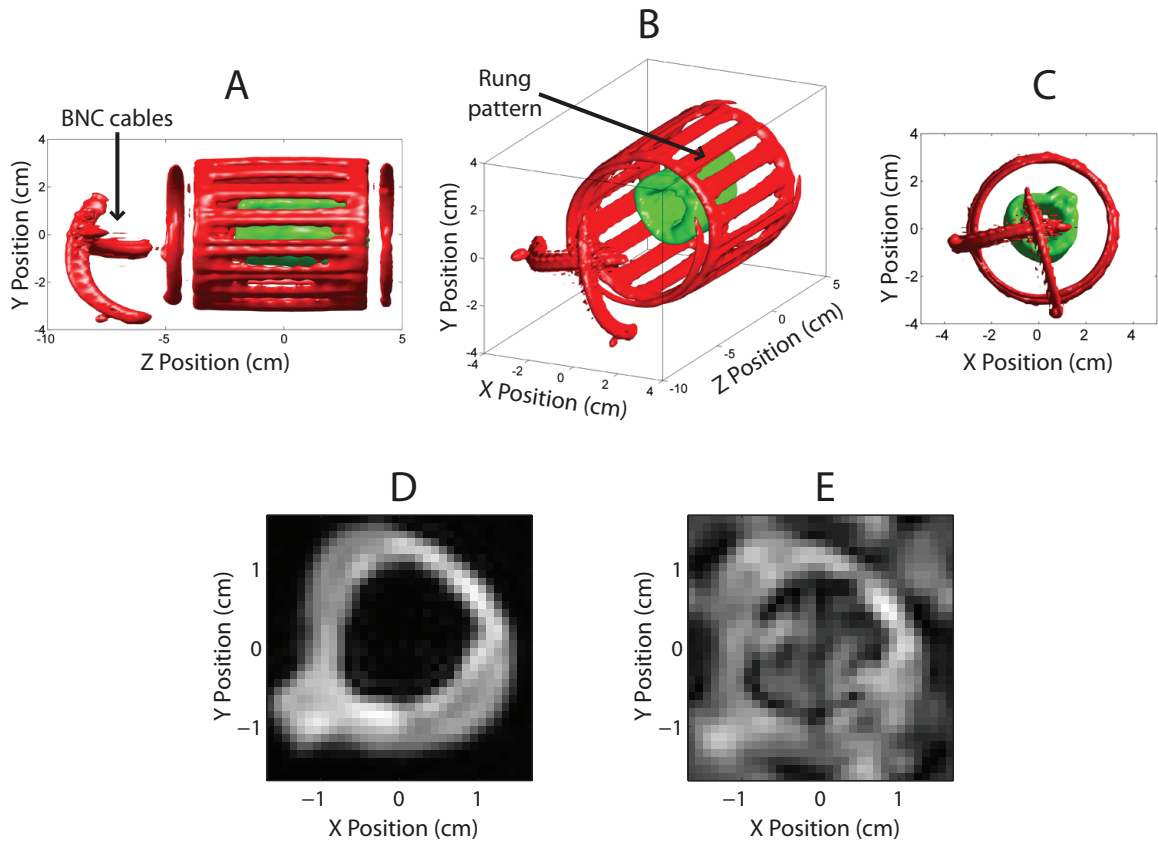


FIGURE 2.1 3D CTI of a human femur segment in a conventional volume imaging coil at 30 μ s TE. Isosurface renderings of coil components (red) surrounding the femur segment (green) are shown in sagittal (A), oblique (B), and axial (C) views. Axes in all images are expressed as distances from the coil isocenter. Background signal in the shape of the coil rung pattern is clearly seen, which presumably originates from the coil substrate plastics. BNC cables are also resolved. An axial slice from the 3D data is shown (D) in which the FOV has been cropped in image space, simulating a femur image over a conventional FOV in the absence of coil background signal. Coil background signal is introduced into the conventional FOV (E) by subsampling the 3D CTI k-space prior to image reconstruction, simulating a femur image analogous to D but in the presence of coil background signal. Via fold-over artifacts, the coil background signal severely degrades the femur region of interest.

To characterize potential short- T_2 signal contributions from different RF coil and/or sample holder materials, 2D and 3D images and non-localized free induction decays (FIDs) were collected using each of three variations of a 20 mm-diameter series-tuned loop-gap resonator (hereafter, Coils A, B, and C), built in-house (Fig 2.2). In all coils, high-purity copper ribbon was formed into the loop-gap shape; all electrical connections were made with a low-flux solder and cleaned with methanol; variable PTFE capacitors (Polyflon, Norwalk, CT) were used for tuning, matching, and balancing and B-type or C-type chip capacitors (American Technical Ceramics, Huntington Station, NY) were used for the main tank capacitance.

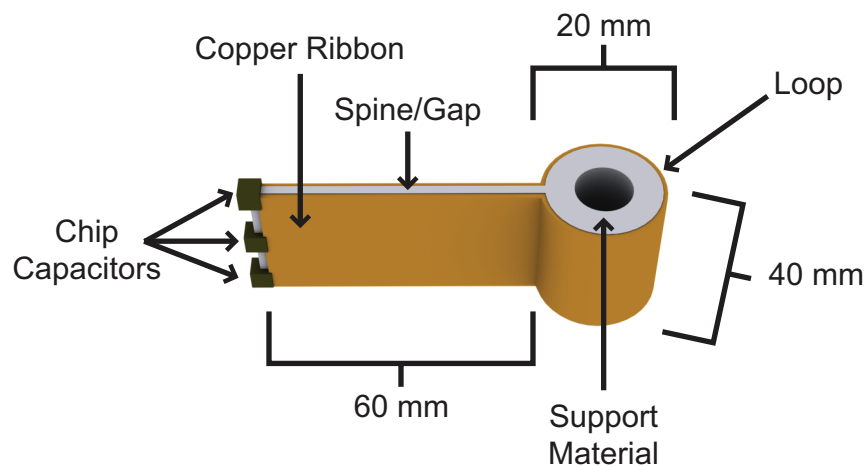


FIGURE 2.2 *Loop-gap resonator schematic.* Key resonator elements and dimensions are shown in a perspective view. With its 20 mm diameter and 40 mm height, the resonator can hold samples of up to ≈ 4 mL in its homogenous region.

Coil material selections, summarized in Table 2.1, were as follows: Coil A was built using polycarbonate pieces for the platform and coil support. Flexible polyethylene-based BNC cable was used as a transmission line, and the gap support was formed from copper-clad G-10/FR4 Garolite (McMaster-Carr, Atlanta, GA), an epoxy-bonded fiberglass. Polycarbonate and fiberglass are commonly used as structural materials for both small animal holders and volume coil forms, and, being relatively hard materials, might be assumed to have negligible background signal beyond a few microseconds. In Coil B, the polycarbonate and fiberglass materials were replaced with virgin PTFE (McMaster-Carr, Atlanta, GA) (i.e., “Teflon”, generally considered to be proton-free), and the common BNC cable was replaced with a PTFE-dielectric semi-rigid transmission line. In Coil C, the internal loop-gap support was removed and replaced with external support rings at the top and bottom of the coil. For all coils, a copper-clad mylar sheet with a 0.25 mm-thick copper layer was rolled, copper layer on the inside, around the entire coil assembly to form a full-coverage RF shield.

TABLE 2.1 *Material selections in the three loop-gap coil variants.*

	Coil A	Coil B	Coil C
Transmission Line	Polyethylene-dielectric BNC	PTFE-dielectric semirigid line	PTFE-dielectric semirigid line
Loop Support	Polycarbonate	PTFE	Air / external PTFE frame
Gap Support	Epoxy-bonded fiberglass	PTFE	Air / external PTFE frame
Coil Platform	Polycarbonate	PTFE	PTFE
Main Tank Capacitance	B-type chip caps	B-type chip caps	C-type chip caps

Transverse relaxation rates (R_2^*) of materials were measured using a pair of 2D CTI projections with TEs of 15 and 30 μ s. The FOV and number of samples varied between variations of the RF coil, but in each case the nominal in-plane resolution after 2x zero-padding was 2 mm x 2 mm. A coronal projection (parallel to long-axis of the loop gap, Fig 2.2) allowed unambiguous identification of different materials because there was no overlapping material in that direction. Three dimensional images were also acquired, with 15 μ s TE, 2 mm isotropic resolution and other parameters as defined above. For both the 2D and 3D images, the RF power was calibrated with a small water sample (0.1 mL, 6 mM CuSO_4), and then images were acquired from the coil in the absence of the water sample in order to best detect the background signals. To account for the varying

background signal amplitude between coils, between 4 (2D, Coil A) and 1150 (3D Coil C) excitations (NEX) were averaged. Finally, for each coil, with and without the 0.1 mL water sample, FIDs were collected (8 μ s 90° hard pulse, 4 μ s receiver dead-time, 5 MHz bandwidth, 15 s TR, 16-64 NEX) and linearly extrapolated to $t = 0$ (midpoint of excitation pulse) to provide a quantitative measure of the total background signal in units of water volume. Neglecting variation in T_1 -weighting between materials, the measured R_2^* s and total signal amplitudes were used to convert the 3D images into units of apparent proton density. This was an apparent, not absolute, measure because the 3D image volume encompassed a wide variation of RF sensitivity and the effect of transverse relaxation during RF excitation was not considered.

2.3 – Experimental Findings: RF Coil Background Signals and Self-portraits

Isosurface renderings of 3D images from the human femur segment in the 63 mm volume coil are shown in Figure 2.1a-c. In addition to the femur (green), signals from several coil elements such as plastic substrates of the birdcage rungs and BNC cables are clearly resolved (red) because of the large field of view. The total integrated signal from the bone and background were equivalent to 6.8 mL and 22.5 mL of water, respectively.

Rather than deconstruct the 63 mm volume coil, which was in routine use in the authors' lab, background signal characterization was conducted in three in-house loop-gap coils fabricated from known materials. The background signal amplitudes, expressed both as water equivalent volume and apparent proton density relative to water, as well as R_2^* values from various material in Coils A, B, and C are reported in Table 2.2.

TABLE 2.2 Sources of background signal in different loop-gap configurations. Various coil materials observed with CTI are reported with their observed T_2^* , apparent ^1H spin densities relative to the spin density of water, and total ^1H signal sizes. Observed signal sizes and spin densities depend on the excitation flip angle and will vary according to the coil's spatial sensitivity. As such, spin density of the gradient insert material was not determined (see Fig 2.4).

Proton Source	T_2^* (μs)	Apparent Spin Density/ H_2O	Signal Size ($\mu\text{L H}_2\text{O}$)
Polycarbonate Dielectric/Support ¹	7.5	0.85	6.1×10^3
Fiberglass Dielectric ¹	110	0.17	105
Gradient Insert ³	120	—	47
Polyethylene BNC Cable ¹	40	0.02	18
PTFE Dielectric/Support ²	20	3.4×10^{-4}	5.9
C-type Chip Capacitors ⁴	7.1	5.6×10^{-4}	1.0
PTFE Capacitors ⁴	15	4.0×10^{-4}	0.6
Laboratory Air ⁴	100	1.2×10^{-5}	0.1

¹ From shielded polycarbonate-based coil with total signal $\approx 6.4 \times 10^3 \mu\text{L H}_2\text{O}$

² From shielded PTFE-based coil with total signal $\approx 7.2 \mu\text{L H}_2\text{O}$

³ From unshielded PTFE-based coil with total signal $\approx 55 \mu\text{L H}_2\text{O}$

⁴ From shielded copper-in-air coil with total signal $\approx 2.1 \mu\text{L H}_2\text{O}$

The total background signal in coil A was equivalent to ≈ 6.4 mL H₂O, compared with the ≈ 4 mL uniform RF field volume. Each of the coil construction materials was clearly visible in CTI images (Fig 2.3a), with the dominant source of signal arising from polycarbonate plastic inside the coil's loop. Coil B was built by replacing coil A's proton-bearing materials with low-proton PTFE, resulting in a much reduced background signal equivalent to ≈ 7.2 μ L H₂O, which originated predominantly from PTFE in the loop and gap (Fig 2.3b). Coil C was built with all PTFE materials placed external to the loop and gap, further reducing the background signal to ≈ 2.1 μ L H₂O, which arose predominantly from variable PTFE and fixed chip capacitors (Fig 2.3c). The localization of signals at the top and bottom of Coil C's loop and gap (Fig 2.3c, sagittal view) likely corresponded to the PTFE external support frame. It should be noted that the C-type chip capacitors in Coil C contributed a larger apparent signal than the physically smaller B-type capacitors in Coil B.

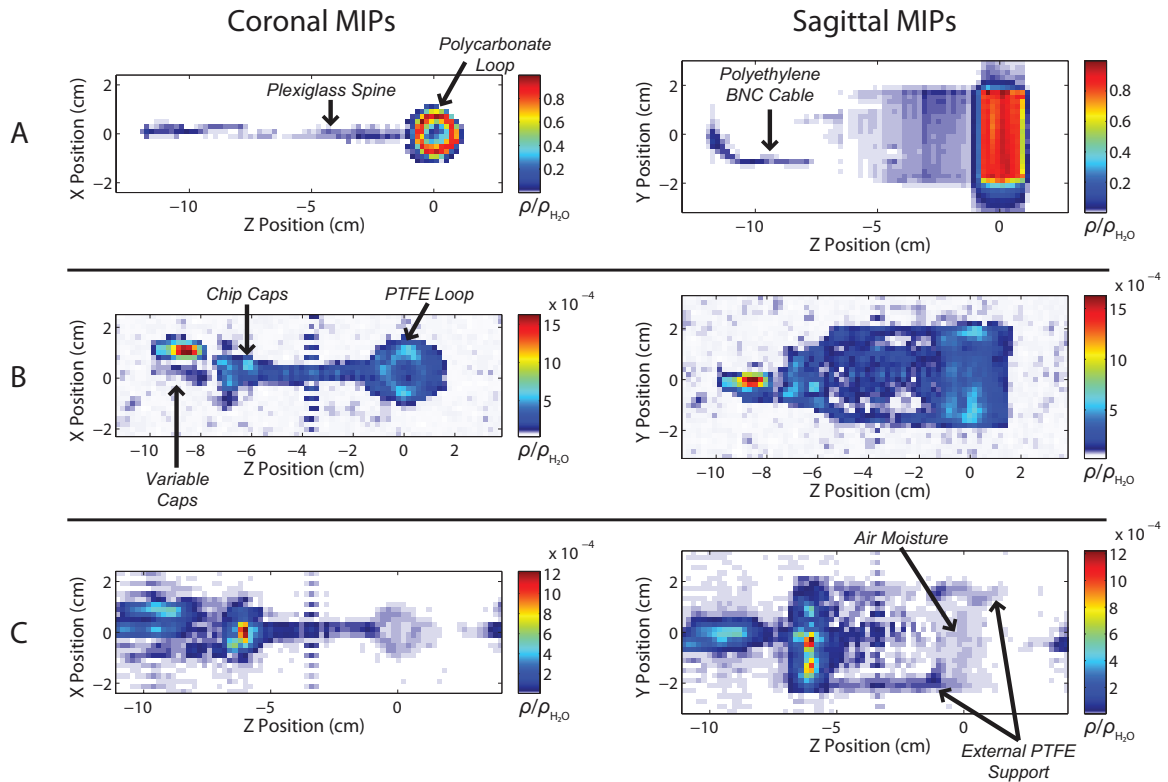


FIGURE 2.3 *Maximum intensity projections (MIPs) from 3D CTI of different loop-gap coil configurations.* Coronal (left) and sagittal (right) MIPs are shown for the polycarbonate-based coil (A), PTFE-based coil (B), and copper-in-air coil (C). For comparison of all coils, color scales are expressed in units of spin density, normalized to the spin density of water ($\rho/\rho_{\text{H}_2\text{O}}$, see text for details). Axes in all images are expressed as distances from the coil isocenter. Images are shown in the same orientation as in Figure 2.2. Materials such as capacitors and BNC cable are labeled for reference. Note that the small region of signal to the right of the loop in C is capacitor-related signal wrapped around from the far left side of the FOV. Also, the spatial banding artifacts originating from the center of the FOVs in B and C were attributed to coil ringing and were excluded from signal quantitation.

RF shielding was also investigated as a means to reduce stray background signals originating from outside of the coil. Bench testing of the unshielded coil B with a network analyzer (relevant to any of the loop-gap coils studied) showed that a 90° RF pulse resulted in $\approx 2^\circ$ RF at the inner gradient bore, which can

potentially excite proton-bearing materials in the gradient insert. This effect is seen in practice (Fig 2.4), where CTI projections from the PTFE-based coil without the RF shield in place reveal a spatially broad signal originating from the gradient insert. This signal amplitude was equivalent to approximately 50 μL of H_2O (Table 2.2), was only partially removed by a slotted RF shield (as is often used to avoid adding material area in which eddy currents can be generated), but was effectively entirely removed by the full coverage RF shield.

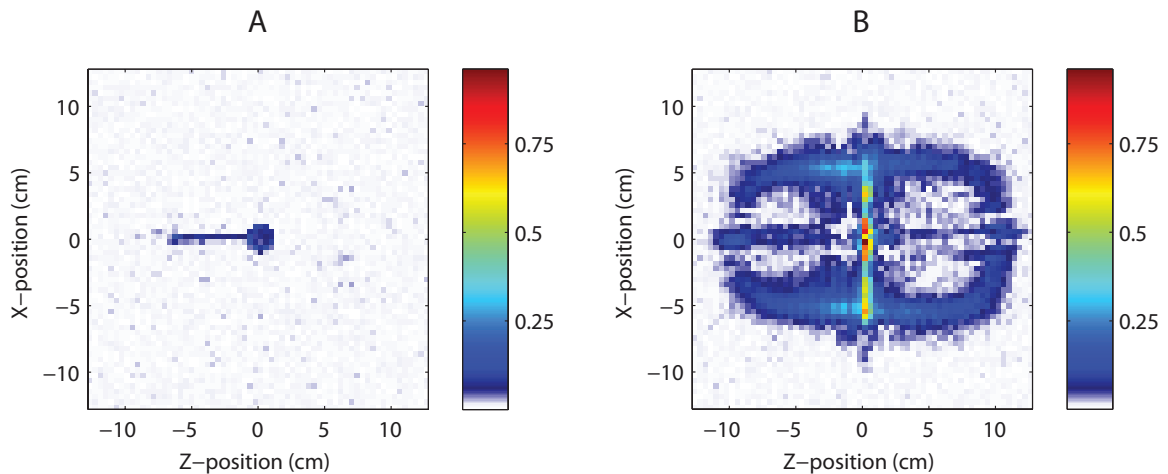


FIGURE 2.4 *Effects of RF coil shielding on background signal.* 2D CTI projections of the PTFE-based coil are shown in the presence (A) and absence (B) of a full-coverage RF shield. Since these images were formed from 2D CTI projections, image intensity cannot be readily converted to spin density as in Figure 2.3 because of a lack of spatial depth information. As such, the images are shown on the same, normalized color scale. Nonetheless, it is clear that the RF shield eliminates a significant amount (see Table 2.2) of unwanted signal from outside the coil.

2.4 — Discussion: Considerations of Coil Materials and Placement

Short- T_2 imaging of a human femur with a conventional volume coil indicates that, even at $TE = 30 \mu s$, the coil background signal cannot be ignored. To demonstrate the potential effect of ignoring the background signal, compare Fig 2.1d and 2.1e. Fig 2.1d shows a single slice through the 3D volume, presenting a cross-sectional view of the femur and cropped to remove the background signals. This is representative of a bone image in the ideal case where no background signal exists. In contrast, Fig 2.1e shows the corresponding image that resulted when the acquisition FOV was reduced by down-sampling k-space. In this case the FOV was not large enough to encompass the entire RF coil and the signal from its proton-bearing material is aliased back into the image. Note that the nature of such aliasing depends on the k-space sampling scheme and will generally create incoherent artifacts for the non-cartesian sampling (7) common to many short- T_2 imaging methods.

Coil A, which was built from commonly used construction and sample holder materials to emulate the conventional volume coil, exhibits a prohibitively large background signal equivalent to 60% more water than can be contained in the coil's RF-homogenous volume. In Coil B, a simple substitution of the coil materials with low-proton PTFE yields a thousand-fold drop in the net

background signal. The remainder of Coil B's signal, dominated by PTFE materials inside the loop and gap (Fig 2.3b), is consistent with a previous study showing that PTFE contains a trace proton NMR signal (8). Coil C minimizes this PTFE signal by moving all PTFE supports to external locations around the resonator, resulting in a final background signal equivalent to $\approx 2.1 \mu\text{L H}_2\text{O}$, which is approximately $1/3000^{\text{th}}$ the size of the coil's RF-homogenous volume.

To put the size and T_2^* values of these background signals into context, consider that uTE signals are derived from a combination of solid/macromolecular protons and the protons from water bound to these macromolecules. Quantitative magnetization transfer studies and compositional analysis in numerous tissues point to solid proton $T_2^* \approx 10 \mu\text{s}$ (9) and bound water T_2 or $T_2^* \approx 50\text{-}500 \mu\text{s}$ (10-12), with concentrations relative to bulk water $\approx 0.05\text{-}0.5$ (9,13). Thus, the fiberglass, gradient insert, and BNC cable signals pose the greatest concern for uTE images with relatively long echo times ($TE \geq 80 \mu\text{s}$), which tend to image bound water signals. When imaging with much shorter echo times (14,15), or with SWIFT ($TE \approx 0$) (2), any of the background signals are long enough lived to contribute to the image, but the polycarbonate, fiberglass, and to a lesser extent, the BNC cable are the most problematic due to their relatively large apparent proton densities. PTFE components and C-type chip

capacitors may present significant signal when looking at solid signals from small samples. For example, the solid proton signal ($T_2^* \approx 10 \mu\text{s}$) from a 0.25 mL sample of human cortical bone has a signal equivalent to $\approx 40 \mu\text{L H}_2\text{O}$ (Table 2.2), as estimated from a previous study (16), which would be significantly corrupted by the apparent $\approx 6 \mu\text{L}$ signal from the PTFE loop support in Coil B.

In general, the relevant threshold for an acceptable background signal when studying short T_2 signals primarily depends on the sample size and RF coil geometry. It is expected that a linear increase in RF coil dimensions (diameter and length) results in a correspondingly linear increase in the amount of coil construction materials and, therefore, a linear increase in the short- T_2 background signal. However, this linear increase in coil size corresponds to an approximate cubic increase in uniform RF volume. For example, in comparing the signals of the 63-mm coil and Coil A we see $\approx 3\times$ difference in linear dimensions, $\approx 3.5\times$ difference in background signal amplitudes, and $\approx 24\times$ difference in uniform RF volume. Hence, the background signal problem is greatest for small samples and coils. For moderate to large RF coils ($> 6 \text{ cm}$ diameter) and samples that are close to filling the uniform RF volume, it may be sufficient to avoid proton-rich materials within the RF coil and along the entire in-bore electrical signal pathway. However, for small samples and coils, it will

also be necessary to minimize the PTFE near the RF coil volume, use high-grade low-proton capacitors, and robustly shield the coil from external NMR signals. Additionally, the proton content of any non-PTFE coil construction materials inside the shielded region should be carefully considered. For commonly-used materials not employed in this study, the reader is directed to previous studies that have identified short-lived signals from plastics such as polypropylene (4) and acrylic (17), as well as longer-lived ($T_2 \approx 2$ ms) signals from acrylonitrile-butadiene-styrene (ABS) and commercial coil casing plastics (18). Furthermore, foams and tapes used for sample placement and positioning cannot be neglected when assessing net background signal.

In addition to coil materials, RF shielding was found to be important for reducing background signal. The 120 mm i.d. gradient insert, like all common magnetic field gradient constructions, contains numerous proton-bearing materials such as fiberglass, epoxy, and water coolant. Although well outside the uniform region of the RF coil, these materials were found to contribute significant signal in the absence of the full coverage RF shield, increasing the background signal of Coil B nearly 8-fold. A full-coverage RF shield was necessary to block signals from the gradient insert, as any gaps in the shield conductor permitted extraneous NMR signals.

Finally, it is worth noting that in Coil C and using the full RF shield, a signal persisted throughout the center of coil's apparently vacant loop (Fig 2.3c). This signal amplitude was consistent with water vapor at 66% relative humidity (100% humid air at 20°C is $\approx 1.2 \text{ kg/m}^3$, holds $\approx 1.5 \%$ w/w water (19), and thus contains $\approx 1.8 \times 10^{-5} \text{ g H}_2\text{O/mL}$), approximately the expected lab humidity, and was removed by purging the magnet bore with dry nitrogen gas. This implies that the humidity of laboratory air may set the ultimate lower-limit for background signals from freestanding, unenclosed coil designs.

2.5 – Conclusions

In a series of RF coil constructions for short- T_2 MRI, it was found that material selection, placement, and shielding were important design parameters for mitigating total coil background signal. For minimal background signal, we recommend that the coil designer 1) use only low proton density materials such as PTFE, and in minimal possible quantity, in the immediate vicinity of the resonator and in-bore RF path, 2) likewise, utilize only low-proton RF electrical components such as PTFE-based BNC cables and small ceramic chip capacitors throughout the in-bore RF path, and 3) encase the resonator with an inward-facing full-coverage RF shield to attenuate stray NMR signals from outside the coil. Since the coil background signal generally becomes less significant as NMR

sample size is increased, the first recommendation may be sufficient when using large coils and samples (> 6 cm diameter), but for study in small animals and tissue specimens, signals from BNC cables and the gradient insert may also be significant. Using these principles, a variety of coils have been fabricated (Fig 2.5) and are now in use at the Vanderbilt University Institute of Imaging Science Center for Small Animal Imaging.

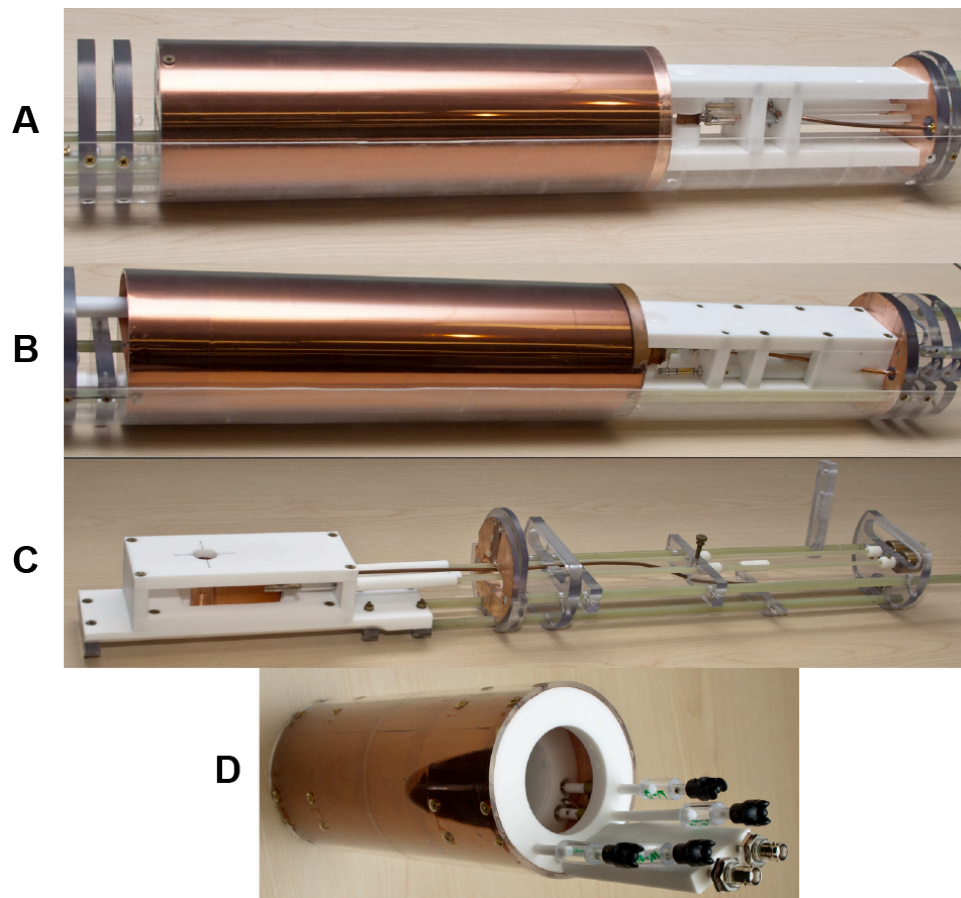


FIGURE 2.5 *Low-¹H coils available on the in-house small animal magnets. Loop-gap coils are available with a 5 mm or 15 mm diameter at 400 MHz (A, interchangeable resonators), a 10 mm diameter at 200 MHz (B), and a 20 mm diameter at 200 MHz (C). A shielded, 16-rung, quadrature low-pass birdcage with 63 mm inner diameter is also available at 200 MHz for volume imaging (D). Copper-colored foil is the shield material.*

2.6 — References

1. Gatehouse PD, Bydder GM. Magnetic resonance imaging of short T-2 components in tissue. *Clinical Radiology* 2003;58(1):1-19.
2. Idiyatullin D, Corum C, Park JY, Garwood M. Fast and quiet MRI using a swept radiofrequency. *J Magn Reson* 2006;181(2):342-349.
3. Wu YT, Ackerman JL, Chesler DA, Graham L, Wang Y, Glimcher MJ. Density of organic matrix of native mineralized bone measured by water- and fat-suppressed proton projection MRI. *Magnetic Resonance in Medicine* 2003;50(1):59-68.
4. Marjanska M, Waks M, Snyder CJ, Vaughan JT. Multinuclear NMR investigation of probe construction materials at 9.4T. *Magnetic Resonance in Medicine* 2008;59(4):936-938.
5. Springer F, Martirosian P, Schwenzler NF, Szimtenings M, Kreisler P, Claussen CD, Schick F. Three-Dimensional Ultrashort Echo Time Imaging of Solid Polymers on a 3-Tesla Whole-Body MRI Scanner. *Investigative Radiology* 2008;43(11):802-808.
6. Emid S, Creyghton JHN. High-Resolution Nmr Imaging in Solids. *Physica B & C* 1985;128(1):81-83.
7. Bernstein MA, King KF, Zhou ZJ. Handbook of MRI pulse sequences. Amsterdam ; Boston: Academic Press; 2004. p. 932-935 p.
8. Bachman HN, Silvera IF. Impurity proton NMR signals from common "proton-free" laboratory materials. *Journal of Magnetic Resonance* 2003;162(2):417-422.
9. Stanisz GJ, Odrobina EE, Pun J, Escaravage M, Graham SJ, Bronskill MJ, Henkelman RM. T-1, T-2 relaxation and magnetization transfer in tissue at 3T. *Magnetic Resonance in Medicine* 2005;54(3):507-512.
10. Schreiner LJ, Cameron IG, Funduk N, Miljkovic L, Pintar MM, Kydon DN. Proton NMR spin grouping and exchange in dentin. *Biophys J* 1991;59(3):629-639.
11. Fantazzini P, Brown RJS, Borgia GC. Bone tissue and porous media: common features and differences studied by NMR relaxation. *Magn Reson Imaging* 2003;21(3-4):227-234.
12. Robson MD, Bydder GM. Clinical ultrashort echo time imaging of bone and other connective tissues. *Nmr in Biomedicine* 2006;19(7):765-780.

13. Dubinskaya VA, Eng LS, Rebrow LB, Bykov VA. Comparative study of the state of water in various human tissues. *Bulletin of Experimental Biology and Medicine* 2007;144(3):294-297.
14. Wu YT, Dai GP, Ackerman JL, Hrovat MI, Glimcher MJ, Snyder BD, Nazarian A, Chesler DA. Water- and fat-suppressed proton projection MRI (WASPI) of rat femur bone. *Magnetic Resonance in Medicine* 2007;57(3):554-567.
15. Du J, Bydder M, Takahashi AM, Chung CB. Two-dimensional ultrashort echo time imaging using a spiral trajectory. *Magnetic Resonance Imaging* 2008;26(3):304-312.
16. Horch RA, Nyman JS, Gochberg DF, Dortch RD, Does MD. Characterization of ¹H NMR Signal in Human Cortical Bone for Magnetic Resonance Imaging. *Magnetic Resonance in Medicine* 2010; In Press.
17. Kennedy CB, Balcom BJ, Mastikhin IV. Three-dimensional magnetic resonance imaging of rigid polymeric materials using single-point ramped imaging with T-1 enhancement (SPRITE). *Canadian Journal of Chemistry-Revue Canadienne De Chimie* 1998;76(11):1753-1765.
18. Widmaier S, Jung W-I, Pfeffer K, Pfeffer M, Lutz O. MRI and determination of T1 and T2 of solid polymers using a 1.5 T whole-body imager. *Magnetic Resonance Imaging* 1993;11(5):733-737.
19. J. M. Smith HCVN, Michael Abbott, Hendrick Van Ness. *Introduction to Chemical Engineering Thermodynamics*: McGraw-Hill; 2000. 816 p.

CHAPTER 3

Biophysical Basis of Transverse Relaxation in Cortical Bone

Recent advancements in MRI have enabled clinical imaging of human cortical bone (re: Chapter 1.4), providing a potentially powerful new means for assessing bone health with molecular-scale sensitivities unavailable to conventional X-ray-based diagnostics. In cortical bone, MRI is sensitive to populations of protons (^1H) partitioned among water and macromolecular sources, which may be differentiated according to intrinsic NMR properties such as chemical shift and transverse and longitudinal relaxation rates. In this chapter, these NMR properties were assessed in human cortical bone donors from a broad age range, and four distinct ^1H populations were consistently identified and attributed to five microanatomical sources. These findings show that modern cortical bone MRI contrast will be dominated by collagen-bound water, which can also be exploited to study bone collagen via magnetization transfer.

3.1 — Background and Introduction: A Basis for Bone NMR

As the skeleton ages, the risk of fracture increases. This increasing propensity to fracture is not solely due to the well documented loss of bone mass with aging,

but also to a deterioration in material strength and toughness of bone (bone quality) (1). As discussed in Chapter 1.3, clinical measurements of bone mass by gold-standard dual energy X-ray absorptiometry (DXA) are relatively insensitive to soft tissue characteristics in bone such as water molecule distribution, which has been conclusively linked to the energy dissipation mechanisms of the bone matrix (2-8) and likely plays a pivotal role in bone quality. Unlike X-ray based imaging modalities, MRI is highly sensitive to the water microenvironment in tissue, as well as other molecular sources of ^1H , and offers the potential to non-invasively evaluate the fracture resistance of bone. While conventional MRI methods are not suitable for imaging cortical bone because of its low proton density and short transverse relaxation time constants (T_2), the ultra-short echo time (uTE) and related MRI methods reviewed in Chapter 1.4 have opened clinical MRI to hard tissue imaging (9-11). Recently these methods have produced high quality images of human cortical bone (10,12) and raised the question of what bone characteristics can be derived from such images.

Presented herein is a phenomenological and biophysical characterization of the uTE MRI-visible ^1H NMR signal of cortical bone. Specifically, unique contributions to the net bone NMR signal are determined for both bound and mobile water, lipids, and bone matrix collagen. Knowledge of these signal

contributions and their NMR properties is critical for future development and interpretation of cortical bone MRI and may form the foundation for a novel diagnostic of bone health.

Recalling from Chapter 1.1, cortical bone is a composite of collagen, minerals, lipids, and pore spaces that are arrayed in repeating units of osteons (13-15). Distinct proton micro-environments are expected in each of these constituents but are too small to be spatially resolved with clinical MRI.

However, their ^1H NMR signal contributions may be resolved by decomposing the net NMR signal into chemical shift and relaxation components. Presented here is a series of NMR measurements at 4.7 T, relevant signal decompositions, and physical manipulations of cortical bone specimens from cadaveric donors to identify common signal components and their micro-anatomical origins.

3.2 — Experimental Methods: Human cortical bone preparation

The Musculoskeletal Tissue Foundation (Edison, NJ), a non-profit tissue allograft bank, and the Vanderbilt Donor Program (Nashville, TN) supplied human femurs from six cadaveric donors (four male, two female, aged 21-94 years old, mean \pm standard deviation: 60 ± 31 years) under instruction to not provide tissue from donors who had tested positive for a blood borne pathogen (e.g., HIV or Hepatitis C). One cortical bone specimen was extracted from the medial mid-

shaft of each donor's right femur and was machined to 15x5x5 mm dimensions via end mill. During dimensioning, care was taken to remove endosteal and periosteal surfaces such that the final specimens for NMR measurement were pure cortical bone. Specimens were stored in phosphate-buffered saline at -20 °C between processing and NMR measurements, and specimens were thawed at 4 °C approximately 18 hours prior to NMR measurements. Immediately prior to NMR measurements, thawed specimens were removed from PBS and blotted dry to remove the large amount of pooled surface water that remained. Specimens endured no more than three freeze-thaw cycles, and separate experiments found that up to six freeze-thaw cycles had negligible impact on the NMR properties. Final cortical bone dimensions were measured with digital caliper for volume determination.

3.3 — Experimental Methods: Micro-computed tomography (μ CT)

μ CT was performed on 2x4x4 mm cortical bone specimens (harvested adjacent to NMR specimen femoral sites) with a Scanco μ CT 40 scanner (Scanco Medical, Switzerland) at 6 μ m voxel size, which was sufficient to image the Haversian canals and other vascular porosity. The osteons of the cortical specimen were aligned with the scanning axis using the standard specimen tube. A portion of each specimen (2.4 mm in length) was scanned acquiring 1000 projections per

180°. X-ray source settings did not vary among the specimens. After reconstruction, the Scanco thresholding procedure segmented bone tissue from air or soft tissue. Applying the Scanco evaluation software to the cortical bone, we quantified porosity, defined as one minus cortical bone volume per total volume.

3.4 — *Experimental Methods: NMR measurements*

The cortical bone specimens were initially assessed with measurements of their ^1H NMR resonance spectra and transverse relaxation (T_2) decays, probing NMR signal decay features that dominate uTE MRI contrast. NMR measurements were performed in a Varian 4.7T horizontal bore magnet with a Direct Drive Receiver (Varian Medical Systems, Palo Alto, CA). An in-house loop-gap style RF coil (lowest- ^1H design in Chapter 2) was used with Teflon structural support, which gave negligible background ^1H signal ($\approx 1\%$ of net bone signal). Pulse sequences used 90° excitation pulses of $\approx 8 \mu\text{s}$ duration and (where relevant) 180° refocusing/inversion pulses of $\approx 16 \mu\text{s}$ duration. Free induction decays (FIDs) were collected at 5MHz bandwidth and 20Hz nominal spectral resolution from a pulse-acquire sequence, with an $8\mu\text{s}$ dead time after excitation to allow for coil ringing to subside. Four excitations were averaged using a $90_{(x,-x,y,-y)}$ phase cycling scheme. Resonance spectra were calculated from FIDs by discrete Fourier

transform and manual phasing. To characterize T_2 , Carr-Purcell-Meiboom-Gill (CPMG) (16) measurements with a total of 10000 echoes were collected at 100 μs echo spacing (first echo at $TE = 100 \mu\text{s}$), yielding data which were fitted with a T_2 spectrum (details below). Four excitations were averaged using a $90_{(x,-x,x,-x)}/180_{(y,y,-y,-y)}$ phase cycling scheme. Echo spacing was minimized while avoiding spin locking effects, which manifested as prolonged apparent T_2 s when echo spacing $< 100 \mu\text{s}$. In all measurements, specimens were placed with osteonal direction orthogonal to B_0 to avoid altering any potential magic angle effects across measurements.

Further investigation of both the FID and CPMG signal included three additional NMR studies: 1) Inversion recovery-prepared CPMG (IR-CPMG), 2) T_2 - T_2 relaxation exchange spectroscopy (REXSY) (17), and 3) dynamic study of FID and CPMG signal responses to D_2O immersion. The IR-CPMG measurements involved an inversion-recovery (IR) preparation with variable recovery time preceding a CPMG acquisition, as described above. Twenty-four recovery times, log-spaced between 1 ms and 10 sec, were used for each sample and the resulting data were fitted with a 2D T_1 - T_2 spectrum (18) (details below). The REXSY measurements involved a CPMG-like preparation with variable number of echoes (NE) followed by a storage/mixing period then a CPMG

acquisition, as described above. Thirty-two different CPMG preparations were used with echo spacing of $100\mu\text{s}$ and NE pseudo-log spaced between 1 and 1000. For all acquisitions, the mixing period was 200 ms, and the resulting data were fitted with a T_2 - T_2 spectrum. REXSY measurements used an additional phase cycle of the storage pulse (to store T_2 -prepared magnetization on the $\pm z$ axis during the mixing period), resulting in a total of 4 averaged excitations. (For further details on using REXSY for exchange measurements see (19)). Finally, after all aforementioned NMR measurements, specimens were placed in an isotonic D_2O solution to study effects of proton-deuteron exchange on NMR properties for determination of proton origins. This solution was made by mixing a volume of 99.9% isotopic purity D_2O (Sigma-Aldrich Corp., St. Louis, MO) with the appropriate mass of PBS electrolyte tablets (MP Biomedicals, Solon, OH) to yield 1x PBS. Each bone specimen was immersed in a volume of isotonic PBS that was 100x larger than the specimen volume, and immersed specimens were maintained on a 60 RPM shaker table at $4\text{ }^\circ\text{C}$ until steady state was achieved (as determined by monitoring NMR resonance spectra). Final NMR measurements were then collected for comparison to initial measurements.

3.5 — *Experimental Methods: NMR Data Fitting*

After phasing, real-valued NMR resonance spectra were fitted to a sum of three Lorentzian lineshapes with a constrained Levenberg–Marquardt algorithm. For each spectrum, visual inspection provided initial guesses of linewidths and frequency offsets so as to improve algorithm convergence, and final inspections of residuals and mean square errors verified proper fitting.

The 10000 CPMG echo magnitudes were down-sampled in a pseudo-log fashion to 1024 echoes and fitted to a sum of 128 decaying exponential functions (with time constants log-spaced between 20 μ s and 10 sec) in a non-negative least-squares sense, subject to a minimum curvature constraint, which produced a so-called T_2 spectrum (20). IR-CPMG data were reduced by singular-value decomposition (21) prior to two-dimensional non-negative least squares fitting (18) to the aforementioned range of decaying exponentials, producing a so-called T_1 - T_2 spectrum. REXSY data were processed in a similar manner, yielding T_2 - T_2 spectra. All data processing was performed with MATLAB (The Mathworks, Natick, MA). Results are presented as mean \pm one standard deviation across samples.

In order to quantitatively compare the absolute signal amplitudes of T_2 spectra across specimens and days, a 20 μ L H_2O reference sample with long T_2

(≈ 2.5 s) was included in each CPMG measurement. This reference sample, together with its known molar ^1H density and the known specimen volumes, enabled the calculation of proton concentrations in the bulk bone specimens for each CPMG relaxation component by comparing integrated areas of each T_2 spectral component to the area of the marker. No such reference was used during resonance spectrum measurements, but the inter-measurement standard deviation of the reference sample's signal intensity was 4.8 %, so it was concluded that the absolute amplitudes of the resonance spectral components were reliable to approximately this degree of precision.

3.6 — Experimental Findings: Decomposition of the Bulk Bone NMR Signal

FID-derived NMR resonance spectra (Fig 3.1, A and B) revealed three distinct signal components, as determined by Lorentzian fitting: two relatively narrow-band, slow-relaxing chemically-shifted components were consistently observed atop a broad-band, fast-relaxing component. In all specimens, the narrow-band component linewidths were < 5 ppm and the broad-band component linewidths were > 100 ppm, giving clear discrimination between slow- and fast-relaxing species. The dominant narrow-band component accounted for 57.7 ± 3.9 % of the total FID signal. The second narrow-band component was consistently chemically shifted from the first component by -4.0 ± 0.2 ppm and represented

4.6 ± 3.2 % of the FID signal. The broadband component accounted for the remaining 33.7 ± 2.5 % of the FID signal and had a -33 ± 6.8 ppm chemical shift from the dominant narrow-band component. T_2^* s of 736 ± 46 μ s, 1700 ± 470 μ s, and 11.8 ± 1.1 μ s for the on-resonant narrow-band, off-resonant narrow-band, and broad-band components, respectively, were calculated from the components' linewidths.

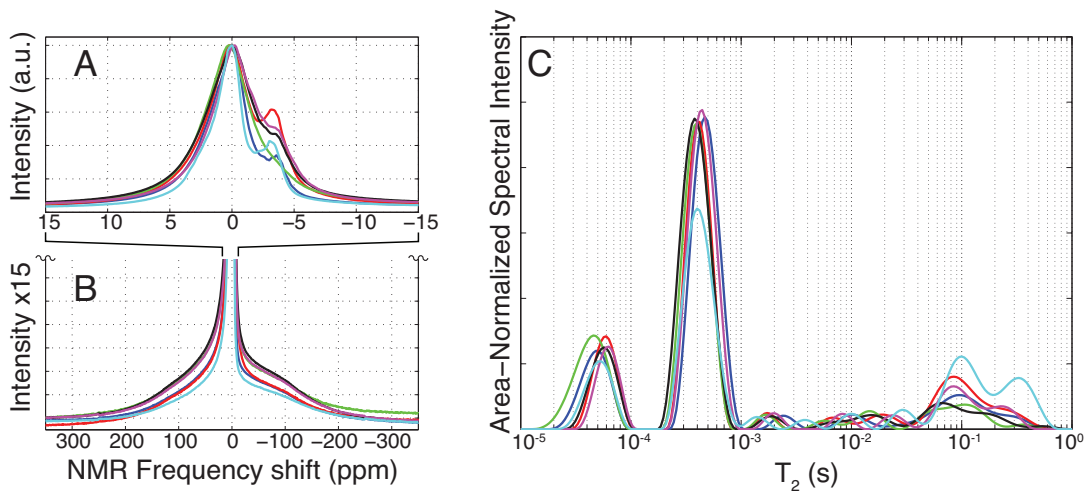


FIGURE 3.1 *Wideline NMR and multiexponential T_2 spectroscopy of human cortical bone specimens.* NMR spectroscopy of human cortical bone specimens over narrow (A) and broad (B) bandwidths generally showed three frequency components in all samples: an off-resonant, narrow-band frequency component at -4.0 ± 0.2 ppm (fat shifted) and on-resonant narrow-band and broad-band components. Spectra in (B) are magnified 15-fold in the vertical axis of (A) and are vertically cropped for display purposes. Multiexponential T_2 spectroscopy of human cortical bone (C) reveals two well-defined T_2 pools at 57 ± 4 μ s and 416 ± 35 μ s and a broad distribution of T_2 components spanning 1 ms to 1000 ms. All spectra were normalized to maximum intensity (A, B) or total integrated area (C).

Fig 3.1C shows CPMG-derived T_2 spectra from each cortical bone specimen, demonstrating two distinct sub-millisecond relaxation components

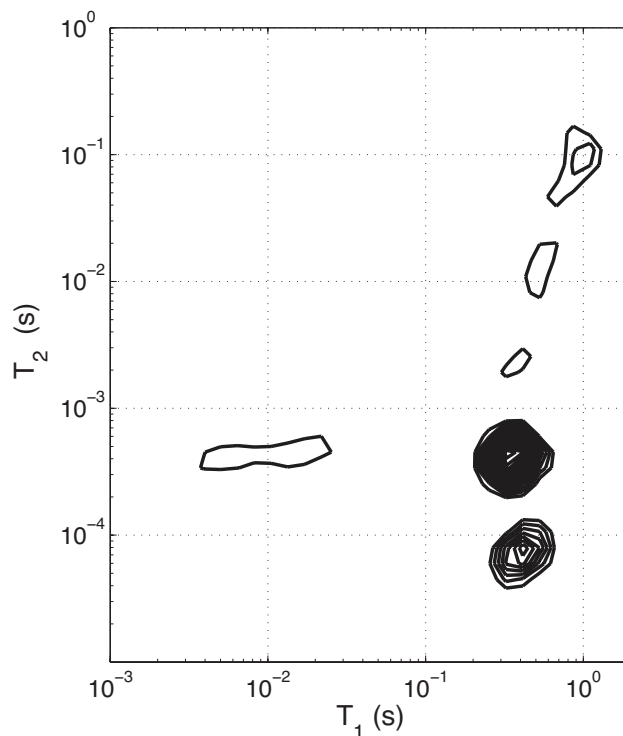
and a broad collection of signals spanning the millisecond-second T_2 domain, which hereafter is collectively considered a third T_2 component for discussion purposes. The two sub-millisecond components had T_2 s of $57 \pm 4 \mu\text{s}$ and $416 \pm 35 \mu\text{s}$, with respective CPMG bone signal fractions of $16.1 \pm 1.3 \%$ and $60.8 \pm 5.3 \%$. The long-lived third T_2 component accounted for the remaining $23.0 \pm 6.5 \%$ of the CPMG signal. Comparing these signal fractions to the concomitantly-measured T_2 marker (see *NMR Data Fitting*) gave proton concentrations of 6.6 ± 1.5 , 24.8 ± 5.8 , and $9.2 \pm 2.3 \text{ mol } ^1\text{H}/\text{L}_{\text{bone}}$ for the $\approx 60 \mu\text{s}$, $\approx 400 \mu\text{s}$, and long-lived T_2 components, respectively. Note that typical CPMG data signal-to-noise ratio was ≈ 7000 (integrated spectral area divided by the standard deviation of the residuals from the T_2 spectrum fit), which was ample to fit the observed $60 \mu\text{s}$ T_2 component. In preliminary studies, general characteristics of both resonance and T_2 spectra did not change substantially between 0.5 T and 9.4 T static magnetic field strengths (data not shown), so the three FID and three CPMG signal components should be relevant to all mainstream laboratory and clinical cortical bone NMR.

For all bone specimens, T_1 - T_2 spectra from IR-CPMG measurements (Fig 3.2) showed T_1 values ranging from $\approx 350 \text{ ms}$ for the two short-lived T_2 components to $\approx 1 \text{ s}$ for much of the long-lived T_2 component. A bi-exponential T_1

relaxation for the $\approx 400 \mu\text{s}$ T_2 component was consistently observed, characteristic of magnetization transfer (MT) between this component and a shorter- T_2 proton pool (22). Observable T_2 proton pools participating in this MT were identified from REXSY T_2 - T_2 spectra (Fig 3.3). The main diagonal in the T_2 - T_2 spectrum is analogous to the 1D CPMG-derived T_2 spectrum, while off-diagonal signals arise from an exchange of magnetization between T_2 components during the 200 ms mixing period (similar to EXSY experiments in chemical-shift resolved studies (23)). As such, REXSY consistently indicated exchange between the two short-lived T_2 components ($\approx 60 \mu\text{s}$ and $\approx 400 \mu\text{s}$). No significant exchange involving the long-lived T_2 signals was observed in any of the samples.

FIGURE 3.2 *2D T_1 - T_2 Spectra.*

Typical results from IR-CPMG data are shown, wherein the T_1 relaxation time(s) for each T_2 component may be identified after a 2D inverse Laplace transform. Note that all T_2 components are monoexponential in T_1 except for the $400 \mu\text{s}$ T_2 , which results from magnetization transfer with a shorter-lived T_2 component.



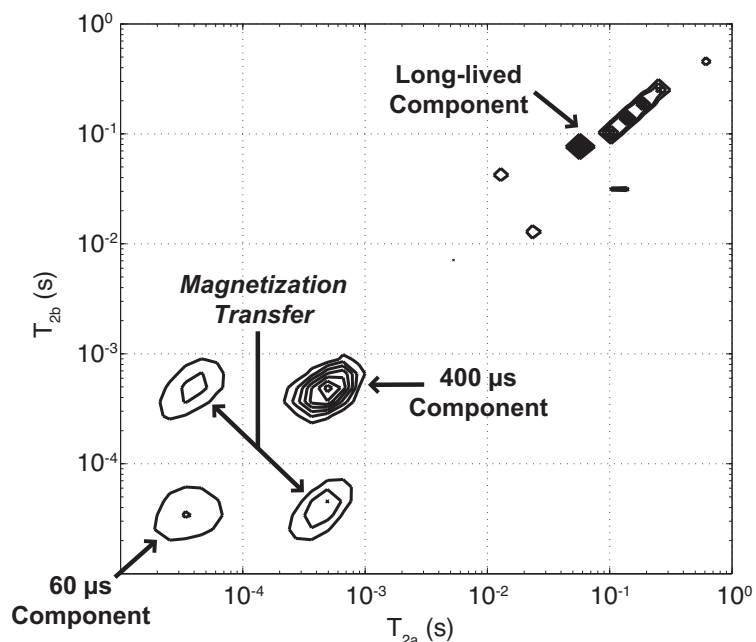


FIGURE 3.3 2-D exchange spectroscopy (REXSY) representative of all human cortical bone specimens. Each of the three T_2 components appear on the main diagonal (running lower-left to upper-right), which represents stationary nuclear spins that do not transit between pools during the 200 ms REXSY mixing period and thus maintain a fixed T_2 . Off-diagonal cross peaks, observed between the two short-lived T_2 components, indicate spins that exchange via magnetization transfer mechanisms. Thus, the protons relaxing with $T_2 \approx 60 \mu\text{s}$ and $\approx 400 \mu\text{s}$ are in molecular contact during the mixing period but effectively remain isolated from the long-lived protons.

Resonance and T_2 spectra from a representative cortical bone specimen undergoing prolonged D_2O immersion are shown in Fig 3.4, A and B. Since the D_2O deuteron is undetectable in 1H NMR measurements and may freely exchange with various protons in bone, these spectra demonstrate a combination of 1H signal components that wash out with D_2O (i.e., water and chemically exchangeable protons such as amines and hydroxyls) and those that do not (methylene protons). Of the three resonance spectra components, the dominant

on-resonant narrow-band component was the only component that was nearly completely washed out (> 95 %). The off-resonant narrow-band component was unaffected by D₂O immersion, as was 83 ± 2 % of the broad-band component (17 ± 2 % washed out). Likewise, the only T₂ component effectively removed by D₂O was the ≈ 400 μs T₂. (> 98 % washed out). The ≈ 60 μs T₂ component was unaffected by D₂O immersion (to within the tolerances associated with CPMG data fitting), and 58 ± 12 % of the long-lived T₂ component was removed by D₂O.

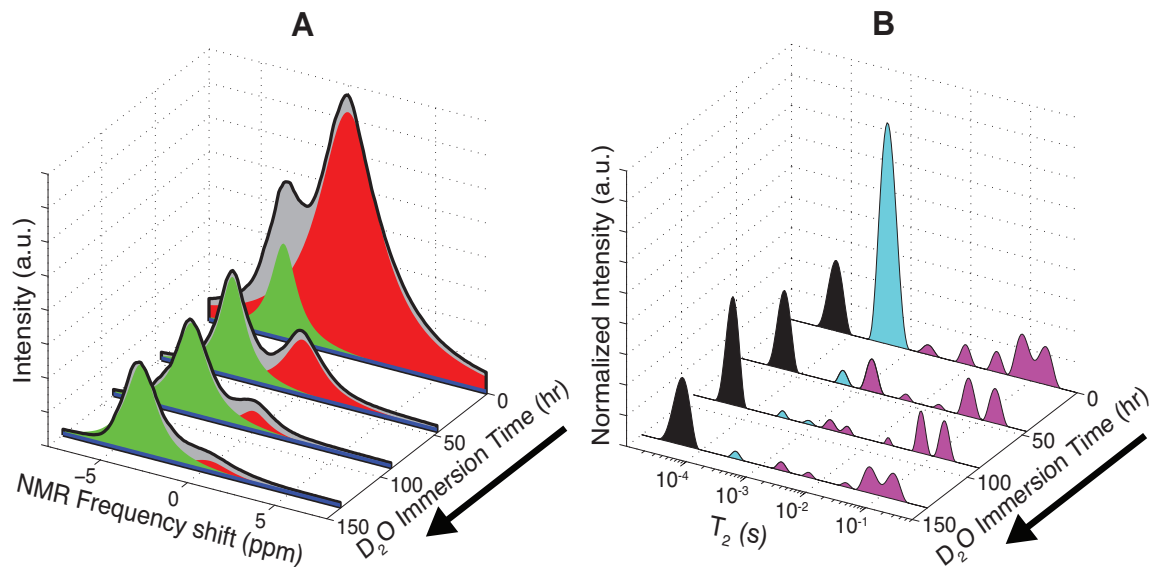


FIGURE 3.4 *Effects of D₂O immersion on resonance and multiexponential T₂ spectra of cortical bone specimens.* Resonance (A) and T₂ spectra (B) are shown at various time points for one representative specimen undergoing D₂O immersion. Resonance spectra, shown in grey and black, were fitted to the sum of three lorentzian components, which are overlaid in red, blue, and green. T₂ spectra are divided into ≈ 60 μs (black), ≈ 400 μs (cyan), and long-lived (magenta) components for comparison to the three resonant components.

3.7 — Discussion: Micro-anatomical Origins of Bone NMR Signals

In animal (24-26) or human (27-31) cortical bones, previous studies have identified various sub-sets of the six NMR components observed herein but have not entirely agreed upon or thoroughly explored their biophysical origins. In particular, the large, sub-millisecond T_2 component has been attributed to both macromolecular-bound water (25,27-31) and porous water of the lacunae and canaliculi (12,26). Because this signal will dominate most standard uTE MRI scans of cortical bone, understanding its biophysical origin and relation to all other signal components is important for interpreting cortical bone MRI. By comparing results from our combination of studies, we have reasoned the biophysical origins of all the FID and CPMG signal components. These assignments and relevant data are summarized in Fig 3.5 and the rationale is outlined as follows.

Based on its chemical shift, endurance through D_2O immersion, and relatively slow relaxation rate, the off-resonant FID component must arise from mobile methylene protons—most likely found on lipids (as similarly concluded by Fernandez-Seara, et. al. (6)). The line width of this component (≈ 1 ppm) corresponds to a $T_2^* \approx 1.6$ ms; therefore, it must be present as a fraction of the long- T_2 component (≈ 45 %) that also survives D_2O immersion.

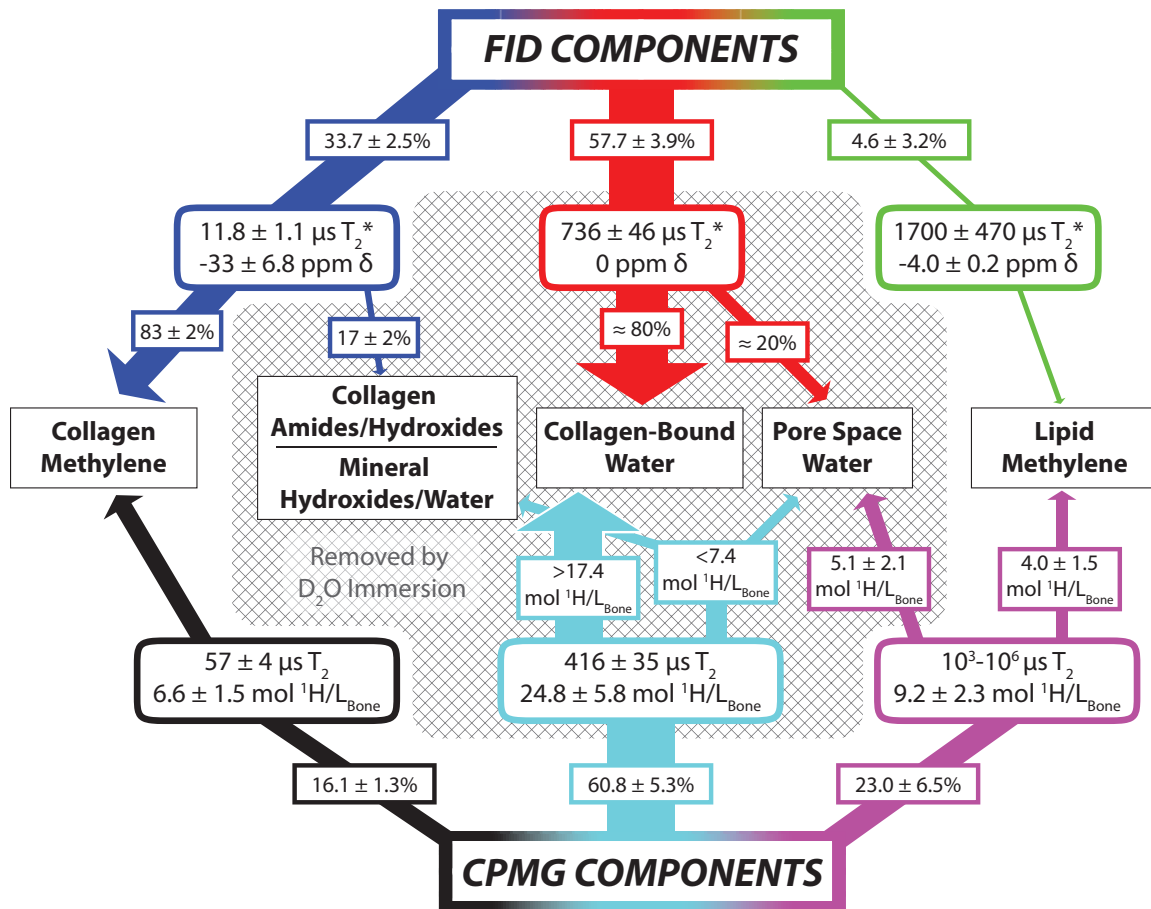


FIGURE 3.5 Postulated biophysical origins of NMR signal relaxation components in human cortical bone. The signal contributions of FID (top) and CPMG (bottom) components to various biophysical proton sources (middle) are indicated by connecting arrows with the same color scheme as in Fig 3.5. FID and CPMG signals are first decomposed into three discrete T_2^* and T_2 relaxation components, respectively, with relevant parameters shown in rounded rectangles. Via D_2O immersion studies and 2-D exchange spectroscopy experiments, these relaxation components can then be assigned to specific proton sources (see Discussion). All components removed by D_2O immersion are enclosed in the shaded area. If a component arises from more than one proton source, the pendant arrows transect approximate signal fractions (%) or proton concentrations ($\text{mol } ^1\text{H}/L_{\text{bone}}$) to indicate the component's distribution among sources.

Aside from the lipid signal, most of the remaining signal that survives D_2O immersion—the broadband FID and short-lived CPMG components—must, by nature of their very short T_2/T_2^* signals, be derived from relatively immobile

methylene protons. The vast majority of these protons must belong to collagen macromolecules, which represent > 90 % of the organic mass in cortical bone (15). Note that both the broadband FID and short-lived CPMG components may arise from the same collagen molecules, but they likely do not originate from the same protons due to the $\approx 70\,000\text{ s}^{-1}$ difference in their relaxation rates ($1/T_2^*$ and $1/T_2$), which is too large to be entirely caused by static magnetic field variations and must arise from different molecular dynamics. It is conceivable that the faster-relaxing FID broadband protons occupy methylene sites on the semi-crystalline collagen triple helix backbone while the slower-relaxing $\approx 60\ \mu\text{s}$ T_2 CPMG protons arise from more mobile collagen methylene, such as side chain positions and the amorphous domains between crystalline regions. While previous cortical bone studies have not distinguished these two signal components, a study of dentin—a bone-like material—found two FID components with $T_2^* \approx 12$ and $60\ \mu\text{s}$ (32).

In contrast to the signal that survives D_2O , the signal that washes out during D_2O immersion must be a combination of water and non-water exchangeable protons (NWEPs, i.e. exchangeable protons that are not found on water). NWEPs in cortical bone arise chiefly from amides/hydroxides in collagen and hydroxides in bone minerals, and NWEP abundance can be estimated as

follows: assuming that bone collagen, on average, can be represented by the well-studied model sequences poly(Gly-Pro-Pro) (33) and poly(Pro-Hyp-Gly) (34), only 6-12% of collagen protons are exchangeable with D₂O, representing 0.4-0.75% of total collagen mass. Given that one mL of cortical bone contains an average of 0.48g organic content (35)—greater than 90% of which is collagen (15)—the expected concentration of exchangeable collagen protons in bone is on the order of 1.7-3.2 mol ¹H/L_{bone}. A similar analysis of bone mineral, using 1.2g mineral/mL bone (35) and a 0.042% weight fraction of exchangeable hydroxide protons (formulated from (36)), gives an expected concentration of 0.5 mol ¹H/L_{bone}. Thus, collagen and mineral sources together give a total NWEF abundance of approximately 2-4 mol ¹H/L_{bone}. Since NWEFs originate from rather immobile proton sites and are expected to be fast relaxing, it is likely that the fraction of the broadband FID component removed by D₂O (≈ 6 % of the total FID signal) accounts for the entire NWEF population. However, it is possible that some of the NWEFs may contribute to the longer-lived FID and CPMG spectral components, but given that an average of 29.5 ± 7.2 mol ¹H/L_{bone} signal was removed from CPMG spectra, we can conclude that this longer-lived signal is predominantly water. Unlike NWEFs, the so-called crystal water protons—ultra-fast-relaxing water in cortical bone mineral crystal lattice vacancies (37)—must be

confined to the small fraction of the broadband FID component removed by D₂O, although the relative contributions of NWEPS and crystal water to this broadband fraction cannot be determined from the measurements herein. With this interpretation, the range of water volume fractions (assuming 1 g/ml water density) found in our 6 specimens was 17.3 - 35.6 %, which is similar to that found from a cohort of pre- and post-menopausal volunteers and renal osteodystrophy patients (12).

The water signal can be further decomposed into two sub-populations: collagen-bound water (again, collagen being the predominant macromolecule) and relatively free water in porous spaces. Based on μ CT at 6 μ m isotropic resolution, Haversian canal porosity of the specimens in this study was 4.0 ± 1.0 %, and we estimate a similar volume of lacunar-canalicular pores (14), making the total average pore volume of the samples ≈ 8 %, or ≈ 9 mol ¹H/L_{bone}. We expect the pore water to have a longer T₂ than the bound water, and $\approx 1/2$ of estimated pore water volume can be accounted for by the 5.1 ± 2.2 mol ¹H/L_{bone} that washed out of the long-T₂ component. The remaining pore water may be included in the ≈ 400 μ s T₂ CPMG component (accounting for no more than ≈ 15 % of it) and/or some of this water may have been wicked inadvertently from the larger pores during sample handling. Thus, including possible contributions of

both NWEPs and porous water, the remainder of the $\approx 400 \mu\text{s}$ T_2 CPMG component must be *at least* $\approx 70\%$ collagen-bound water (or $17.4 - 24.8 \text{ mol } ^1\text{H}/L_{\text{bone}}$). This assignment is roughly consistent with literature estimates of 0.48 g collagen per mL of cortical bone (35) and 0.49 g water bound per gram collagen in bone, which together equate to an expected bound-water proton concentration of $\approx 26 \text{ mol } ^1\text{H}/L_{\text{bone}}$.

The assignments of the $\approx 60 \mu\text{s}$ and $\approx 400 \mu\text{s}$ components to collagen methylene protons and collagen-bound water, respectively, are also consistent with the observation of exchange between these components seen in our RESXY measurements (Fig 3.3). Interestingly, the observation that REXSY demonstrates exchange between these two components but only the $\approx 400 \mu\text{s}$ T_2 component is removed by D_2O indicates that the observed magnetization exchange is mediated by a through-space, dipole-dipole interaction rather than chemical exchange, which further supports our biophysical assignments. It also is noteworthy that our biophysical assignments in human cortical bone are similar to previous findings in human dentin (32) (determined through ^1H NMR relaxometry and sample dehydration), with one particular exception: the $\approx 60 \mu\text{s}$ decay component in dentin was attributed to a mixture of hydroxide and water, in addition to protein. At least one other study has identified very-short lived water

in bone mineral (37); however, it disappeared with dehydration and so we presume it would be washed out with D₂O. Herein, we conclude that the 60- μ s T₂ component is predominantly protein-derived because it survives D₂O immersion.

Finally, it should be noted that the broad age range of the bone donors herein allowed the study of common relaxation features across presumably diverse physiological states. Interestingly, relaxation rates among all the donors were similar, indicating that the chemical nature of various bone proton milieux persist during aging. The dominant source of variability observed among donors was in the relaxation component pool sizes; for example, the oldest and most visibly osteoporotic donor had a larger long-lived T₂ component (Fig 3.1c, turquoise line) than the other donors. However, a thorough analysis of the inter-donor relaxation differences would require a significantly larger number of donors, which is beyond the scope of this work but is the subject of future study.

3.8 – *Conclusions*

In summary, ¹H NMR signal from human cortical bone was found to exhibit a broad distribution of transverse relaxation components attributable to known bone proton sources (Fig 3.5) as follows: i) T₂^{*} \approx 12 μ s, derived \approx 80 % from collagen backbone methylene protons and the remainder from non-water

exchangeable protons (amide/hydroxide) and possibly adsorbed mineral water, ii) $T_2 \approx 60 \mu\text{s}$, derived predominantly from collagen side-chain or otherwise mobile methylene protons, iii) $T_2 \approx 400 \mu\text{s}$, derived predominantly from water bound to the collagen responsible for the $12 \mu\text{s } T_2^*$ and $60 \mu\text{s } T_2$ components, iv) $T_2 \approx$ milliseconds-second, derived $\approx 60 \%$ from pore water and $\approx 40 \%$ from lipid methylene protons. These findings indicate that modern uTE MRI of cortical bone is dominated by signal from water bound to bone matrix collagen, and that commonly-used long- T_2 suppression techniques for enhancing bone contrast will suppress signal from lipids and pore space water that may be of biological/clinical interest. Also, while some short- T_2 signals in bone may be difficult to quantify directly, the interaction between their underlying proton pool and the dominant water signal offers the potential to probe prohibitively fast-relaxing cortical bone signals through magnetization transfer contrast. Finally, there was considerable variability in the lipid and pore water content across the diverse (albeit small number of) human cortical bone samples studied herein, indicating these two metrics may contain the useful information on bone quality and health.

3.9 – References

1. Johnell O, Kanis JA, Oden A, Johansson H, De Laet C, Delmas P, Eisman JA, Fujiwara S, Kroger H, Mellstrom D, Meunier PJ, Melton LJ, O'Neill T, Pols H, Reeve J, Silman A, Tenenhouse A. Predictive value of BMD for hip and other fractures. *J Bone Miner Res* 2005;20(7):1185-1194.
2. Bembey AK, Bushby AJ, Boyde A, Ferguson VL, Oyen ML. Hydration effects on the micro-mechanical properties of bone. *J Mater Res* 2006;21(8):1962-1968.
3. Nyman JS, Roy A, Shen XM, Acuna RL, Tyler JH, Wang XD. The influence of water removal on the strength and toughness of cortical bone. *J Biomech* 2006;39(5):931-938.
4. Yan JH, Daga A, Kumar R, Mecholsky JJ. Fracture toughness and work of fracture of hydrated, dehydrated, and ashed bovine bone. *J Biomech* 2008;41(9):1929-1936.
5. Sasaki N, Enyo A. Viscoelastic properties of bone as a function of water-content. *J Biomech* 1995;28(7):809-815.
6. Fernandez-Seara MA, Wehrli SL, Takahashi M, Wehrli FW. Water content measured by proton-deuteron exchange NMR predicts bone mineral density and mechanical properties. *J Bone Miner Res* 2004;19(2):289-296.
7. Bembey AK, Oyen ML, Bushby AJ, Boyde A. Viscoelastic properties of bone as a function of hydration state determined by nanoindentation. *Philos Mag* 2006;86(33-35):5691-5703.
8. Nyman JS, Ni QW, Nicolella DP, Wang XD. Measurements of mobile and bound water by nuclear magnetic resonance correlate with mechanical properties of bone. *Bone* 2008;42(1):193-199.
9. Balcom BJ, MacGregor RP, Beyea SD, Green DP, Armstrong RL, Bremner TW. Single-point ramped imaging with T-1 enhancement (SPRITE). *J Magn Reson Ser A* 1996;123(1):131-134.
10. Idiyatullin D, Corum C, Park JY, Garwood M. Fast and quiet MRI using a swept radiofrequency. *J Magn Reson* 2006;181(2):342-349.
11. Gatehouse PD, Bydder GM. Magnetic resonance imaging of short T-2 components in tissue. *Clin Radiol* 2003;58(1):1-19.
12. Techawiboonwong A, Song HK, Leonard MB, Wehrli FW. Cortical bone water: In vivo quantification with ultrashort echo-time MR imaging. *Radiology* 2008;248(3):824-833.

13. Olszta MJ, Cheng XG, Jee SS, Kumar R, Kim YY, Kaufman MJ, Douglas EP, Gower LB. Bone structure and formation: A new perspective. *Mater Sci Eng R* 2007;58(3-5):77-116.
14. Cowin SC. Bone poroelasticity. *J Biomech* 1999;32(3):217-238.
15. Weiner S, Wagner HD. The material bone: Structure mechanical function relations. *Annu Rev Mater Sci* 1998;28:271-298.
16. Meiboom S, Gill D. Modified Spin-Echo Method for Measuring Nuclear Relaxation Times. *Rev Sci Instrum* 1958;29(8):688-691.
17. Callaghan PT, Arns CH, Galvosas P, Hunter MW, Qiao Y, Washburn KE. Recent Fourier and Laplace perspectives for multidimensional NMR in porous media. *Magnetic Resonance Imaging* 2007;25(4):441-444.
18. English AE, Whittall KP, Joy MLG, Henkelman RM. Quantitative 2-dimensional time correlation relaxometry. *MagnResonMed* 1991;22(2):425-434.
19. Dortch RD, Horch RA, Does MD. Development, simulation, and validation of NMR relaxation-based exchange measurements. *Journal of Chemical Physics* 2009;131(16):11.
20. Whittall KP, Mackay AL. Quantitative interpretation of NMR relaxation data. *J Magn Reson* 1989;84(1):134-152.
21. Venkataramanan L, Song YQ, Hurlimann MD. Solving Fredholm integrals of the first kind with tensor product structure in 2 and 2.5 dimensions. *IEEE Trans Signal Process* 2002;50(5):1017-1026.
22. Edzes HT, Samulski ET. Measurement of cross-relaxation effects in proton NMR spin-lattice relaxation of water in biological-systems - hydrated collagen and muscle. *J Magn Reson* 1978;31(2):207-229.
23. Macura S, Huang Y, Suter D, Ernst RR. Two-dimensional chemical-exchange and cross-relaxation spectroscopy of coupled nuclear spins. *J Magn Reson* 1981;43(2): 259-281.
24. Turov VV, Gun'ko VM, Zarko VI, Leboda R, Jablonski M, Gorzelak M, Jagiello-Wojtowicz E. Weakly and strongly associated nonfreezable water bound in bones. *Colloids Surf B* 2006;48(2):167-175.
25. Fantazzini P, Brown RJS, Borgia GC. Bone tissue and porous media: common features and differences studied by NMR relaxation. *Magn Reson Imaging* 2003;21(3-4):227-234.

26. Ong HH, Wehrli SL, Wehrli FW. Proton NMR Study of Transverse Relaxation in Rabbit and Rat Cortical Bone. *J Bone Miner Res* 2008;23:S494-S494.
27. Ni QW, King JD, Wang XD. The characterization of human compact bone structure changes by low-field nuclear magnetic resonance. *Meas Sci Technol* 2004;15(1):58-66.
28. Wang XD, Ni QW. Determination of cortical bone porosity and pore size distribution using a low field pulsed NMR approach. *J Orthop Res* 2003;21(2):312-319.
29. Ni QW, Santos ADL, Lam H, Qin YX. Assessment of simulated and functional disuse on cortical bone by nuclear magnetic resonance. *Adv Space Res* 2007;40(11):1703-1710.
30. Ni QW, Nicoletta DP. The characterization of human cortical bone microdamage by nuclear magnetic resonance. *Meas Sci Technol* 2005;16(3):659-668.
31. Ni QW, Nyman JS, Wang XD, De Los Santos A, Nicoletta DP. Assessment of water distribution changes in human cortical bone by nuclear magnetic resonance. *Meas Sci Technol* 2007;18(3):715-723.
32. Schreiner LJ, Cameron IG, Funduk N, Miljkovic L, Pintar MM, Kydon DN. Proton NMR spin grouping and exchange in dentin. *Biophys J* 1991;59(3):629-639.
33. Boryskina OP, Bolbukh TV, Semenov MA, Gasan AI, Maleev VY. Energies of peptide-peptide and peptide-water hydrogen bonds in collagen: Evidences from infrared spectroscopy, quartz piezogravimetry and differential scanning calorimetry. *J Mol Struct* 2007;827(1-3):1-10.
34. Berisio R, Vitagliano L, Mazzarella L, Zagari A. Crystal structure of a collagen-like polypeptide with repeating sequence Pro-Hyp-Gly at 1.4 angstrom resolution: Implications for collagen hydration. *Biopolymers* 2000;56(1):8-13.
35. Gong JK, Arnold JS, Cohn SH. Composition of Trabecular and Cortical Bone. *Anat Rec* 1964;149:325-331.
36. Cho G, Wu Y, Ackerman JL. Detection of hydroxyl ions in bone mineral by solid-state NMR spectroscopy. *Science* 2003;300(5622):1123-1127.
37. Wilson EE, Awonusi A, Morris MD, Kohn DH, Tecklenburg MMJ, Beck LW. Three structural roles for water in bone observed by solid-state NMR. *Biophys J* 2006;90(10):3722-3731.

CHAPTER 4

Biomechanical Significance of the Cortical Bone T_2 Distribution

The previous chapter established the micro-anatomical origins of NMR signals in human cortical bones, providing a framework for analyzing NMR data in the context of bone physiology. In this chapter, the biomechanical significance of this framework is evaluated by examining the correlations between human cortical bone ^1H NMR or high-resolution X-ray signals and various measured mechanical properties. Results showed that ^1H NMR signals were better predictors of yield stress, peak stress, and pre-yield toughness than were the X-ray derived signals. These ^1H NMR signals can, in principle, be extracted from clinical MRI, thus offering the potential for improved clinical assessment of fracture risk.

4.1 — Background and Introduction: The Material Role of Bone NMR

Current clinical bone diagnostics are incomplete. Recalling from Chapter 1.3, the estimate of areal bone mineral density (BMD) by dual energy x-ray absorptiometry (DXA) does not fully predict fracture risk: for a given DXA score, there is an unexplained increase in fracture risk with age (1,2), as well as with progression of various disease states, such as diabetes (3). The limitations of

DXA related to BMD depending on bone size (4) may be somewhat overcome by quantitative computed tomography imaging, but, ultimately, any X-ray based diagnostic is only sensitive to the mineral portion of the bone, which accounts for only $\approx 43\%$ of bone by volume. The remaining soft-tissue components of bone, including collagen and collagen-bound water, are essentially invisible to DXA and quantitative computed tomography. In contrast, clinical MRI, which is based on the ^1H NMR signal, cannot directly detect bone mineral but is sensitive to the soft tissue of bone. Further, a recent study has demonstrated that ^1H NMR transverse relaxation time constants (T_2) distinguishes proton signals from collagen, collagen-bound water, and pore water (5). With this technology and the idea that the presence and hydration-state of collagen play a critical role in dissipating energy in bone (6), we hypothesized that ^1H NMR can report on the material strength of bone, and we present here compelling experimental observations from ^1H NMR, X-ray CT and mechanical analyses of cadaveric bone samples which indicate that MRI has the potential to diagnose fracture risk better than DXA.

4.2 — Experimental Methods: Human cortical bone processing

The Musculoskeletal Tissue Foundation (Edison, NJ), a non-profit tissue allograft bank, and the Vanderbilt Donor Program (Nashville, TN) supplied human femurs from 40 cadaveric donors (26 male, 14 female, aged 21-105 years old, mean \pm standard deviation: 67 ± 24 years) under instruction to not provide tissue from donors who had tested positive for a blood borne pathogen (e.g., HIV or Hepatitis C). One human cortical bone sample per donor was extracted from the medial quadrant of the mid-shaft and was machined to $70 \times 5 \times 2$ mm³ dimensions via end mill. During dimensioning, care was taken to remove endosteal and periosteal surfaces such that the final specimens were pure cortical bone. From each milled sample, three specimens were extracted for NMR, μ CT, and mechanical testing (Fig 4.1).

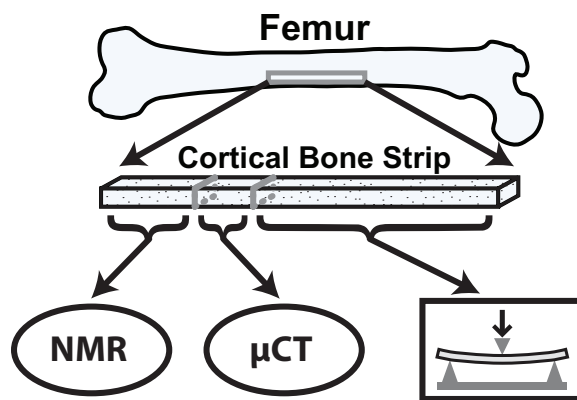


FIGURE 4.1 *NMR/ μ CT/mechanical testing study overview.* From each cadaveric bone studied, one strip of cortical bone was extracted, three separate pieces of which were used for NMR, μ CT, and mechanical testing.

Specimens were stored in phosphate-buffered saline at -20°C then thawed at 4°C for approximately 18 hours prior to NMR measurements. (No more than three freeze-thaw cycles were involved for a given specimen, and separate experiments found that up to six freeze-thaw cycles had negligible impact on the NMR properties.) Final specimen dimensions were measured with digital caliper for volume determination. Further details of bone tissue processing are given in Appendix II.

4.3 — *Experimental Methods: NMR*

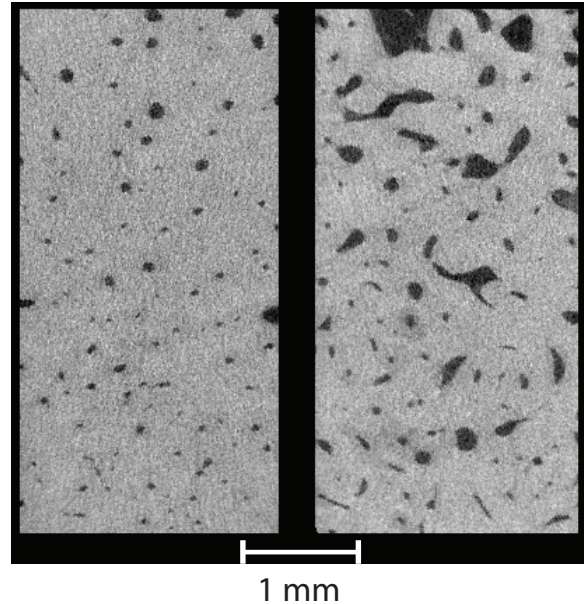
From one of the three specimens per donor sample, ^1H NMR transverse relaxation (T_2) characteristics were measured and reduced to three independent signal components, which we have recently identified as being primarily derived from collagen methylene protons, collagen-bound water protons, and water protons in pores (5). All NMR measurements were performed in a Varian/Magnex 4.7 T horizontal bore magnet with a Direct Drive Receiver. An in-house loop-gap style RF coil with Teflon structural support was used (similar to the coil described in (18) and the lowest- ^1H design in Chapter 2), which provided $90^{\circ}/180^{\circ}$ RF pulses of $\approx 8\mu\text{s}/16\mu\text{s}$ duration and contributed negligible background ^1H signal ($\approx 1\%$ of net bone signal).

Carr-Purcell-Meiboom-Gill (CPMG) measurements with a total of 10000 echoes were collected at 100 μs echo spacing, which was empirically determined to be a suitable minimum threshold for both maximizing the range of T_2 detection while minimizing spin-locking effects. Echo magnitudes were fitted to a sum of 128 decaying exponential functions (with time constants log-spaced between 20 μs and 10 sec) in a non-negative least-squares sense, subject to a minimum curvature constraint, which produced a so-called T_2 spectrum (19). In order to quantitatively compare the absolute signal amplitudes of T_2 components across days, a reference sample with long T_2 ($\approx 2\text{s}$) and known proton content was included in each CPMG measurement. The presence of the reference sample, together with the known specimen volumes, enabled the calculation of proton concentrations in the bulk bone specimens for each CPMG relaxation component by comparing integrated areas of each T_2 spectral component to the area of the marker. As a simple demonstration of the potential for acquiring signal from a specific T_2 domain without the full CPMG acquisition, from one bone specimen, an additional CPMG measurement was acquired with a preceding a 10-ms duration, 3500 Hz bandwidth hyperbolic secant inversion pulse (20), so chosen to selectively invert the long- T_2 ^1H signal.

4.4 — *Experimental Methods: μ CT*

The second specimen from each donor sample (~ volume of 40 mm³) was studied at high resolution (6 μ m), with low noise μ CT to quantify apparent volumetric bone mineral density (avBMD) and intracortical porosity (for pores \geq 6 μ m in diameter). Note that for a given specimen size avBMD is a volumetric analog to areal BMD as measured by DXA, and intracortical porosity at this resolution is not readily determined from clinical radiographs or QCT including high-resolution peripheral QCT scanners (which obtain resolutions of 80-100 μ m) (21). The specimen was scanned by acquiring 1000 projections per 180° at 70 keV using a Scanco, model μ CT-40. From an hydroxyapatite (HA) phantom image (acquired weekly), linear attenuation coefficients derived from the μ CT images were equated to volumetric bone mineral density (vBMD) in units of mg-HA/cm³. Using the Scanco software, the outer perimeter of the sample was defined to determine the total bone volume. The avBMD was defined as the mean of vBMD for all voxels within the total bone volume. The bone tissue volume was segmented from air or soft tissue at a threshold of 800 mg-HA/cm³ to determine the porosity (= 1 minus bone tissue volume per total bone volume) (Fig 4.2).

FIGURE 4.2 *Representative μ CT.* Axial μ CT images are shown for cortical bone specimens from a 48 y.o. male donor (left) and an 82 y.o. male donor (right). For the 48 and 82 y.o. donors, respectively, avBMD was 1222 and 1135 mg-HA/cm³, and porosity was 4 % and 11.3 %.



4.5 — *Experimental Methods: Mechanical Testing*

Finally, we subjected the third, parallelepiped specimen (nominal dimensions of 2 mm x 5 mm x 40 mm) from each donor sample to a three point bending test, and measured four mechanical properties relevant to fracture risk in bone: yield stress, peak stress, flexural modulus, and pre-yield or elastic toughness. A material testing system (Dynamight 8841, Instron, Canton, OH) recorded the force-displacement data (Fig 4.3) from a 100 N load cell and the linear variable differential transformer, respectively, at 50 Hz, as the hydrated bone was loaded to failure at 5 mm/min. The span was 35 mm, and all tests were performed at room temperature. Applying the flexure formula to the yield force, as determined by the 0.2% offset, or to the peak force endured by the bone specimen, and applying the deflection equation to the slope of the linear section

of the force-displacement curve provided the material properties, yield stress, peak stress, and flexural modulus, respectively (6). Pre-yield or elastic toughness was the area under the force-displacement curve from zero displacement to the yield displacement divided by the cross-sectional area of the bone sample to account for slight differences in specimen dimensions.

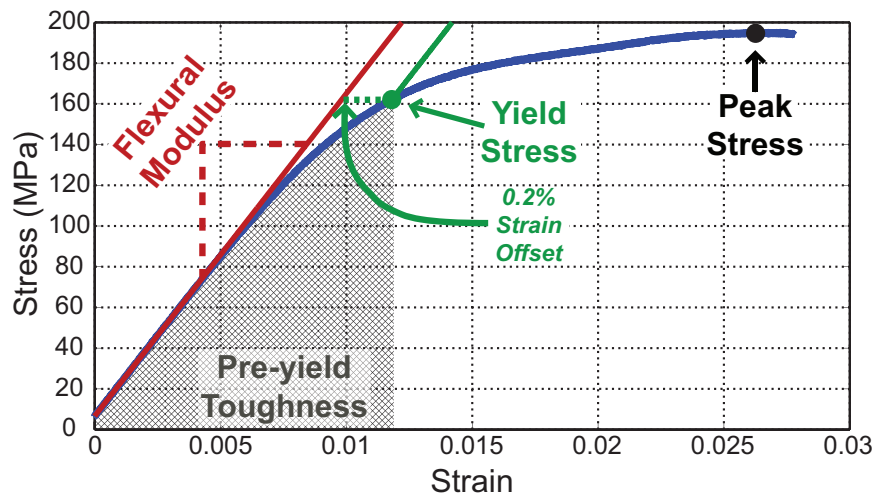


FIGURE 4.3 *Mechanical testing analysis.* A representative stress vs. strain curve for cortical bone is shown (blue) along with graphical depictions of mechanical parameters. Flexural modulus is the slope of the initial linear mechanical response, yield stress is defined at 0.2% offset from the flexural modulus line, and peak stress is the maximum observed stress. Pre-yield toughness (see text for definition) is proportional to the area under the curve, up to the yield stress.

4.6 — Experimental Findings: Correlates to Mechanical Properties

Figure 4.4 shows the mean (and standard deviation and range) spectrum of ^1H NMR transverse relaxation time constants (T_2 spectrum) from 40 cadaveric bone

samples. In this mean spectrum and in each individual sample spectrum, signal from three distinct domains of T_2 were readily identified, as previously found (5): $50 \mu\text{s} < T_2 < 150 \mu\text{s}$, defined as pool A, due primarily to collagen methylene protons; $150 \mu\text{s} < T_2 < 1 \text{ ms}$, pool B, due primarily to collagen-bound water protons; and $1 \text{ ms} < T_2 < 1 \text{ s}$, pool C, due to water protons in pores in lipid protons. From these three signals, six parameters were extracted: 3 signal amplitudes (S_A, S_B, S_C , in absolute units of mole ^1H per liter bone) and 3 corresponding mean relaxation rate constants ($R_{2,A}, R_{2,B}, R_{2,C}$ in s^{-1}). Note that while the signal amplitudes are computed in absolute units of concentration, the correspondence between signal amplitudes, S_A, S_B , and S_C , and actual concentrations of collagen methylene protons, bound water protons, and pore-water or lipid protons, respectively, is potentially affected by a number of factors, including the line shape of the methylene protons, the magnetization exchange rate between bound and methylene protons, and overlap of T_2 components from different sources.

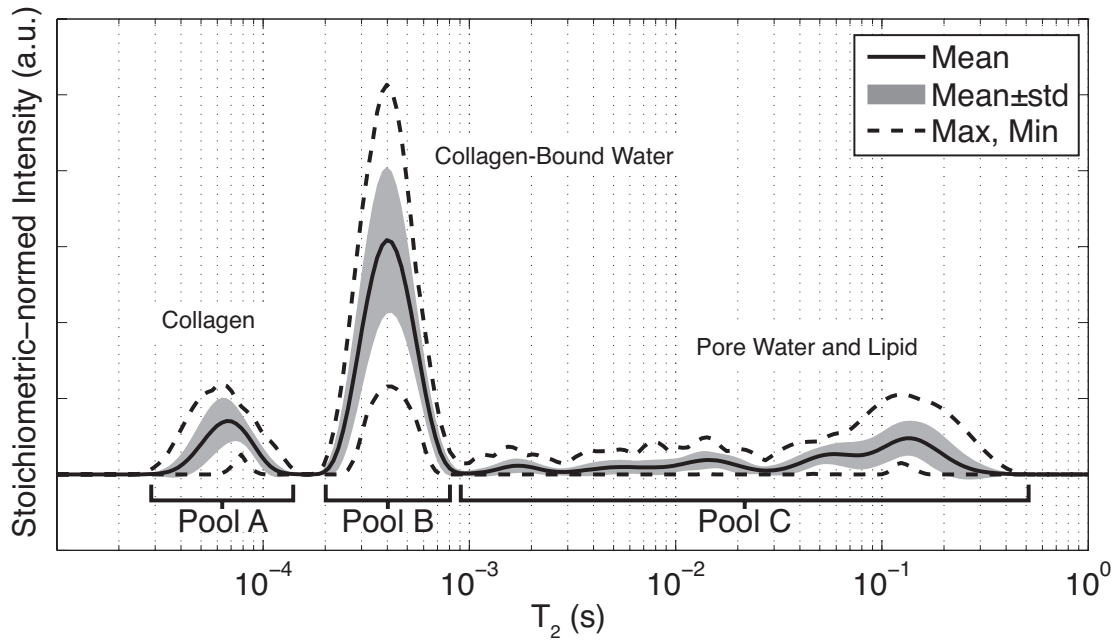


FIGURE 4.4 Summary of T_2 spectra measured from 40 human cortical bone samples. All spectra exhibited a short- T_2 component ($T_2 \approx 60 \mu\text{s}$), derived primarily from collagen protons, an intermediate T_2 components ($T_2 \approx 400 \mu\text{s}$), derived primarily from collagen-bound water protons, and a broad distribution of long- T_2 components ($1 \text{ ms} < T_2 < 1 \text{ s}$), derived from a combination of pore water and lipid protons.

Each of the three NMR signal amplitudes (S_A , S_B , S_C) was found to linearly correlate ($r^2 = 0.34, 0.68, 0.61, p < 0.05$) with peak stress (Fig 4.5), but note that the sum of all three signals did not ($r^2 = 0.06, p > 0.05$). Similar pair-wise linear correlations (and lack thereof) also existed between NMR signal amplitudes and the other three measured mechanical properties.

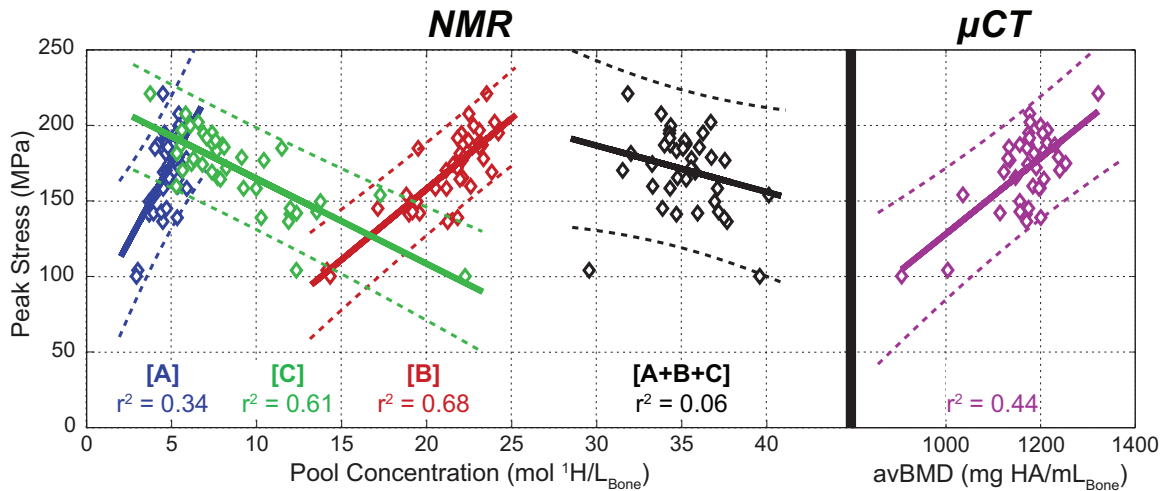


FIGURE 4.5 Correlations of measured peak stress and T_2 spectral component amplitudes (NMR, left) and avBMD measured by μ CT (right). Blue, red, and green data show integrated amplitudes (S_A , S_B , and S_C) of the T_2 -discriminated signals from pools A, B, and C, respectively. The black data show the total ^1H NMR signal ($S_A + S_B + S_C$), and the purple data are derived from μ CT-based measures of avBMD. Each of the NMR signals amplitudes shows a significant linear correlation with peak stress and both S_B and S_C correlate more strongly with peak stress than does avBMD. Note that the total ^1H NMR signal does not correlate well with peak stress.

These findings indicate that peak cortical bone stress, and the other measured mechanical properties, are directly related to the amount of collagen and collagen-bound water in bone, and inversely related to the bone pore volume. μ CT-derived measures of bone porosity and avBMD (akin to DXA) were also found to linearly correlate with mechanical properties, but S_A and S_B were better predictors (i.e., higher r^2 values) than μ CT-porosity for three of four mechanical properties (flexural modulus being the exception), and better predictors than avBMD (i.e., DXA) for all four mechanical properties. Table 4.1

summarizes the pairwise linear correlations between imaging measure (^1H NMR and X-ray) and the four mechanical properties.

	Yield Stress	Fracture Stress	Flexural Modulus	Pre-yield Toughness
R_2A	0.10	0.12	0.04	0.12
R_2B	0.19	0.22	0.12	0.19
R_2C	0.00	0.01	0.01	0.00
[A]	0.41	0.34	0.39	0.34
[B]	0.62	0.68	0.48	0.57
[C]	0.57	0.61	0.49	0.49
[A+B+C]	0.05	0.06	0.06	0.03
aBMD	0.43	0.44	0.46	0.33
Porosity	0.58	0.60	0.59	0.46

$p > 0.05$
 $r^2 \leq 0.3$
 $0.3 < r^2 \leq 0.6$
 $0.6 < r^2$

TABLE 4.1 Summary of Pearson's r^2 for pairwise correlations between imaging measures (^1H NMR and X-ray) and mechanical properties. All correlations were significant ($p < 0.05$) except those shaded grey. Red, yellow and blue shading indicate ranges of r^2 values, and the imaging measure that was most predictive (highest r^2) of each mechanical measure is highlighted with a bold outline.

Note that without the two apparent outlier data (peak stress ≈ 100 MPa), the predictive power of S_B and S_C decreased to r^2 values of 0.52 and 0.49, respectively, but the r^2 of avBMD with peak stress decreased to a greater extent (to 0.16). That is, the relative predictive power of S_B and S_C compared with avBMD *increased* without these two data points. Also note that multiple linear regression analysis told a similar story: combination of NMR signal parameters

(R_B and S_B) best predicted of three of four mechanical properties (adjusted R^2 : 0.56-0.70, again, flexural modulus was the exception), and better predicted all four mechanical properties than did avBMD.

4.7 — Discussion: Potential for MRI-based Fracture Risk Assessment

As a surrogate to radiation-based CT, MRI has been developed to characterize trabecular volume and architecture as a means to assess fracture risk (7,8). For example, such MRI-derived measurements of bone volume fraction and trabecular thickness correlated with the compressive strength of human trabecular bone, although the correlations were not as strong as that between CT-derived BMD and compressive strength (9). These MRI techniques do not assess the inherent quality of the bone tissue, and this is a significant shortcoming given the importance of ultrastructural characteristics of the extracellular matrix (e.g., collagen integrity) to the fracture resistance of bone (10). From ex vivo studies of bone, various quantifications of water by NMR have been correlated with the mechanical competence of bone. In a rabbit model of diet-induced hypomineralization, a ^1H NMR-derived measurement of water content was directly related to the bending strength of cortical bone (11); however, in a study of ovariectomized and treated mice, only group-mean total water ^1H NMR signal correlated with mechanical properties—no correlation was found across pooled

data from 60 bones, which may be explained by the findings of total ^1H signal shown here (Fig 4.5). Also, an NMR technique known as “decay from diffusion in an internal field” (DDIF) found an inverse correlation between this NMR-derived pore water parameter and the yield stress of bovine trabecular bone in compression (12), in rough agreement with the present observations of pore-water. Prior to the present study though, only one study attempted to correlate NMR measurements of both pore water and water bound to the extracellular matrix to the mechanical properties of human bone (13). That study used T_2^* -discriminated rather than T_2 -discriminated (used herein) ^1H NMR signals at low static magnetic field, and while a direct relationship existed between the so-called T_2^* -defined bound water and peak stress, it described a much lower fraction of the peak stress variance ($r^2 = 0.36$, compared to 0.68, above). Also, the translation of T_2^* based discrimination to clinical imaging may be problematic due to the presence of lipid in bone (5,11), and the inability of T_2^* to discriminate bone ^1H pools at clinical field strengths (no discrimination was found at 4.7T (5) and no discrimination has been reported at clinical fields strengths (≥ 1.5 T)).

Current uTE protocols on human MRI systems use echo times $< 100 \mu\text{s}$ ((14) and references therein), more than short enough to capture the majority of the bound water signal and some of the collagen proton signal, but the

translation of the present findings to clinical MRI will require practical imaging methods of distinguishing these short- T_2 signals from the longer- T_2 pore water and lipid signals. There are numerous strategies for integrating T_2 -selective magnetization preparation into a clinically practical uTE-type sequence (15,16,17), and the optimal approach for bone imaging has not yet been determined. However, Fig 4.6 shows two T_2 spectra from one bone specimen. The solid line shows the normal T_2 spectrum, as used in the above analysis, while the dotted line shows the spectrum that results following the complex average of two CPMG signals, with and without the preceding hyperbolic secant RF pulse. This RF pulse effectively inverts only the long T_2 signals while largely saturating the collagen proton and bound-water signal, so the complex average cancels only the long T_2 signals and results in a net NMR signal that is $\approx 95\%$ derived from protons with $T_2 < 1\text{ms}$. With such an approach, it is conceivable that quantitative MRI methods can be developed which report on bone fracture risk via the NMR/mechanical property relationships in Fig 4.5 & Table 4.1.

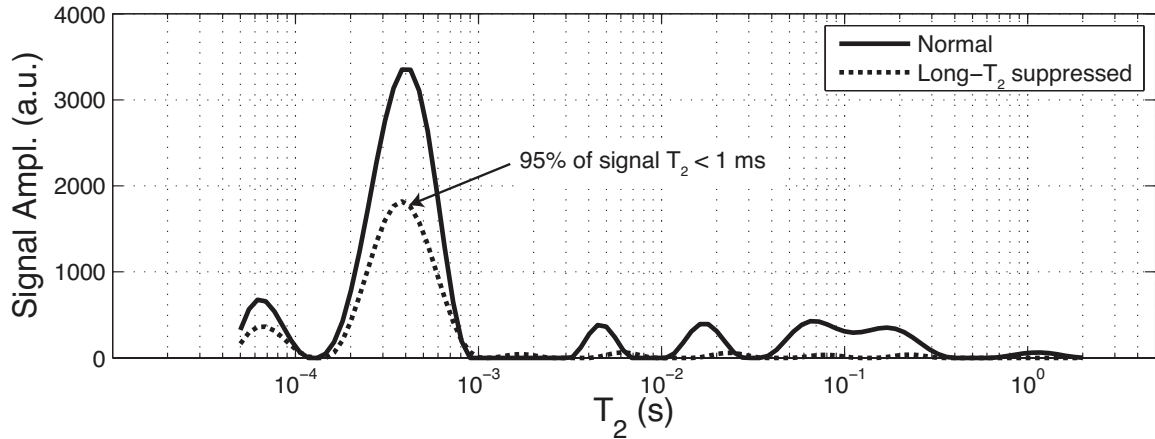


FIGURE 4.6 *Adiabatic T_2 -selective suppression.* Solid line shows a the T_2 spectrum from a typical bone sample, and the dotted line shows the spectrum that results following the complex average of two signals, with and without an adiabatic full passage magnetization preparation. The total integrated signal from this long- T_2 suppressed spectrum is 95% from signals with $T_2 < 1$ ms, thereby demonstrating in principle a simple and practical method for generating a MRI contrast dominated by $S_A + S_B$.

4.8 — Conclusions

These results demonstrate in principle that a simple RF pre-pulse, which can be readily integrated into a standard uTE pulse sequence, can distinguish pore water from collagen protons and collagen bound water protons in bone. Once implemented on clinical scanners, such an MRI method can then assess both the contribution of structure to whole bone strength as well as the contributions of collagen integrity and porosity. Since individual NMR measures of collagen and bound/pore water content were found to have a higher correlation to bone biomechanics than X-rays, MRI-based contrast has the potential to provide a

more complete assessment of fracture risk than current X-ray based methods as long as bound/pore water and/or collagen constituents are discriminated.

4.9 – References

1. Kanis JA, Johnell O, Oden A, Dawson A, De Laet C, et al. (2001) Ten year probabilities of osteoporotic fractures according to BMD and diagnostic thresholds. *Osteoporos Int* 12: 989-995.
2. Johnell O, Kanis JA, Oden A, Johansson H, De Laet C, et al. (2005) Predictive value of BMD for hip and other fractures. *J Bone Miner Res* 20: 1185-1194.
3. Vestergaard P (2007) Discrepancies in bone mineral density and fracture risk in patients with type 1 and type 2 diabetes--a meta-analysis. *Osteoporos Int* 18: 427-444.
4. Carter DR, Bouxsein ML, Marcus R (1992) New approaches for interpreting projected bone densitometry data. *J Bone Miner Res* 7: 137-145.
5. Horch RA, Nyman JS, Gochberg DF, Dortch RD, Does MD (2010) Characterization of ¹H NMR Signal in Human Cortical Bone for Magnetic Resonance Imaging. *Magnetic Resonance in Medicine* 64: 680-687.
6. Nyman JS, Roy A, Shen XM, Acuna RL, Tyler JH, et al. (2006) The influence of water removal on the strength and toughness of cortical bone. *Journal of Biomechanics* 39: 931-938.
7. Wehrli FW (2007) Structural and functional assessment of trabecular and cortical bone by micro magnetic resonance imaging. *J Magn Reson Imaging* 25: 390-409.
8. Majumdar S (2008) Magnetic resonance imaging for osteoporosis. *Skeletal Radiol* 37: 95-97.
9. Majumdar S, Kothari M, Augat P, Newitt DC, Link TM, et al. (1998) High-resolution magnetic resonance imaging: three-dimensional trabecular bone architecture and biomechanical properties. *Bone* 22: 445-454.
10. Nyman JS, Reyes M, Wang X (2005) Effect of ultrastructural changes on the toughness of bone. *Micron* 36: 566-582.

11. Fernandez-Seara MA, Wehrli SL, Takahashi M, Wehrli FW (2004) Water content measured by proton-deuteron exchange NMR predicts bone mineral density and mechanical properties. *J Bone Miner Res* 19: 289-296.
12. Sigmund EE, Cho H, Chen P, Byrnes S, Song YQ, et al. (2008) Diffusion-based MR methods for bone structure and evolution. *Magn Reson Med* 59: 28-39.
13. Nyman JS, Ni Q, Nicolella DP, Wang X (2008) Measurements of mobile and bound water by nuclear magnetic resonance correlate with mechanical properties of bone. *Bone* 42: 193-199.
14. Robson MD and Bydder GM (2006) Clinical ultrashort echo time imaging of bone and other connective tissues. *NMR in Biomedicine* 19: 765-780.
15. Larson PEZ, Conolly SM, Pauly JM, Nishimura DG (2007) Using adiabatic inversion pulses for long-T-2 suppression in ultrashort echo time (UTE) imaging. *Magnetic Resonance in Medicine* 58: 952-961.
16. Rahmer J, Blume U, Bornert P (2007) Selective 3D ultrashort TE imaging: comparison of "dual-echo" acquisition and magnetization preparation for improving short-T-2 contrast. *Magnetic Resonance Materials in Physics Biology and Medicine* 20: 83-92.
17. Du J, Takahashi AM, Bae WC, Chung CB, Bydder GM (2010) Dual Inversion Recovery, Ultrashort Echo Time (DIR UTE) Imaging: Creating High Contrast for Short-T-2 Species. *Magnetic Resonance in Medicine* 63: 447-455.
18. Horch RA, Wilkens K, Gochberg DF, Does MD (2010) RF coil considerations for short T2 MRI. *Magnetic Resonance in Medicine* 64: 1652-1657.
19. Whittall KP, Mackay AL (1989) Quantitative interpretation of NMR Relaxation Data. *Journal of Magnetic Resonance* 84: 134-152.
20. Silver MS, Joseph RI, Hoult DI (1984) Highly Selective $\pi/2$ and π -Pulse Generation. *Journal of Magnetic Resonance* 59: 347-351.
21. Burghardt AJ, Kazakia GJ, Ramachandran S, Link TM, Majumdar S (2010) Age- and Gender-Related Differences in the Geometric Properties and Biomechanical Significance of Intracortical Porosity in the Distal Radius and Tibia. *Journal of Bone and Mineral Research* 25: 983-993.

CHAPTER 5

Clinical Methods for Bound/Pore Water-discriminated Imaging of Cortical Bone

Human cortical bone is known to contain a distribution of T_1 and T_2 components attributed to bound and pore water (Chapter 3), and NMR-based quantitation of these components is more biomechanically-informative than X-ray-based measures as long as bound and pore water are distinguished (Chapter 4). Despite the wide array of bone MRI methods (Chapter 1.4), clinical imaging approaches have yet to discriminate bound from pore water on the basis of their relaxation properties. In this chapter, two clinically-compatible MRI methods are proposed for selectively imaging either bound or pore water by utilizing differences in their T_{1s} and T_{2s} . The methods are validated in a population of *ex vivo* human cortical bones, and estimates obtained for bound and pore water are compared to bone mechanical properties. Results show that the two MRI methods provide good estimates of bound and pore water that correlate to bone mechanical properties. As such, the bound and pore water-discriminated MRI protocols shown herein should provide diagnostically useful tools for assessing bone fracture risk.

5.1 — Background and Introduction: The Need for Bound/Pore Water Discrimination

The development of ultrashort-echo time (uTE) and related MRI methods for imaging short T_2 signals (1-5) has generated considerable interest in applying MRI to dense tissues. For example, cortical bone, which is conventionally imaged using X-ray-based methods, can now be effectively imaged with MRI (3,5-9) and its ^1H NMR signal characteristics report on bone damage (10) and mechanical properties (11,12). In particular, recent studies show that cortical bone NMR signals of transverse relaxation time constant (T_2) $\approx 400 \mu\text{s}$ are due primarily to collagen-bound water (13-17) and correlate directly (and more strongly than X-ray based measures) with several mechanical properties of cortical bone (18). Similarly strong inverse correlations were found between signals with $T_2 > 1 \text{ ms}$, due primarily to pore water, and the same mechanical properties (18). These findings demonstrate the potential for MRI to offer diagnostic measures of bone fracture risk, but the opposing relationships of bound and pore water content with mechanical properties requires MRI methods that distinguish signals from these two biophysical origins. One approach for distinguishing long- from short- T_2 signals in uTE imaging is through T_2 selective RF pulses (19-23). For cortical bone, the broad line widths of both bound and pore water signals (13) dictate the use of relatively high bandwidth RF pulses, which can be realized with

intrinsically T_2 -selective adiabatic pulses (24,25). Presented here are clinically-practical MRI methods for distinguishing bound and pore water signals from cortical bone based on T_2 -selective adiabatic pulses as well as T_1 characteristics of cortical bone bound and pore water. Signals from each method are found to correlate well with previously employed non-imaging methods and with measured bone mechanical properties, offering promise for their use *in vivo* as a diagnostic measure of bone fracture risk.

5.2 — Theory: A Model for the NMR Lineshape of Water in Cortical Bone

In order to explain the widely different T_2 s but apparently similar T_2^* s arising from bound and pore water, consider a simple, qualitative model of the observed free induction decay (FID) rate as a sum of reversible and irreversible transverse relaxation rates. That is $R_2^* = R_2 + R_2'$, where $R_2^* = 1/T_2^*$ is the observed transverse relaxation rate in the FID, $R_2 = 1/T_2$ is the time-irreversible rate as observed in a Carr-Purcell-Meiboom-Gill (CPMG) measurement, and R_2' is the time-reversible rate. With this model, consider bound water to exhibit $R_2 \gg R_2'$ (such that $R_2^* \cong R_2$), a condition of so-called homogenous line-broadening. This arises from dipolar interactions of motionally-restricted bound water spins throughout the

bone matrix space, as well as from magnetization transfer with dipolar broadened collagen/semisolids observed in (9,13). Conversely, consider the pore water signal to result from the sum of numerous isolated free water pools, each with relatively low R_2 values but collectively with off-resonant frequencies described by a broad distribution. Such would be the case for the polydisperse pore size distribution observed in bone (e.g. Haversian canals, lacunae, and canaliculi (15,26)), wherein pores contain motionally-averaged mobile water surrounded by a bone matrix of different magnetic susceptibility (27). Thus, the pore water FID is primarily governed by R_2' (such that $R_2^* \cong R_2'$), a condition of so-called inhomogenous line-broadening. In this sense, cortical bone pore water bears similarity to water within porous media (14). Figure 5.1 demonstrates NMR frequency-domain representations of this bound/pore water model, and indicates that to effectively manipulate the bulk pore water magnetization a broadband RF pulse is needed to nutate the full distribution of individual off-resonant pore magnetizations within the bulk pore water lineshape.

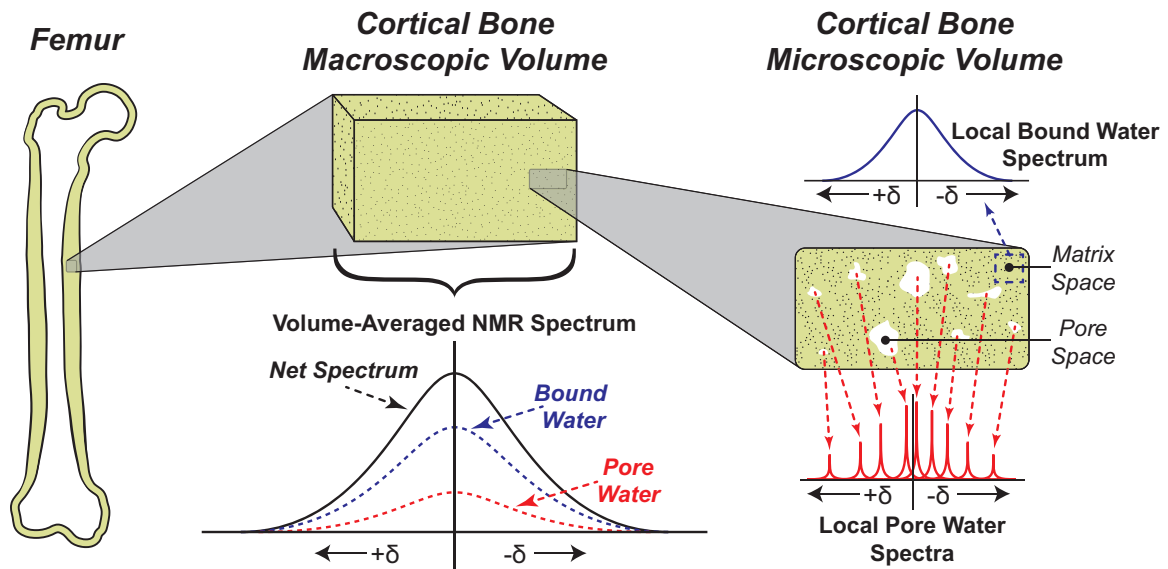


FIGURE 5.1 A model of the water ^1H NMR lineshapes in human cortical bone. Across a macroscopic volume of cortical bone akin to an MRI voxel (middle), numerous bound and pore water components are combined into a broad net NMR spectrum with similarly broadened bound and pore water contributions. On the local microscale (right), bound water in the bone matrix space gives rise to a homogeneously broadened NMR spectrum. Conversely, the relatively mobile water within each pore space gives rise to a narrower NMR spectrum of varied chemical shift (dictated by pore geometry and pore-matrix susceptibility variation). The sum of these microscale contributions gives rise to a heterogeneously broadened pore water lineshape across macroscopic bone volumes (middle).

5.3 — Theory: T_2 Selective Adiabatic RF pulses

From the model above and previous wide-line NMR studies (13,28), it is readily apparent that any RF pulse designed to perturb the entire pore water magnetization must possess a relatively large bandwidth (≈ 3500 Hz at 4.7T, estimated ≈ 2000 Hz at 3.0T). A conventional amplitude modulated RF pulse with this bandwidth would be short in duration and similarly responsive for T_2 s of both bound and pore water. However, an adiabatic pulse has an additional

degree of freedom in design by way of its frequency modulation and can invert spins across a wide bandwidth using a relatively long, frequency-swept RF waveform. Although relaxation during an adiabatic pulse is complicated due to the spectral density contribution at $\gamma B_1(t)$ (29), we approximate such relaxation with the Bloch equations and invariant T_1 and T_2 relaxation time constants. Figure 5.2 shows the effect of a 5 ms duration, 5 kHz bandwidth hyperbolic secant (sech) adiabatic full passage (AFP) pulse (24) applied to equilibrium magnetization, as determined by numerical solution of the Bloch equations.

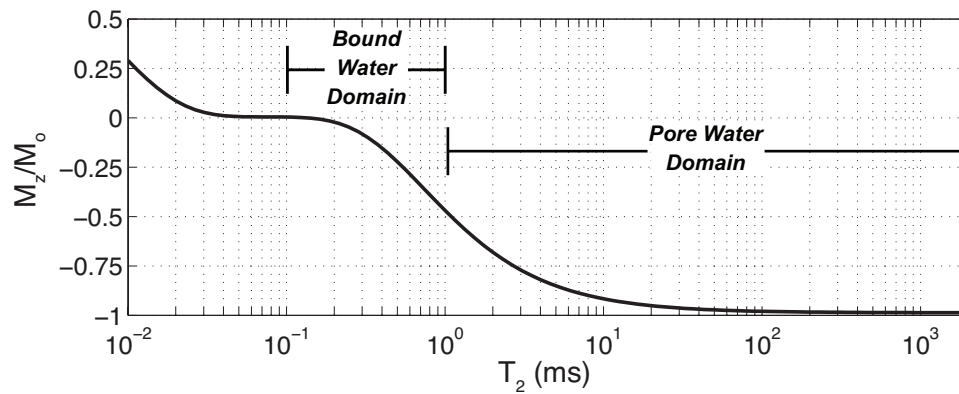


FIGURE 5.2 *Simulated effects of a sech AFP pulse on cortical bone water longitudinal magnetization.* Bloch equation simulation of a 5ms/5kHz AFP shows a significant T_2 dependence of the AFP inversion efficiency (above). Such an AFP pulse is expected to largely saturate and invert the bound and pore water magnetizations, respectively, given their considerably different T_2 domains noted above.

This figure demonstrates the T_2 -selectivity of such RF pulses, in accord with previous work (22,25), and their suitability for differentially rotating bound water ($T_2 < 1$ ms) and pore water ($T_2 > 1$ ms) magnetizations. The inversion

efficiency of a given RF pulse is described by a scalar multiplier ($-1 \leq \alpha \leq 1$) representing the change in longitudinal magnetization caused by each AFP pulse.

5.4 — Theory: Ultra-short Echo Time Pulse Sequences

Figure 5.3a shows a conventional uTE sequence (CuTE), wherein the first data points are collected at an ultra-short echo time, typically $< 100 \mu\text{s}$ (1). With such a short echo time, the CuTE signal will contain contributions from both bound and pore water. Acquisition strategies such as a multiple gradient echo or spectroscopic readout (5,30) can be added to CuTE to measure FID signal characteristics for the purpose of discriminating bound from pore water in the T_2^* domain. To this end, a spectroscopic method with bi-exponential- T_2^* analysis of the uTE signal (herein, BEuTE) has recently been reported (31).

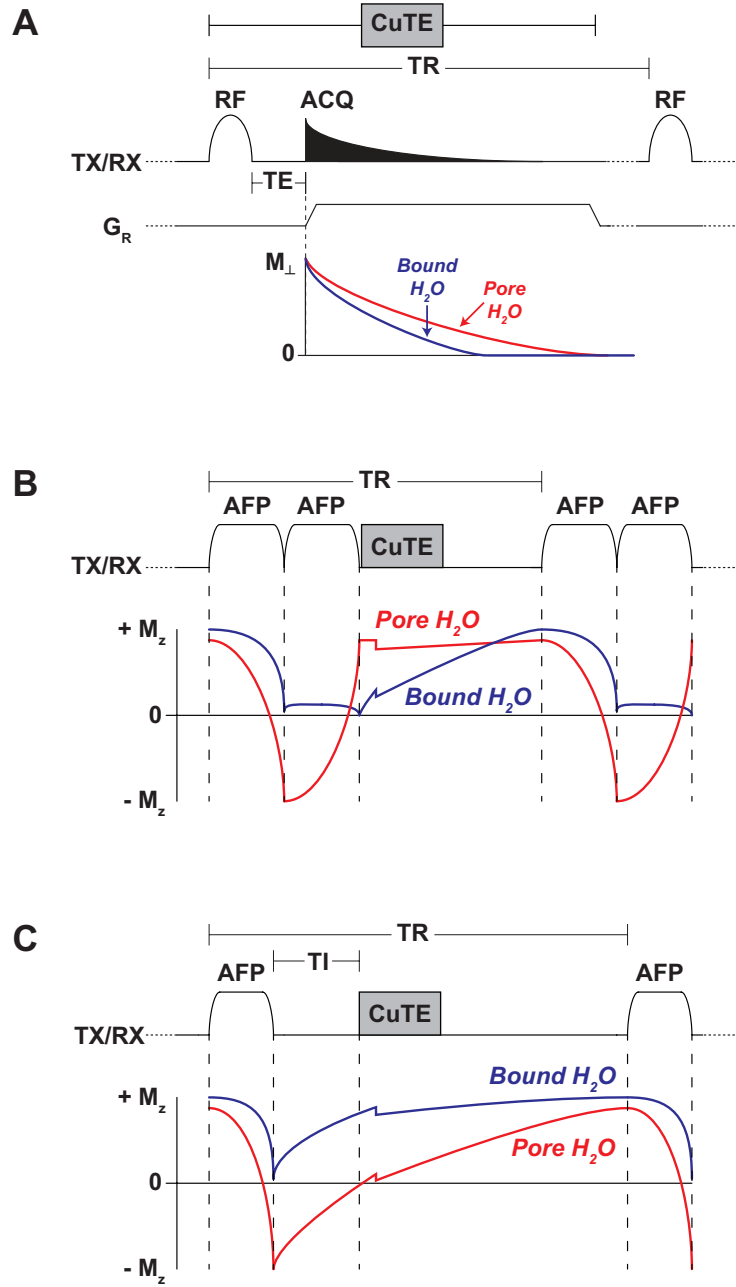


FIGURE 5.3 Proposed ultra-short echo time-based approaches for MRI of cortical bone net, pore, and bound water content. The CuTE sequence in A is sensitive to both bound and pore water, but their similar T_2^* present difficulties in quantitatively distinguishing bound from pore water if spectroscopic acquisition schemes are employed for BEuTE (see subplot). Incorporating a double-AFP T_2 filter (DAFP) into the uTE sequence (B) drives the steady state bound water longitudinal magnetization to saturation at readout, thus creating a signal dominated by pore water. Conversely, the adiabatic inversion recovery (AIR) scheme in C drives pore water to saturation, creating a predominantly bound water signal. (TR=repetition time, TI=inversion time, G_R = readout gradient, RF=slice or volume excitation).

In this approach, with a two-compartment model of bound water (bw) and pore water (pw) assuming no inter-compartmental magnetization exchange, the signal magnitude equation for the BEuTE signal is simply,

$$S_{uTE}(TE_i) = S_0^{bw} \sin \theta \frac{1 - e^{-R_1^{bw} TR}}{1 - e^{-R_1^{bw} TR} \cos \theta} e^{-R_2^{*bw} TE_i} + S_0^{pw} \sin \theta \frac{1 - e^{-R_1^{pw} TR}}{1 - e^{-R_1^{pw} TR} \cos \theta} e^{-R_2^{*pw} TE_i} \quad [1],$$

where TE_i is the time after excitation of i^{th} the signal datum, TR is the sequence repetition time, θ is the excitation pulse flip angle, R_1^{bw} and S_0^{bw} are the longitudinal relaxation rate and relative proton density, respectively, of bound water, and likewise for R_1^{pw} and S_0^{pw} of pore water. Given *a priori* estimates of R_1^{bw} and R_1^{pw} , the observed signal, $S_{uTE}(TE_i)$, can be fitted with Eq [1] to estimate $S_0^{bw, pw}$ and $R_2^{*bw, pw}$. (More on required *a priori* information for this and other sequences below.)

Challenges to the BEuTE approach include similarly short T_2^* characteristics of bound and pore water (Fig 5.1) that will likely converge with increasing field strength, off-resonance effects leading to non-monotonic decays, potentially non-lorentzian lineshapes associated with short T_2 s, and the need for spectroscopic imaging with sufficient sampling of the $\approx 50 \mu s$ to 5 ms TE domain. While practical spectroscopic imaging with bi-exponential fitting has recently

been demonstrated in the context of bone MRI (30,31), it has yet to be rigorously evaluated with regards to bound/pore water T_2^* discrimination. However, with spectroscopic or multiple gradient echo techniques, bound and pore water should be clearly distinguishable from surrounding soft tissue signals (marrow, muscle, fat, etc.), which have significantly longer T_2^* values ($\gg 10$ ms) than cortical bone water.

5.5 — Theory: Double Adiabatic Full Passage (DAFP) Pulse Sequence

A pair of sequential AFP pulses incorporated into the CuTE sequence (Fig 5.3b) will rotate pore water magnetization through 360° while approximately saturating the bound water magnetization (see Fig 5.2). Thus, the DAFP signal is comprised primarily of pore water with a magnitude described by

$$S_{DAFP} \approx S_o^{pw} \sin \theta \frac{1 - (\alpha^{pw})^2 e^{-R_1^{pw} TR}}{1 - (\alpha^{pw})^2 e^{-R_1^{pw} TR} \cos \theta} e^{-R_2^{*pw} TE} \quad [2].$$

Given *a priori* estimates of R_1^{pw} and R_2^{*pw} and knowledge of the inversion efficiency of the AFP pulse on the pore water magnetization, α^{pw} , the pore water proton density, S_o^{pw} , can be estimated from the observed signal, S_{DAFP} . As noted

above, the long- T_2^* surrounding tissue signal may still be suppressed if a multiple gradient echo/spectroscopic readout is employed.

5.6 – Theory: Adiabatic Inversion Recovery (AIR) Pulse Sequence

An AFP pulse added to the CuTE sequence (Fig 5.3c) will largely invert pore water while approximately saturating the bound water, following which an appropriate inversion recovery delay (TI) can be chosen to null pore water magnetization. Thus, the signal is comprised primarily of bound water with a magnitude described by

$$S_{AIR} \approx S_o^{bw} \sin \theta \frac{1 - (1 - \alpha^{bw}) e^{-R_1^{bw} TI} - \alpha^{bw} e^{-R_1^{bw} TR}}{1 - \alpha^{bw} e^{-R_1^{bw} TR} \cos \theta} e^{-R_2^{*bw} TE} \quad [3].$$

If TI is chosen to null signal from pore water, this equation can be re-written as

$$S_{AIR} = S_o^{bw} \sin \theta \frac{1 - (1 - \alpha^{bw}) \left(\frac{1 - \alpha^{pw} e^{-R_1^{pw} TR}}{1 - \alpha^{pw}} \right)^{R_1^{bw} / R_1^{pw}} - \alpha^{bw} e^{-R_1^{bw} TR}}{1 - \alpha^{bw} e^{-R_1^{bw} TR} \cos \theta} e^{-R_2^{*bw} TE} \quad [4].$$

Given *a priori* estimates of R_1^{bw} , R_1^{pw} , R_2^{*bw} and α^{bw} , the bound water density, S_o^{bw} , can be estimated from the observed signal, S_{AIR} . Because pore water R_1 is relatively similar to those of surrounding soft tissue (compared with bound water), the AIR sequence will naturally suppress surrounding tissue and has

been previously used for this purpose expressly (8,32). But again, as above, this suppression may be further improved through a multiple gradient echo/spectroscopic acquisition.

5.7 – Theory: Absolute Water Concentration

For all of the above measurements, the estimated relative water density, S_0^{bw} or S_0^{pw} , requires an *a priori* estimate of one or more of R_1 , R_2^* , or α , for bound and/or pore water, as indicated in Eqs [1-4]. Previous work indicates that across individuals mean R_2^{bw} is relatively constant (13). One can expect R_2^{*bw} , R_1^{bw} and α^{bw} to be so as well, making the choice of their values relatively unimportant as long as the same value is used for calculating S_0^{bw} across individuals. Pore water signal characteristics are more likely to vary across individuals with different pore sizes, so some variation in R_1^{pw} , R_2^{*pw} , and α^{pw} is expected (due to the pore geometry dependence of R_2^{pw} (15,16)). In practice, using a reasonably short echo time (TE \leq 50 μ s) mitigates the importance of the *a priori* estimate of R_2^{*pw} , and the impact of variations in R_1^{pw} and α^{pw} across a small (N = 14) collection of bone samples is evaluated below.

5.8 — *Experimental Methods Overview*

The proposed pulse sequences and signal equations were evaluated with the following procedure:

- 1) Establish population-averages of the required *a priori* parameter estimates ($R_1^{bw, pw}$ and $\alpha^{bw, pw}$).
- 2) Measure the relative contributions of bound and pore water to BEuTE, CuTE, DAFP and AIR methods by bi-exponential T_2^* (BEuTE) or multi-exponential T_2 characterization (CuTE/DAFP/AIR) of their signals.
- 3) Correlate estimates of S_0 from BEuTE, CuTE, DAFP and AIR signals to gold-standard equilibrium CPMG measurements and to cortical bone mechanical properties.

5.9 — *Experimental Methods: Human cortical bone preparation*

The Musculoskeletal Tissue Foundation (Edison, NJ), a non-profit tissue allograft bank, and the Vanderbilt Donor Program (Nashville, TN) supplied human femurs from 14 cadaveric donors (8 male, 6 female, 22-98 years old, mean \pm standard deviation (SD) = 70 ± 25 years) under instruction to not provide tissue from donors who had tested positive for a blood borne pathogens. Cortical bone specimens for either NMR or mechanical testing were extracted from adjacent

sites in the medial mid-shaft of each donor's right femur and were machined to \approx 10 \times 2 \times 4 mm or 40 \times 2 \times 4 mm dimensions, respectively, providing uniform cortical bone, free of endosteal and periosteal surfaces. Note that volume of the NMR samples, determined by digital caliper measurement, was on the order one or a few voxels in a typical lower leg quantitative uTE bone image (6). Specimens were stored in phosphate-buffered saline at -80 °C between processing and measurements, and specimens were thawed at 4 °C approximately 18 hours prior to measurements. Immediately prior to NMR measurements, thawed specimens were removed from PBS and blotted dry to remove pooled surface water.

5.10 — Experimental Methods: Mechanical Testing

Standard three point bend mechanical testing was performed at room temperature to determine several mechanical properties relevant to fracture risk in bone: flexural modulus, yield stress, peak stress, fracture stress, and toughness to failure. A material testing system (Dynamight 8841; Instron, Canton, OH) recorded the force-displacement data from a 100 N load cell and the linear variable differential transformer at 50 Hz. Hydrated bone was loaded to failure at 5 mm/min on a 35 mm support span. Various mechanical properties were determined from force-displacement data following the standard methods described previously (18).

5.11 — *Experimental Methods: NMR*

NMR measurements were performed at 200 MHz and $\approx 20^\circ\text{C}$ using a 4.7T horizontal bore magnet with a DirectDrive console (Varian/Agilent, Santa Clara, CA). An in-house loop-gap style RF coil with Teflon structural support was used (similar to the coil described in (33)), which provided $90^\circ/180^\circ$ RF pulses of $\approx 5\ \mu\text{s}/10\ \mu\text{s}$ duration and contributed negligible background ^1H signal ($<1\%$ of net cortical bone signal). In all NMR measurements, bone specimens were placed with osteonal direction orthogonal to B_0 to maintain consistent magic angle effects. In all measurements of the CuTE, DAFP, and AIR sequences, a microsphere containing 21.2 μL of deionized H_2O ($T_2 \approx 2.5\ \text{s}$) was placed adjacent to bone specimens as a reference marker for signal size quantitation. Also, to ensure there were no significant time-dependent changes of the bone T_2 characteristics during NMR measurements, equilibrium CPMG measurements were collected before and after each series of measurements.

Using experimental parameters described elsewhere (13), transverse relaxation was measured at equilibrium with a CPMG pulse sequence (100 μs echo spacing), and longitudinal relaxation was characterized with inversion-recovery-prepared CPMG (IR-CPMG). To observe the effects of a single AFP pulse on bound and pore water signals in cortical bone (α^{bw} and α^{pw}), the CPMG

measurements were repeated with and without a preparatory sech pulse (AFP-CPMG) of varying duration and bandwidth (Table 5.1). During a 5 ms delay between the sech pulse and the excitation RF of the CPMG acquisition, a spoiler gradient (2 ms, 10 G/cm) removed any net transverse magnetization.

T (ms)	BW (kHz)	β (rad/s)	μ	$\gamma B_{1,max}$ (Hz)
5	1	2120	1.48	821
5	2	2120	2.96	1162
5	3.5	2120	5.19	1537
5	5	2120	7.41	1837
10	1	1060	2.96	581
10	2	1060	5.93	821
10	3.5	1060	10.38	1087
10	5	1060	14.82	1299
15	1	706	4.45	474
15	2	706	8.89	671
15	3.5	706	15.56	887
15	5	706	22.24	1060

TABLE 5.1 *Combinations, by rows, of adiabatic full passage pulse parameters used herein.*

CuTE and DAFF and AIR sequences were driven to steady state by replacing their uTE imaging modules (Fig 5.3) with a non-imaging acquisition: hard RF excitation (10 μ s, 20°) followed by an FID acquisition and a subsequent spoiler gradient (5 ms, 10 G/cm). FID and CPMG acquisitions were collected at

steady state. The DAFP and AIR sequences used sech pulses of 10 ms duration and 3.5 kHz BW. (These pulses used $\approx 24 \mu\text{T}$ peak B_1 , which is near the maximum available on typical human MRI systems but can be reduced by using higher order hyperbolic secant, H_{Sn} , pulses (34)). Both AIR and DAFP used $\text{TR} = 300$ ms; CuTE used $\text{TR} = 35$ ms. AIR measurements were repeated with 11 TI values spanning 70-110 ms to empirically determine a single optimal TI for nulling pore water across all specimens.

The BEuTE method was evaluated by analyzing non-imaging FIDs collected from equilibrium magnetization (pulse-acquire measurement: $\text{TR} = 5$ s, 90° flip, acquisition of a 10 ms window at 2.5 MHz bandwidth, 64 averages, 8 μs receiver dead time prior to acquisition). These equilibrium FIDs provide an idealized testbed for evaluating the BEuTE method, as they are free of imaging artifacts and unwanted coherence pathways potentially present in the steady state imaging version of BEuTE. Bound and pore water T_1 -weighting, which is not present in the equilibrium FIDs but would be in BEuTE imaging, is not required to evaluate the soundness of the BEuTE method.

5.12 — Experimental Methods: Data Analysis

All data processing was performed using MATLAB (The Mathworks, Natick, MA). The freely-available MERA_Toolbox (Multi-Exponential Relaxation

Analysis, http://vuiis.vanderbilt.edu/~doesmd/MERA/MERA_Toolbox.html) provided a regularized non-negative least-square (NNLS) approach to estimate multi-exponential T_2 spectra from CPMG data and T_1 - T_2 spectra from IR-CPMG data as described in (13). Because AFP-CPMG measurements contained decaying signals of both positive and negative amplitude, direct NNLS analysis was not possible. Instead, the complex AFP-CPMG signals were first summed with the complex equilibrium-CPMG signals, and the resulting summed signal, comprised solely of non-negative amplitude decaying exponentials, was fitted with a T_2 spectrum. This T_2 spectrum was then subtracted on a peak-by-peak basis from the equilibrium T_2 spectrum to construct an estimated AFP-CPMG T_2 spectrum.

Population averaged bound/pore R_1 s were computed from each specimen's T_1 - T_2 spectra by computing the mean R_1 in the appropriate T_2 domains (for bound and pore water) and the resulting R_1 s were averaged across all specimens. A population average for net water R_1 (R_1^{nw}) was similarly computed from mean R_1 s across both bound and pore water T_2 domains. Population averaged AFP efficiency parameters, α^{bw} and α^{pw} were estimated by dividing bound or pore water T_2 spectral intensities from the AFP-CPMG

measurements by those from the equilibrium CPMG measurements and then averaging across specimens.

Steady state longitudinal magnetizations of CuTE, DAFP, and AIR pulse sequences were discriminated on a T_2 basis via NNLS fitting of CPMG data collected in the final TR periods. CuTE CPMG data satisfied the NNLS constraint, so fitting directly gave T_2 spectra. However DAFP and AIR CPMGs potentially contained both positive and negative decays, so T_2 spectra were calculated in the same manner as those from AFP-CPMG data (described above).

FIDs from the CuTE, DAFP, and AIR sequences were quantified similarly to previous in vivo studies that employ reference signals (6,7), although transverse relaxation decay during TE periods was not considered (assumed $TE \ll T_2^*$ in all sequences). FID magnitudes at $TE = 50 \mu s$, which consisted of both short- T_2^* bone water and long- T_2^* marker water, were stripped of long- T_2^* contributions by subtracting magnitudes at $TE = 3 ms$, and the resulting signal was defined as S_{CuTE} , S_{DAFP} , or S_{AIR} . (When imaging, the reference signal would be spatially resolved from cortical bone and so the long-TE signal subtraction would only be used to suppress contaminating soft tissue signals.) S_{CuTE} and R_1^{nw} were then used with a mono-exponential form of Eq [1] (e.g. the standard spoiled gradient echo signal equation) to estimate the net water proton density, S_o^{nw} ,

while S_{DAFP} , S_{AIR} and the appropriate population-averaged *a priori* parameter estimates were used with Eq [2] or [3] to estimate S_0^{bw} or S_0^{pw} . To convert S_o^{mw} , S_0^{bw} , and S_0^{pw} into units of absolute proton concentration, these estimates were multiplied by $V_{\text{ref}}\rho_{\text{ref}}/V_{\text{bone}}S_o^{\text{ref}}$, where V_{ref} and V_{bone} are the water reference and bone volumes, respectively, $\rho_{\text{H}_2\text{O}} = 111.1 \text{ mol } ^1\text{H}/\text{L}_{\text{H}_2\text{O}}$ was the assumed proton concentration of the reference, and S_o^{ref} is the total signal arising from the water marker (obtained by integrating the the equilibrium CPMG T_2 spectrum over $T_2\text{s} > 1000 \text{ ms}$, where the entire marker signal is clearly discriminated from bone water). Resulting proton concentration estimates from the CuTE, DAFP, and AIR signals were pairwise linearly regressed to the aforementioned bone mechanical properties, as well as to gold-standard measures of net, pore, and bound water, respectively. These gold-standard measures were calculated from equilibrium CPMG-derived T_2 spectra by integrating over the appropriate T_2 domains, as previously demonstrated in (13,18).

Equilibrium FIDs, chosen as surrogates to BEuTE signals (see rationale above), were fit with bi-exponential decays via least-squares fitting to Eq [1], assuming $e^{-R_1TR} \approx 0$ (i.e. $TR \gg T_1$). FIDs were fit across a time domain of 50 μs to

4.5 ms (similar to that shown in the aforementioned bone bi-exponential imaging study (31)) to isolate bound and pore water decays while avoiding signal from a large matrix-related $T_2 \approx 10 \mu\text{s}$ component. Resulting short and long- T_2^* signal fractions were compared to the fractions of bound and pore water (relative to total water) determined from gold-standard equilibrium CPMG T_2 spectra. While this gave a straightforward evaluation of BEuTE's ability to discriminate bound and pore water, short and long- T_2^* signal sizes were also converted to units of proton concentration (via the aforementioned $V_{\text{ref}}\rho_{\text{ref}}/V_{\text{bone}}S_o^{\text{ref}}$ factor), which were pairwise linearly regressed to bone mechanical properties for the purpose of comparing the diagnostic utility of BEuTE to that of CuTE, DAFP, and AIR. Since the water reference was not present during equilibrium FID measurements (to avoid confounding off-resonance effects), this quantitation step used water reference signals acquired in separate experiments, which introduced another source of experimental variance but was expected to be negligible (on the order of 5% of the water reference's signal size (13)).

5.13 — *Experimental Findings*

Figure 5.4A shows representative cortical bone CPMG decays collected with and without a 5 ms duration, 5 kHz bandwidth AFP preparatory pulse. It is clear that

the AFP pulse largely saturates the submillisecond- T_2 bound water while strongly inverting the long-lived pore water T_2 s. These effects are shown in Fig 5.4B on a peak-wise basis for three specimens subjected to various AFP bandwidths; similar results (not shown) were obtained at the other AFP pulse durations in Table 5.1. All but the narrowest bandwidth AFP pulses generally trended with the simulations (e.g. Fig 5.2), although some positive bias is generally observed. The narrowest bandwidth AFPs (1000 Hz) all failed to strongly invert long- T_2 pore water. The α^{bw} was extracted from the 10ms/3.5kHz AFP-CPMG data and ranged 0.08-0.11 (mean \pm std: 0.09 ± 0.01) across all specimens, while α^{pw} ranged from -0.90 to -0.65 (mean \pm std: -0.78 ± 0.07). These mean α^{bw} and α^{pw} values were used in all signal quantitation.

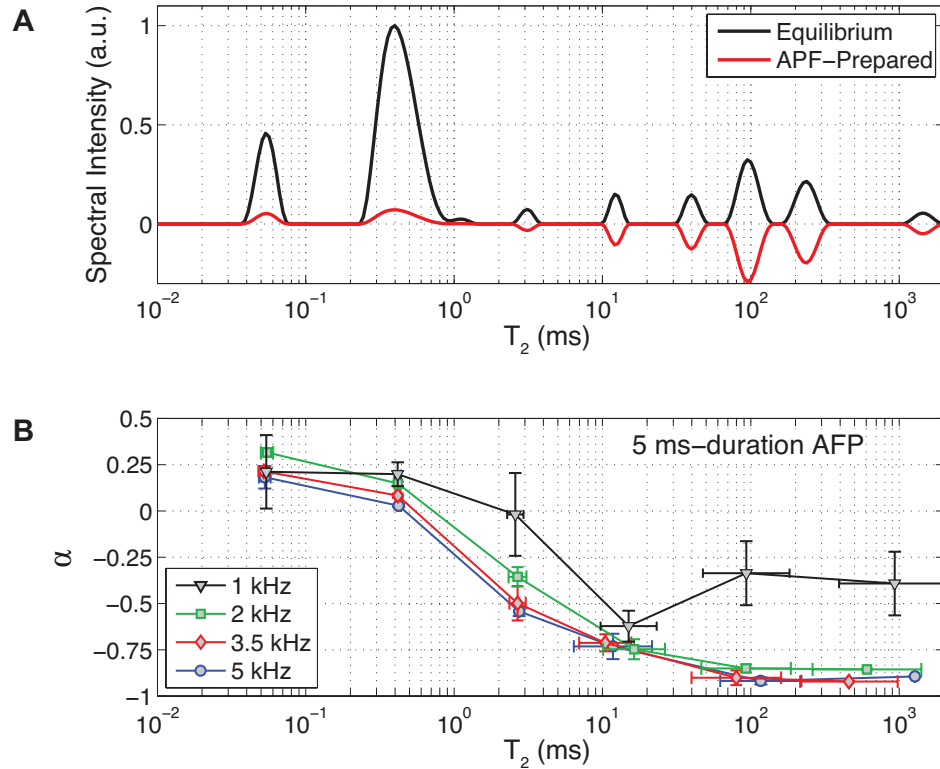


FIGURE 5.4 Observed effects of a sech AFP pulse on cortical bone water longitudinal magnetization. T_2 spectra (A) from a representative bone specimen at equilibrium and following an AFP pulse (5ms/5kHz) show a largely saturated bound water component ($T_2 \approx 0.4$ ms) and inverted pore water ($T_2 > 1$ ms), as represented by the negative spectral amplitudes (see Methods for details). The ratio of AFP-prepared to equilibrium T_2 spectral peak areas gives the APF efficiency parameter α , shown in B for a variety of AFP bandwidths (error bars represent ± 1 SD across specimens).

T_1 - T_2 spectra from IR-CPMG resembled those shown elsewhere (13). As previously described, population-averaged pool T_1 s extracted from these spectra were used in all signal quantitation. Bound water T_1 s were consistent across specimens, ranging 340-370 ms (mean \pm std: 357 ± 10 ms), while pore water T_1 s exhibited a wider range of 380-775 ms (mean \pm std: 551 ± 120). Net T_1 s (weighted average of bound and pore water) ranged 380-450 ms (mean \pm std: 412 ± 20 ms).

Bi-exponential fitting results for evaluating the BEuTE method are given in Fig 5.5. Across the specimens, the short- T_2^* component ranged 230-370 μs (mean \pm std: 290 ± 40), while the long- T_2^* component ranged 520-1800 μs (mean \pm std: 1280 ± 360).

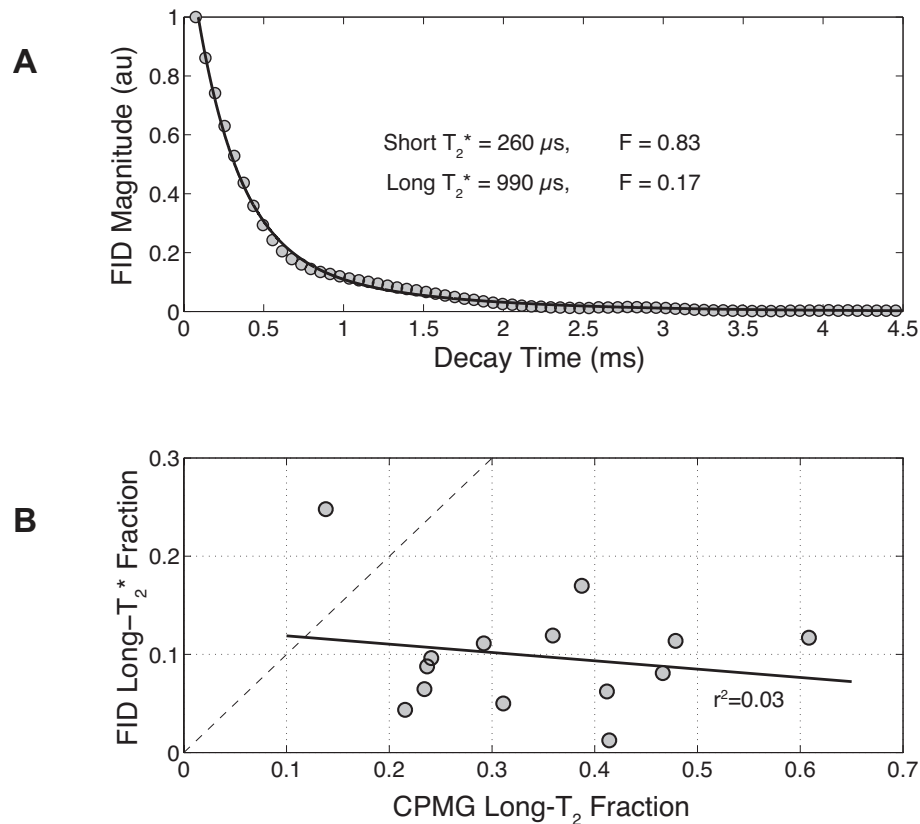


FIGURE 5.5 *Bi-exponential fitting for bound/pore water separation in the T_2^* domain. A representative cortical bone equilibrium FID and bi-exponential fit is shown with resulting T_2^* and signal fraction values at inset (A). Across the specimens (B), the long- T_2^* signal fraction obtained from FID bi-exponential fitting was poorly correlated to the long- T_2 ($1\text{ms} < T_2 < 1\text{s}$) signal fraction obtained from CPMG multi-exponential fitting, the latter of which is known to arise predominantly from pore water. Thus, FID data were poor indicators of pore water content.*

A representative fit is shown in Fig 5.5A. The signal fractions of the long- T_2^* component ranged 0.01-0.25 across specimens (mean \pm std: 0.10 ± 0.06) and were in poor agreement with the long- T_2 signal fractions derived from equilibrium CPMG measurements (Fig 5.5B), which ranged 0.14-0.61 (mean \pm std: 0.29 ± 0.10). The large bias and lack of trending in Fig 5.5B shows that signal fractions obtained from the BEuTE method are poor indicators of CPMG signal fractions, the latter of which are known to represent bound/pore water content (13-17).

T_2 -resolved signal components present in the CuTE, DAFP, and AIR signals are shown in Fig 5.6A-C. Bound, pore, or net water proton concentrations determined from in each strategy are compared to gold-standard equilibrium-CPMG-derived concentrations in Fig 5.6D-F, and there was a strong linear correlation ($r^2 \geq 0.7$) in all cases. CuTE/DAFP/AIR-derived proton concentrations agreed well with with net/pore/bound water concentrations derived from equilibrium CPMG, with no statistically significant bias (dashed lines in Fig 5.6D-F are 95% confidence intervals, which included the line of unity in all cases). For the AIR sequence, a single TI of 90 ms was found to give the best pore water suppression across all specimens.

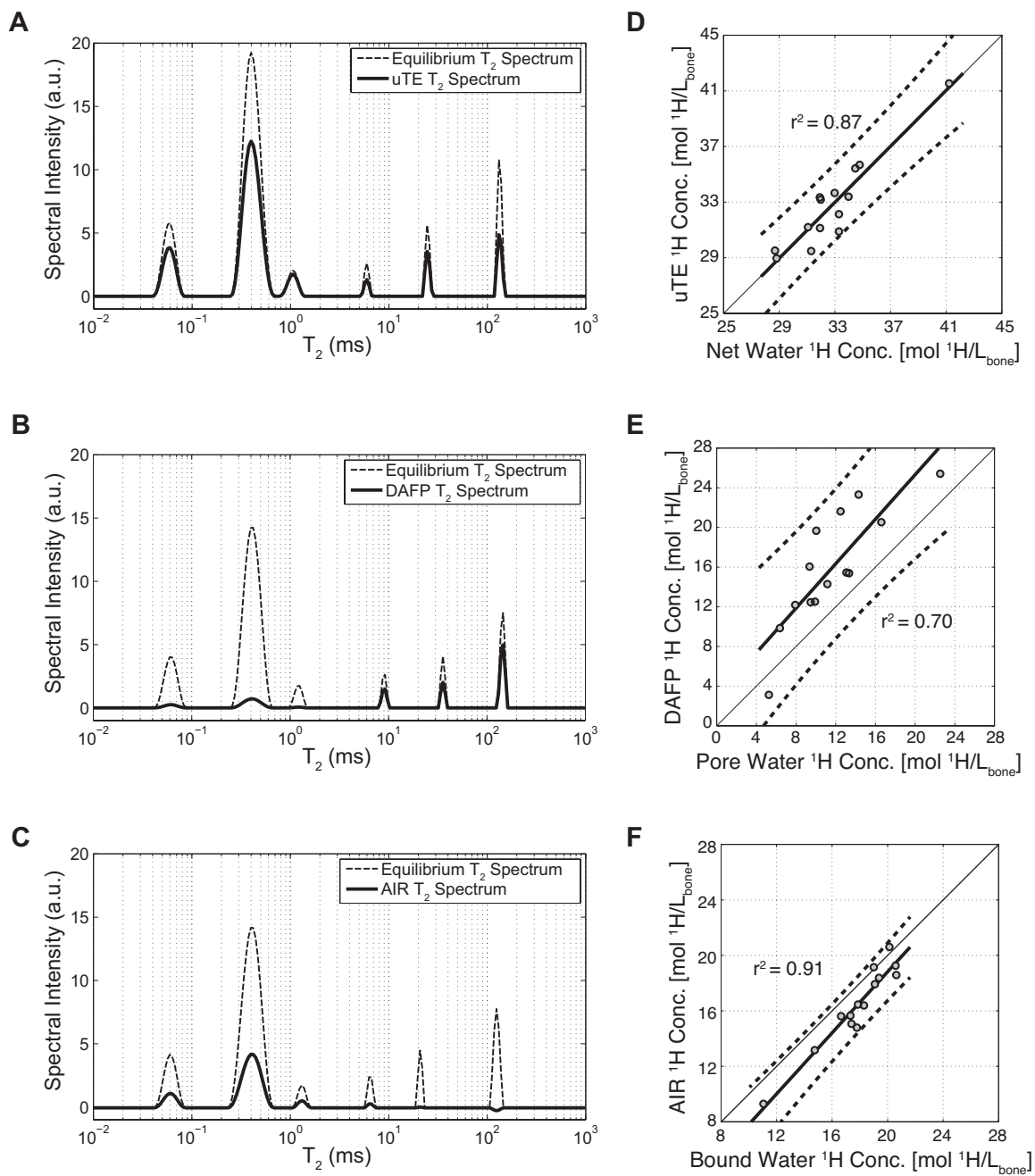


FIGURE 5.6 Signal contents and correlations to gold standard measures for the uTE, DAFP, and AIR methods. T_2 spectra from CPMGs collected at steady state show that the net uTE signal contains a mixture of both bound and pore water contributions (A), while the DAFP signal is dominated by pore water (B) and the AIR signal by bound water (C). For each method (D-F), estimates of M_0 from the steady state FID signal—quantified in absolute units of proton concentration—correlated satisfactorily to gold-standard measures of net, pore, or bound water as determined by equilibrium T_2 spectroscopy.

Figure 5.7 shows correlations between mechanical properties and water concentrations derived from BEuTE/CuTE/AIR/DAFP signals, which are closely analogous to the clinical imaging pixel intensities that could be obtained from these methods. An example of correlations to peak stress is given in Fig 5.7A, and Pearson's r^2 between the different strategies and mechanical parameter pairings are given in Fig 5.7B. BEuTE and CuTE failed to give any statistically significant correlation ($P < 0.05$), but AIR and DAFP correlated well to all mechanical properties (r^2 ranged 0.35 to 0.69).

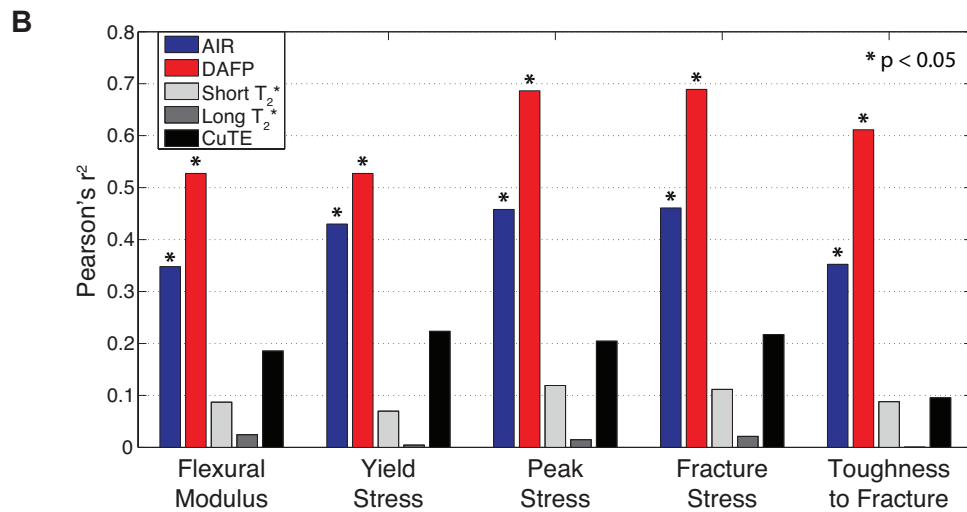
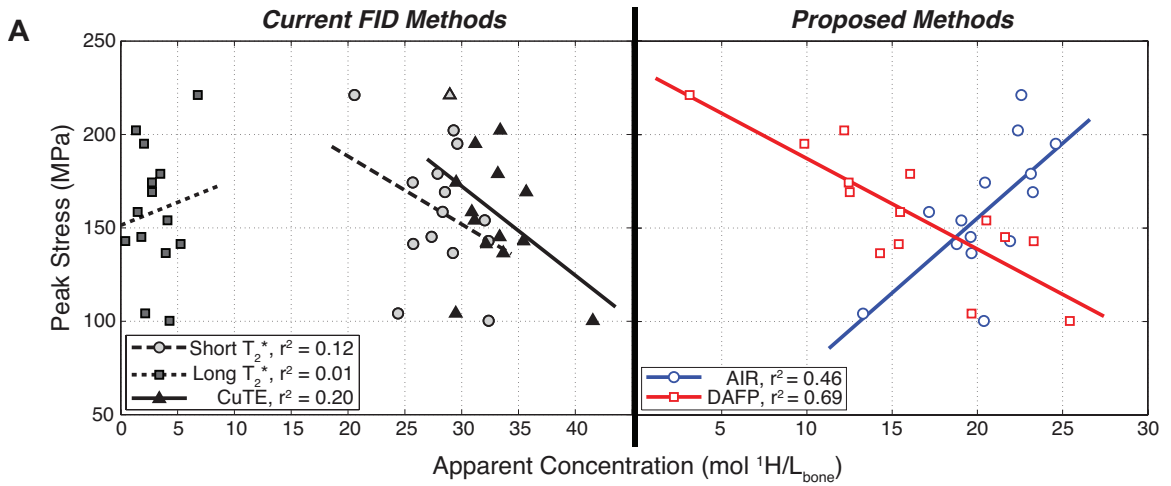


FIGURE 5.7 *Mechanical property correlations to steady state signals across specimens.* Linear correlations to peak stress are shown for proton concentrations derived from BEuTE (short/long- T_2^*) and CuTE methods (A, left) as well as for concentrations derived from the proposed AIR/DAFP methods (A, right). Pearson's r^2 s for correlations between the different methods' water concentrations and various mechanical properties are summarized in B. While AIR and DAFP were good correlates to mechanical properties, none of the FID methods exhibit statistically significant correlations ($p < 0.05$) for any of the mechanical properties surveyed.

5.14 — Discussion

Discrete transverse relaxation components of the ^1H NMR signal have been well characterized in cortical bone (13-17,28). Relevant to this study, a dominant T_2 component of $\approx 400 \mu\text{s}$ and a broad distribution of components spanning 1ms - 1s have been consistently observed in numerous human cadaveric donors.

Through a variety of techniques such as $\text{H}_2\text{O}/\text{D}_2\text{O}$ exchange, the $400 \mu\text{s}$ T_2 signal has been attributed to matrix-bound water and the longer-lived signals to pore space water (12,13,35). Recently, a direct linear correlation between the bound water signal size and important mechanical properties such as peak stress has been observed, indicating that, in principle, MRI signals can be used to assess bone fracture risk (18). However, an inverse linear correlation with the pore water signal size results in a complete loss of predictive power if both bound and pore water contributions are included in the same MRI measurement. Thus, diagnostically-relevant cortical bone image contrast relies on discriminating bound from pore water. To this end, we present a qualitative model of cortical bone relaxation, wherein the bound and pore water signals undergo predominantly homogenous and inhomogenous line-broadening (i.e. irreversible and reversible transverse relaxation), respectively. In light of this model, we evaluate clinically-applicable uTE-based AIR and DAFP schemes for quantitative

bound and pore water signal discrimination, which would act as surrogates to the diagnostically-useful but clinically-impractical CPMG measurements in (13,18). Undiscriminated water signal quantitation has been successfully implemented on clinical scanners (6,7) via phantoms with known composition and NMR parameters, and we demonstrate an analogous procedure herein with the AIR and DAFP strategies to demonstrate their bound or pore water selectivity in comparison to existing BEuTE/CuTE bone imaging methods.

5.15 — Discussion: A Model for Bound and Pore Water Transverse Relaxation in Human Cortical Bone

The model of inhomogeneously-broadened and spatially-sequestered pore water is supported by observations of both its long T_2 ($\gg 1$ ms) and short T_2^* (≈ 1 ms), as well as the poor inversion performance of narrow-band AFPs (Fig 5.4). Thus, the broad pore water NMR spectral line is interpreted as a superposition of chemically-shifted narrow lines that do not exchange significant magnetization with each other on the timescale of MRI measurements. This condition likely arises from expected magnetic susceptibility effects (27), a micro-anatomical pore size distribution (previously linked to the pore water T_2 distribution (15)), and the lack of rapid mixing across spatially-disparate pores. Importantly, pore water is inhomogeneously broadened to such an extent that it shares a similar T_2^* with

bound water at high fields (such as in the 4.7T data of (13)). As such, the strongly multi-exponential nature of the cortical bone T_2 spectrum—with separable bound and pore water domains spanning several decades in T_2 —is not preserved in the T_2^* domain, and it will be challenging to quantitatively discriminate bound from pore water using spectroscopic imaging (30,31) or multiple gradient echo schemes adapted to uTE MRI. Straightforward chemical shift-based discrimination is also impractical, given the similarly-broad and spectrally-overlapping bound and pore water lineshapes at high fields—lineshape differences between the two were not readily apparent in a previous study (13). An alternative scheme for pore/bound water discrimination is warranted for clinical and high field cortical bone MRI, and the concept of T_2 -filtering bound from pore water with adiabatic pulses is explored herein.

5.16 — Discussion: Current Bone MRI Methods with Non-selective Imaging

Most cortical bone MRI to date has utilized broad-band excitation pulses and strategies for soft tissue suppression (6-8,32), but imaging results have not been well characterized with regards to bound vs. pore water contributions. BEuTE and CuTE were duplicated herein and did not exhibit significant bound/pore water discrimination. BEuTE's poor discrimination (Fig 5.5B) arises from a mixture of confounds, such as similar bound/pore water T_2^* s which gives rise to

artifactual fitted signal fractions, as well as off-resonance effects from fat and other species that contribute non-monotonic characteristics to the FIDs and disrupt exponential fitting. Although short and long- T_2^* fractions from high field imaging were attributed to bound and free water in (31), the present findings show that such long- T_2^* fractions are clearly not capturing all of the pore water contributions. We anticipate this will become even more problematic as bone imaging moves to higher fields (e.g. the 7T imaging shown in (36)), and further in vivo studies on this point are merited.

Since the CuTE signal includes both bound and pore water contributions, quantitation was performed with the net water T_1 (weighted average of bound and pore water), similar to the approaches taken by (3,6-8). Despite the observed ≈ 2 -fold difference between bound and pore water T_1 s, the CuTE signal agreed well with the net water content, showing a strong linear correlation and minimal bias (Fig 5.6D). Thus, this method is useful for bulk cortical bone water measurements, which supports the findings of other investigators (7).

5.17 — Discussion: AFP Pulses for Bound Water Selection

AFP-CPMG data (Fig 5.4) showed that AFP pulses with bandwidths ≥ 2 kHz created a condition of strongly saturated bound water ($\alpha^{bw} \approx 0.1$) and well-

inverted pore water ($\alpha^{pw} \approx -0.8$), which generates useful contrast between the two pools. For a variety of AFP pulse parameters and bandwidths ≥ 2 kHz, bone water behavior over a broad range of T_2 s followed Bloch equation simulations (Fig 5.2) but was not saturated/inverted as strongly as simulations predicted. This discrepancy may arise from unaccounted relaxation effects (e.g. $T_{1\rho}$) or from magnetization transfer with a semisolid spin pool ($T_2 \approx 10 \mu\text{s}$) that would remain largely unaffected by the AFP pulses herein. However, evaluating such mechanisms is beyond the scope of this study. All AFP pulses with 1 kHz bandwidth still saturated bound water but failed to coherently invert the pore water, which is consistent with the model of homogeneously-broadened bound water and heterogeneously-broadened pore water. Thus, it appears that $\approx 2\text{kHz}$ is the minimum AFP bandwidth (at 4.7T) for effective manipulation of the pore water pool at high fields, and a 3.5 kHz bandwidth was used in the following.

5.18 — Discussion: DAFP for Pore Water-Selective Imaging

Incorporating a broadband DAFP pulse into steady-state imaging was found to strongly saturate bound water and result in a signal dominated by pore water (Fig 5.6B). The assumption that the observed DAFP signal arises entirely from pore water may contribute to overestimation of pore water content (Fig 5.6E),

which is largely a consequence of signal contamination from incompletely saturated bound water and shorter-lived T_{2s} ($\approx 50 \mu\text{s}$) from collagen. However, the bias is not statistically significant and there is a strong correlation ($r^2 = 0.7$) between the DAFP signal and CPMG measures of pore water, even though sample-specific relaxation and AFP efficiency parameters were not included (i.e. population averages were used to scale the signal into proton concentration units). Thus, the DAFP signal is a useful measure of pore water. While no prior information (e.g. R_1 estimates) is needed when planning the DAFP sequence, the high power deposition of the DAFP pulses may limit the TR of the sequence in practice.

5.19 — Discussion: AIR for Bound Water-Selective Imaging

The AIR approach has been successfully shown for general soft tissue suppression in cortical bone MRI (8,32), but its bound/pore water specificity has not been evaluated. Herein, it is shown that signal from an optimized AIR sequence ($TR/TI = 300/90 \text{ ms}$) is dominated by bound water contributions and is largely insensitive to pore water (Fig 5.6C). Sources of bias in the signal quantitation include transverse relaxation during the TE period and magnetization transfer with a semisolids pool during the TI period. However, there was negligible bias, even without sample-specific relaxation or AFP

efficiency correction, as seen by a strong correlation to gold-standard bound water measures ($r^2 = 0.91$, Fig 5.6F). Thus, the AIR signal provides a useful measure of bound water.

The high degree of AIR's bound water selectivity is advantageous, but it requires an estimate of pore water T_1 for optimal IR-nulling. Herein, a single empirically-determined 90 ms TI gave satisfactory pore water nulling across specimens, so a patient-specific estimate of pore water T_1 is not necessary for clinical bound water quantitation. However, since the pore water signal contains a distribution of T_1 s, non-nulled pores with T_1 s shorter and longer than the mean would be placed in anti-phase during bound water signal acquisition. To maintain this state and avoid pore water contamination, the imaging module in AIR should favor minimal echo and acquisition times.

5.20 — Discussion: Correlations to Mechanical Properties

Strong pairwise linear correlations ($r^2 \approx 0.3-0.7$) between various mechanical properties and the AIR and DAPF signals (Fig 5.7) provide a proof of concept that these strategies hold diagnostic relevance for predicting fracture risk.

Importantly, donor-specific measures of bound/pore/net water T_1 , T_2 , and AFP pulse effects are not needed for mechanical property prediction (population averages were used herein) but may further strengthen correlations if available.

The BEuTE fitted signal fractions, which were a poor discriminators of bound/pore water, as well as the CuTE signal, which contains a mixture of both bound and pore water, were not found to have statistically significant correlations to any mechanical property, in agreement with our previous findings (18). In that study, with a three-fold-larger bone specimen population, both bound and pore water had similar mechanical correlation strengths. Herein, DAFP pore water showed considerably stronger mechanical correlations than AIR bound water, but the high correlation between the AIR-signal and equilibrium CPMG-derived bound water measures implies that stronger AIR/mechanical property correlations could emerge in a larger population. Additionally, there is likely to be an optimal imaging TE, since $TE \ll 50 \mu s$ would introduce matrix-related signals ($T_2 \approx 10 \mu s$, (11,13,17)) that confound pore water estimation, and $TE \gg 50 \mu s$ enhances bound/pore water $T_2^{(*)}$ weighting that may vary across bones in a manner not correlated with mechanical properties.

Finally, we note the possibility of combining two of the CuTE/AIR/DAFP measurements to determine a third water measurement. This follows the premise that $M_o^{net} = M_o^{bw} + M_o^{pw}$, where M_o^{net} is determined from CuTE and M_o^{bw} and M_o^{pw} are determined from AIR and DAFP, respectively. For example, the AIR sequence's maximum temporal signal-to-noise ratio efficiency, ($\propto S_{AIR}/\sqrt{TR}$),

occurs at $TR \approx 500$ ms and $\theta \approx 90^\circ$ for practical AFP and tissue characteristics ($\alpha^{bw} = 0.1$, $\alpha^{pw} = -0.85$, $R_1^{bw} = 2.9$ Hz, $R_1^{pw} = 1.9$ Hz). Such a long TR may be acceptable for 2D imaging, but 3D imaging may require impractically long scan times unless MP-RAGE (37) or similar acquisition schemes are employed to collect several lines of k-space during each TR . However, bound water information can alternately be synthesized from two separate CuTE and DAFP scans in perhaps less time.

Additionally, as an alternative to DAFP, we note that a spin echo measurement with a minimal (≈ 10 ms) echo time can, in principle, be used to selectively image the long- T_2 pore water while allowing sufficient time for complete bound water T_2 decay, but the broad bandwidths needed to refocus the pore water spins will test the limits of clinical MRI (e.g. peak $|B_1|$ and specific absorption rate safeguards).

5.21 – Conclusions

In summary, bound and pore water NMR signals in cortical bone follow homogeneously and inhomogeneously broadened transverse relaxation mechanisms, respectively. Bound and pore water-specific NMR spectra exhibit similar and overlapping lineshapes, so discriminating the two in commonly-used

T_2^* and chemical shift domains is challenging at high fields. We present alternate, T_2 -filter-based strategies for isolating bound or pore water signals for uTE MRI. A pulse sequence (AIR) combining the T_2 -selectivity of an AFP pulse and the T_1 -selectivity of an inversion-recovery filter is demonstrated for quantitative bound water imaging, and a double-AFP sequence (DAFP) is shown as a means for quantitative pore water imaging. Both methods achieve a high degree of bound/pore water selectivity while utilizing clinically-relevant RF pulse parameters. The resulting signals have strong correlation to important bone mechanical properties, which was not found to be the case for current bone imaging methods (BEuTE/CuTE). Since patient-specific measures of T_1 and T_2 (i.e. AFP pulse effects) are not needed, it should be practical to obtain *in vivo* bound and pore water maps of cortical bone with the proposed methods, which may be used to assess bone fracture risk.

5.22 — References

1. Robson MD, Gatehouse PD, Bydder M, Bydder GM. Magnetic resonance: An introduction to ultrashort TE (UTE) imaging. *J Comput Assist Tomogr* 2003;27(6): 825-846.
2. Idiyatullin D, Corum C, Park J, Garwood M. Fast and quiet MRI using a swept radiofrequency. *Journal of Magnetic Resonance* 2006;181(2):342-349.
3. Wu Y, Ackerman J, Chesler D, Graham L, Wang Y, Glimcher M. Density of organic matrix of native mineralized bone measured by water- and fat-

- suppressed proton projection MRI. *Magnetic Resonance in Medicine* 2003;50(1):59-68.
4. Balcom B, MacGregor R, Beyea S, Green D, Armstrong R, Bremner T. Single-point ramped imaging with T-1 enhancement (SPRITE). *Journal of Magnetic Resonance Series A* 1996;123(1):131-134.
 5. Du J, Takahashi AM, Chung CB. Ultrashort TE Spectroscopic Imaging (UTESI): Application to the Imaging of Short T2 Relaxation Tissues in the Musculoskeletal System. *Journal of Magnetic Resonance Imaging* 2009;29(2):412-421.
 6. Techawiboonwong A, Song H, Leonard M, Wehrli F. Cortical bone water: In vivo quantification with ultrashort echo-time MR imaging. *Radiology* 2008;248(3):824-833.
 7. Rad HS, Lam SCB, Magland JF, Ong H, Li C, Song HK, Love J, Wehrli FW. Quantifying cortical bone water in vivo by three-dimensional ultra-short echo-time MRI. *NMR Biomed* 2011;n/a-n/a.
 8. Du J, Carl M, Bydder M, Takahashi A, Chung CB, Bydder GM. Qualitative and quantitative ultrashort echo time (UTE) imaging of cortical bone. *J Magn Reson* 2010;207(2):304-311.
 9. Springer F, Martirosian P, Machann J, Schwenzer N, Claussen C, Schick F. Magnetization Transfer Contrast Imaging in Bovine and Human Cortical Bone Applying an Ultrashort Echo Time Sequence at 3 Tesla. *Magnetic Resonance in Medicine* 2009;61(5):1040-1048.
 10. Ni Q, Nicolella D. The characterization of human cortical bone microdamage by nuclear magnetic resonance. *Meas Sci Technol* 2005;16(3):659-668.
 11. Nyman J, Ni Q, Nicolella D, Wang X. Measurements of mobile and bound water by nuclear magnetic resonance correlate with mechanical properties of bone. *Bone* 2008;42(1):193-199.
 12. Fernandez-Seara M, Wehrli S, Takahashi M, Wehrli F. Water content measured by proton-deuteron exchange NMR predicts bone mineral density and mechanical properties. *J Bone Miner Res* 2004;19(2):289-296.
 13. Horch R, Nyman J, Gochberg D, Dortch R, DOES M. Characterization of ^1H NMR signal in human cortical bone for magnetic resonance imaging. *Magnetic Resonance in Medicine* 2010;64(3):680-687.

14. Fantazzini P, Brown R, Borgia G. Bone tissue and porous media: common features and differences studied by NMR relaxation. *Magn Reson Imaging* 2003;21(3-4):227-234.
15. Ni Q, King J, Wang X. The characterization of human compact bone structure changes by low-field nuclear magnetic resonance. *Measurement Science & Technology* 2004;15(1):58-66.
16. Wang X, Ni Q. Determination of cortical bone porosity and pore size distribution using a low field pulsed NMR approach. *J Orthop Res* 2003;21(2):312-319.
17. Ni Q, Nyman J, Wang X, De Los Santos A, Nicolella D. Assessment of water distribution changes in human cortical bone by nuclear magnetic resonance. *Meas Sci Technol* 2007;18(3):715-723.
18. Horch RA, Gochberg DF, Nyman JS, Does MD. Non-invasive Predictors of Human Cortical Bone Mechanical Properties: T-2-Discriminated H-1 NMR Compared with High Resolution X-ray. *PLoS ONE* 2011;6(1):e16359.
19. Carl M, Bydder M, Du J, Takahashi A, Han E. Optimization of RF excitation to maximize signal and T2 contrast of tissues with rapid transverse relaxation. *Magnetic resonance in medicine : official journal of the Society of Magnetic Resonance in Medicine / Society of Magnetic Resonance in Medicine* 2010;64(2):481-490.
20. Josan S, Pauly JM, Daniel BL, Pauly KB. Double Half RF Pulses for Reduced Sensitivity to Eddy Currents in UTE Imaging. *Magnetic resonance in medicine : official journal of the Society of Magnetic Resonance in Medicine / Society of Magnetic Resonance in Medicine* 2009;61(5):1083-1089.
21. Larson PEZ, Gurney PT, Nayak K, Gold GE, Pauly JM, Nishimura DG. Designing long-T-2 suppression pulses for ultrashort echo time imaging. *Magnetic resonance in medicine : official journal of the Society of Magnetic Resonance in Medicine / Society of Magnetic Resonance in Medicine* 2006;56(1):94-103.
22. Larson PEZ, Conolly SM, Pauly JM, Nishimura DG. Using adiabatic inversion pulses for long-T-2 suppression in ultrashort echo time (UTE) imaging. *Magnetic resonance in medicine : official journal of the Society of Magnetic Resonance in Medicine / Society of Magnetic Resonance in Medicine* 2007;58(5):952-961.
23. Sussman M, Pauly J, Wright G. Design of practical T-2-selective RF excitation (TELEX) pulses. *Magnetic resonance in medicine : official journal of the Society of Magnetic Resonance in Medicine / Society of Magnetic Resonance in Medicine* 1998;40(6):890-899.

24. Silver M, Joseph R, Hoult D. Highly selective $\pi/2$ and π pulse generation. *Journal of Magnetic Resonance* 1984;59(2):347-351.
25. Norris D, Ludemann H, Leibfritz D. An Analysis of the Effects of Short T2 Values on the Hyperbolic-Secant Pulse. *Journal of Magnetic Resonance* 1991;92(1): 94-101.
26. Cowin S. Bone poroelasticity. *Journal of Biomechanics* 1999;32(3):217-238.
27. Hopkins J, Wehrli F. Magnetic susceptibility measurement of insoluble solids by NMR: Magnetic susceptibility of bone. *Magnetic Resonance in Medicine* 1997;37(4):494-500.
28. Wehrli F, Fernandez-Seara M. Nuclear magnetic resonance studies of bone water. *Ann Biomed Eng* 2005;33(1):79-86.
29. Bull T. Relaxation in the rotating frame in liquids. *Progress in Nuclear Magnetic Resonance Spectroscopy* 1992;24:377-410.
30. Du J, Hamilton G, Takahashi A, Bydder M, Chung C. Ultrashort echo time spectroscopic imaging (UTESI) of cortical bone. *Magnetic resonance in medicine : official journal of the Society of Magnetic Resonance in Medicine / Society of Magnetic Resonance in Medicine* 2007;58(5):1001-1009.
31. Diaz E, Chung C, Bae W, Statum S. Ultrashort echo time spectroscopic imaging (UTESI): an efficient method for quantifying bound and free water. *NMR in ...* 2011.
32. Du J, Takahashi AM, Bae WC, Chung CB, Bydder GM. Dual Inversion Recovery, Ultrashort Echo Time (DIR UTE) Imaging: Creating High Contrast for Short-T2 Species. *Magnetic Resonance in Medicine* 2010;63(2):447-455.
33. Horch RA, Wilkens K, Gochberg DF, Does MD. RF coil considerations for short-T2 MRI. *Magn Reson Med* 2010;64(6):1652-1657.
34. Tannus A, Garwood M. Improved performance of frequency-swept pulses using offset-independent adiabaticity. *Journal of Magnetic Resonance Series A* 1996;120(1):133-137.
35. Fernandez-Seara M, Wehrli S, Wehrli F. Diffusion of exchangeable water in cortical bone studied by nuclear magnetic resonance. *Biophysical Journal* 2002;82(1):522-529.
36. Krug R, Larson PEZ, Wang C, Burghardt AJ, Kelley DAC, Link TM, Zhang X, Vigneron DB, Majumdar S. Ultrashort echo time MRI of cortical bone at 7 tesla

field strength: A feasibility study. *Journal of Magnetic Resonance Imaging* 2011;34(3):691-695.

37. Haase A. Snapshot FLASH MRI. Applications to T1, T2, and Chemical-Shift Imaging. *Magnet Reson Med* 1990;13(1):77-89.

CHAPTER 6

The Future of Cortical Bone Magnetic Resonance

The work shown in previous chapters established a biophysical basis for diagnostic bone MRI. The micro-anatomical origins of bone NMR signal components were first identified, followed by a demonstration of their ability to predict bone mechanical integrity. Finally, practical methods were developed for performing bone MRI in the clinic while preserving the ability to predict bone mechanical response—showing potential for diagnostic utility. This work, and resulting conclusions, were based on studies using bulk measurements from bone localized to a portion of the femoral cortex. One obvious step going forward is to extend this work to whole bone fracture studies, and there are other avenues to explore such as monitoring the progression of diseases and therapies with MRI measures of bone matrix composition. These future directions are discussed below, and considerations are given as to the practicality of bone MRI in clinical or point-of-care settings. Afterwards, this dissertation concludes with some final thoughts.

6.1 — Whole Bone Fracture Assessment

One ultimate goal of MRI-based whole bone fracture assessment would be for clinicians to determine, with a high probability, whether or not a patient's typical unbraced fall would result in fracture. With such fracture risk information, patient lifestyle could be updated accordingly and clinicians could tailor drug therapies to address MRI-derived fracture risk. As a second goal, the fracture risk prognosis could be improved via MRI scan-rescan protocols carried out over periods of months to years. In this way, clinicians could monitor the progression of bone properties over time to establish a fracture risk trajectory, thereby estimating at what point fracture risk would reach thresholds for clinical intervention. To realize these and other goals, a framework needs to be developed for translating whole-bone MRI data into a measure of whole bone fracture risk.

One envisioning of a framework for MRI-based whole bone fracture assessment involves coupling volumetric MRI data to finite element mesh (FEM) mechanical modeling. Mechanical FEM modeling is fundamentally a method of numerical integration, which determines the stresses and strains distributed throughout a mechanical member once its surface boundary conditions, geometry, and material properties are known (1). FEM methods have been

applied previously to CT-based bone image sets (2-4), demonstrating improved fracture risk prediction as compared to bulk measures such as DXA. While these methods construct meshes for finite element modeling from CT-determined bone geometry, the individual mechanical properties of each mesh element are assumed to be identical or, in the best case scenario, are derived from X-ray-based BMD measures. By way of its stronger mechanical property correlations, bone MRI offers an added degree of refinement by providing inputs for FEM methods as follows: 1) bone geometry, which can be determined from the volumetric MRI dataset by thresholding or spatial segmentation methods of identifying bone-containing image pixels (5); and 2) spatially-resolved bone mechanical properties, which can be determined by translating bone water measures from the AIR and/or DAFP MRI methods into relevant mechanical properties (via population-based relationships determined *a priori*, such as those shown in Chapters 5 & 6). In this way, both mesh geometry and individual mesh element mechanical properties can be generated from bone MRI, and the resulting FEM model can be evaluated *in silico* to determine responses to simulated mechanical insults consistent with falling or high-impact activities. Monte Carlo or other statistical approaches can be utilized to provide clinicians

with patient-specific measures of fracture risk from this MRI-driven FEM modeling.

By leveraging the well-developed field of FEM biomechanical modeling, MRI-driven fracture assessment should be relatively straightforward to develop and should be more informative than X-ray-based fracture assessment, owing to MRI's higher sensitivity to bone mechanical properties. If whole-bone modeling proves impractical because of MRI field-of-view or scan time limitations, site-specific fracture risk assessment could be conducted on common fracture locations such as the femoral head, ankle, wrist, or collar bone. Given the robustness of the FEM method and the clinical feasibility of mechanically-predictive bone MRI, MRI-driven FEM has potential as a clinical tool for practical, patient-specific whole bone fracture risk assessment.

6.2 — Bone Matrix MRI: Going Beyond Mechanical Properties

Thus far, bone MRI has been evaluated in the context of mechanical property prediction. However, as a compositional measure, bone MRI has other applications such as the evaluation of disease states, where assessing the physiological status of bone would be useful for diagnosis or to monitor treatment response. For example, monitoring bone collagen and bound/pore water composition could potentially provide sensitivity to: A) the increased

collagen crosslink density that occurs with diabetes and aging (Chapter 1.3); B) the collagen structural anomalies that occur in altered phenotypes like OI (also Chapter 1.3); C) the osteolytic perturbations to bone matrix that occur when bone cancers upset the bone formation/resorption balance (6); D) the physiological responses to therapies such as remineralization secondary to bisphosphonate drug regimens (7) or defect repair secondary to biomimetic bone scaffold implantation (8); E) the cascade of processes involved in fracture healing (9); and F) basic functional physiology such as the fluid redistribution mechanics thought to occur during dynamic bone loading (10,11). Bulk measures of collagen content or bound/pore water may be useful for each of these applications, but it is possible to provide more specific measures of bone composition with another level of refinement, dubbed bone matrix MRI.

The goal of bone matrix MRI is to generate quantitative measures of bone matrix volume and constituent concentrations (i.e. matrix constituent quantities relative to matrix volume). This approach offers an added degree of specificity to physiological changes accompanying the previously mentioned diseases and therapies. For example, a hypothetical increase in bone matrix volume caused by up-regulation of normal bone formation could result in elevated amounts of matrix water, collagen, and minerals, such that bulk measures of these

constituents (relative to overall bone volume) would be increased even though their concentrations in the matrix remain unchanged. Conversely, hypermineralization could cause an increase in matrix volume with negligible or relatively small increases in bulk matrix water and collagen, as the matrix concentration of the mineral phase is increased relative to those of water and collagen. Thus, bone matrix MRI is potentially more sensitive to physiological changes than bulk MRI measures of collagen and water, however a good estimate of bone matrix volume is essential to this approach.

Since cortical bone volume is the sum of matrix and pore volumes, bone matrix volume can be estimated by subtracting a measure of the total pore space volume from the total bone volume (e.g. as determined voxel-wise from DAFP pore water images of known resolution). The proton density of the pore spaces is needed to convert quantitative DAFP pore water amount to total pore volume, and it may be sufficient either to assume this density is relatively constant across patients or to estimate this density from the blood pool's proton density on a patient-specific basis (since the pore space is well vascularized). Bound water matrix concentration can be determined by normalizing quantitative AIR MRI measurements to the bone matrix volume, since the AIR signal is assumed to predominantly arise from matrix water. More development is necessary to

generate quantitative measures of the collagen phase, but uTE methods strongly sensitive to bone collagen's 10-50 μ s T_2 range (such as SWIFT (12)) have the potential to do so and can be likewise normalized to measure collagen concentration in the matrix. Finally, mineral concentration in the matrix volume can be inferred once matrix volume and both water and collagen concentrations are known, or quantitative BMD measures can be utilized, such as those from QCT or the emerging field of mineral-specific ^{31}P MRI (13,14). Although further study and validation is needed, bone matrix MRI may find use as a research tool or in the clinic, if matrix concentration measures prove to be diagnostically informative.

6.3 — Requirements for Practical Cortical Bone MRI in the Clinic

With MRI in widespread use today, the infrastructure is largely in place for clinical bone MRI. However, the question remains as to how much practical value bone MRI adds to clinical diagnosis, given the relatively high costs of MRI compared to other imaging modalities. It is unlikely that clinical bone MRI will ever become as inexpensive as DXA or plain film X-ray measurements, although it is conceivable that bench-top or small-scale boutique MRI scanners for peripheral scanning (wrist, ankle, etc.) could drive down bone MRI costs considerably. Regardless, by way of their low cost and widespread use, point-of-

care DXA machines and similar devices will provide competition to novel MRI methods for some time to come. Ultimately, to be successful, bone MRI needs to provide sufficient diagnostic value so as to outweigh its added costs. The work presented in the preceding chapters provides evidence of this diagnostic value, as bone MRI was shown to offer more compositional measures and stronger mechanical property prediction than X-rays. While this may be a promising first step, what is ultimately needed is large-scale clinical studies of bone MRI in the context of whole bone fracture assessment or specific diseases and therapies. Demonstration of diagnostic utility in this manner is a key requirement to garnering widespread, practical bone MRI in the clinic.

Other requirements for practical bone MRI include: the widespread adoption of non-cartesian image reconstruction hardware/software, as bone uTE MRI methods thus far use radial sampling strategies almost exclusively; the use of quantitative phantoms/markers placed within the bone imaging field of view, which would likely be packaged similarly to the current clinical MRI fiducial markers and consist of $D_2O/H_2O/CuSO_4$ formulations with known proton density and relaxation characteristics; and ideally (but not necessarily) a low- 1H MRI hardware environment, which could consist of hot-swappable PTFE-formed

RF coils and shield inserts if necessary. These requirements are relatively modest and should not present significant barriers to clinical bone MRI.

6.4 – *Final Thoughts*

In a word, the future of bone MRI is one of potential. Given that bone MRI is still in a relatively nascent state, there is potential for improving our knowledge of fundamental physiology, the processes of disease and aging, and the effects of therapeutic strategies. This potential arises from the capabilities of the bone MRI toolset, which is now a platform capable of making quantitative compositional measures *in vivo* with micro-anatomical specificity. A new paradigm is now available for the study of bone, since these types of *in vivo* measures were not available prior to the studies herein and recent work from other researchers. Furthermore, cortical bone is an ideally robust tissue that favors *ex vivo* experimentation: it can withstand numerous freeze-thaw cycles and long-term frozen storage, it is readily machinable and can be powderized to conform to different laboratory tests (NMR, mechanical, chemical, etc.), and it can be subjected to sterilization procedures if necessary (e.g. γ -irradiation). With the modern MRI toolset in place and bone's favorable properties, it is this author's opinion that an exciting future awaits bone researchers.

Additionally, it is worthwhile to note that the methods applied to characterize human cortical bone herein have broad utility. Transverse relaxation spectroscopy, D₂O-based isotopic manipulation, and measures of composition and chemical exchange are all methods readily compatible with a variety of tissue types. An example of applying these methods to biological sources of myelin is shown in Appendix III, in which the biophysical basis for a new myelin imaging biomarker is presented.

Finally, this work concludes on a note of reverence. Since bones are often our only earthly remains to withstand the tests of time, there is perhaps a certain poetry or mystique within the labors of bone research: just as studying our forebears' ancient bones has told us much about our past, studying our living bones with novel imaging tools has promise to tell us much of our future.

6.5 — *References*

1. Lynch DR. Numerical partial differential equations for environmental scientists and engineers: Springer Verlag; 2005. 388 p.
2. Cody D, Gross G, Hou F, Spencer H, Goldstein S, Fyhrie D. Femoral strength is better predicted by finite element models than QCT and DXA. *Journal of Biomechanics* 1999;32:1013-1020.
3. Yosibash Z, Trabelsi N, Milgrom C. Reliable simulations of the human proximal femur by high-order finite element analysis validated by experimental observations. *Journal of Biomechanics* 2007;40(16):3688-3699.

4. Schileo E, Taddei F, Malandrino A, Cristofolini L, Viceconti M. Subject-specific finite element models can accurately predict strain levels in long bones. *Journal of Biomechanics* 2007;40(13):2982-2989.
5. Rad HS, Lam SCB, Magland JF, Ong H, Li C, Song HK, Love J, Wehrli FW. Quantifying cortical bone water in vivo by three-dimensional ultra-short echo-time MRI. *NMR in Biomedicine* 2011;24(7):855-864.
6. Terpos E. Biochemical markers of bone metabolism in multiple myeloma. *Cancer Treatment Reviews* 2006;32(S1):15-19.
7. Body JJ, Mancini I. Bisphosphonates for cancer patients: why, how, and when? *Supportive Care in Cancer* 2001;10(5):399-407.
8. Petite H, Viateau V, Bensaid W, Meunier A. Tissue-engineered bone regeneration. *Nature* 2000;18:959-963.
9. Dimitriou R, Tsiridis E, Giannoudis PV. Current concepts of molecular aspects of bone healing. *Injury* 2005;36(12):1392-1404.
10. Wang L, Wang Y, Han Y, Henderson S, Majeska R, Weinbaum S, Schaffler M. In situ measurement of solute transport in the bone lacunar-canalicular system. *PNAS* 2005;102(33):11911-11916.
11. Malachanne E, Dureisseix D, Canadas P, Jourdan F. Experimental and numerical identification of cortical bone permeability. *Journal of Biomechanics* 2008;41(3):721-725.
12. Idiyatullin D, Corum C, Park J, Garwood M. Fast and quiet MRI using a swept radiofrequency. *Journal of Magnetic Resonance* 2006;181(2):342-349.
13. Wu Y, Ackerman J, Chesler D, Li J. Evaluation of bone mineral density using three-dimensional solid state phosphorus-31 NMR projection imaging. *Calcif Tissue Int* 1998;62:512-518.
14. Wu Y, Reese TG, Cao H, Hrovat MI, Toddes SP, Lemdiasov RA, Ackerman JL. Bone mineral imaged in vivo by 31P solid state MRI of human wrists. *Journal of Magnetic Resonance Imaging* 2011;34(3):623-633.

APPENDIX I

Experiences with High Power Loop-gap RF Coil Design and Bench Testing

The bone spectroscopy presented in previous chapters was performed on low- ^1H loop-gap coils at 200 MHz. Commercial versions of these coils were prohibitively expensive, and metrics such as coil ^1H background signal size were not available from the vendors. Thus, in-house coils were purpose-built, and the design and material selection processes were outlined in Chapter 2. This appendix expands on Chapter 2 and presents a number of practical points noted during coil development. Hopefully these points will be of assistance to other non-RF engineers like the author who need to design and bench test boutique NMR coils. For the interested reader, accessible discussions of related RF electronics theory can be found in the early chapters of (1).

AI.1 – Coil Selection and Design

The loop-gap resonator design was chosen for bone studies because of its uniform B_1 field throughout the middle third of the coil's height (2) and because of its low internal electric field, which minimized sample heating (3) and allowed high power and duty cycle RF pulses for short CPMG echo spacing. Figure AI.1

shows a schematic and circuit layout of a 20 mm diameter loop-gap coil that operates at 200 MHz, which serves as the platform for discussions below.

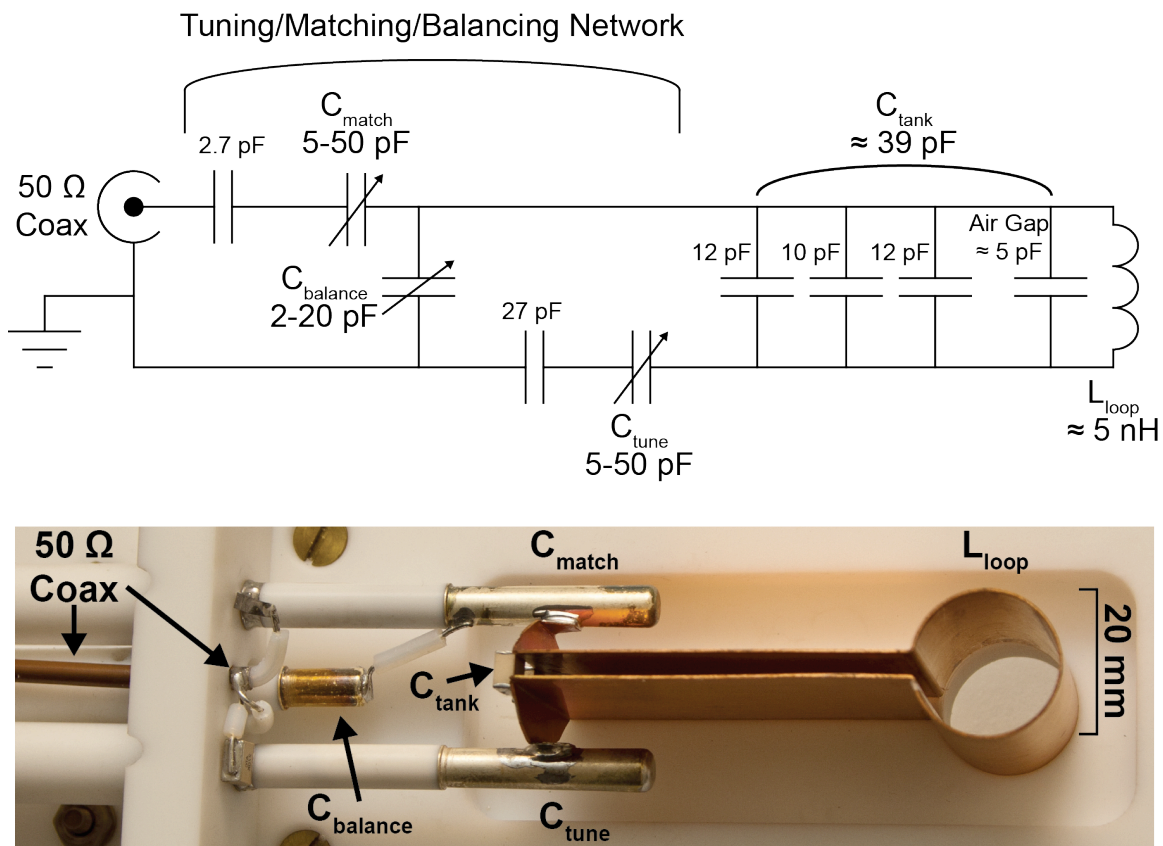


FIGURE AI.1 200 MHz loop-gap probehead schematic (top) and component layout (bottom).

Circuit design was based on a versatile, capacitive tuning/matching/balancing network commonly used in high power probeheads, e.g. the proton channel of (4) and the design in section 4.5.2 of (1) (notable typo: there is an omitted capacitor in a ground leg of this reference's Fig 4.9). Physical circuit layout was chosen such that the coil was optimized for high power: lead wires and tuning/matching/balancing trimmer capacitors were spaced far enough apart

to avoid arcing at high voltages, and tank (primary resonator) capacitance was distributed across several chip capacitors to reduce current flows and heating within individual components. The large body of copper in the loop-gap resonator also doubled as a heatsink for the tank capacitors (but was also a source of undesirable eddy currents during imaging experiments). ATC (American Technical Ceramics) 700B/C-series chip capacitors were useful for fixed capacitances, as they were non-magnetic, did not drift with temperature change as much as Voltronics and assorted in-house chip capacitors, and had high Qs (Q = quality factor, a measure of loss defined as energy stored divided by energy dissipated). Teflon trimmer capacitors from Polyflon were used here, but quartz-dielectric versions from Voltronics were adopted in later designs because they better withstood inadvertent overvoltages (leading to dielectric breakdown and tuning instability under load via internal arcing). In practice, large trimmer capacitance ranges were desirable to facilitate the initial search for the coil's main resonance mode, after which chip capacitors of appropriate values were added in series to scale down trimmer effects on the main resonance (improved tuning rod usability) and to reduce voltages across the trimmers.

AI.2 — Tuning, Matching, and Balancing on the Bench-top

Once a coil is assembled, the challenge remains to find a “solution” (i.e. set of trimmer capacitance values) for a tuned, matched, and balanced state at the desired resonant frequency. The tuning capacitance adjusts the main loop-gap resonance to match the desired NMR frequency. Matching adjusts the impedance of the coil to that of the coaxial transmission line and RF amplifier (50 ohms), such that there is negligible capacitive or inductive load at the probehead port and maximum power transmission to the coil (and maximum NMR signal returned from the coil). Balancing is a symmetrizing process which places currents through the coaxial transmission line outer shield and inner conductor into antiphase; as a result, there is no net current in the transmission line of the perfectly balanced probehead and, consequently, minimal radiative losses.

Balancing was frequently overlooked during in-house coil fabrication prior to this work but is arguably just as important as tuning and matching. A poorly balanced probehead will act as an RF radiator, because current-carrying coaxial transmission lines effectively become broadcast antennas. In this case, the coil’s tuning and matching become sensitive to capacitances and inductances in the near field of the transmission lines, such as human operators attempting to tune and match the coil (who can then upset the tune/match simply by moving

around!). Importantly, radiative losses can degrade coil performance: the Q-factor of the balanced probehead in Fig AI.1 was improved approximately 5-fold over prior, unbalanced in-house designs. Since NMR signal-to-noise ratio is proportional to \sqrt{Q} , (1), proper balancing can translate into considerable sensitivity benefits. For further discussion of balancing, refer to Chapter 4 in (1).

Tuning, matching, and balancing are accomplished on a network analyzer, preferably with the setup shown in Fig AI.2. Port 1 of the network analyzer is connected to the coil with coaxial cable (transmission line); an in-line choke or filter should *not* be used at this stage so undesirable cable currents are not attenuated. Port 2 is connected to an electric field probe, which is clamped around Port 1's cable for sensitivity to cable currents; this probe is a magnetically-shielded, broadband pickup coil and thus is ideally suited for cable current monitoring. Finally, port 3 is connected to a hand-held search wand, which is an electrically-shielded, broadband pickup predominantly sensitive to magnetic flux. The search wand is not strictly necessary, but it is useful for initial coil setup described below and for localizing any stray resonances; also, it can also double as a cable current monitor if held adjacent to the transmission line with its axis perpendicular to the line (so as to pick up the conservative magnetic field flux from cable currents). Network analyzer scattering parameters used in this setup

are: S11 (to measure power reflections from the coil), S12 (to measure cable currents), and S13 (to pick up coil emissions with the search wand). A scattering parameter S_{ij} provides frequency-resolved measures of power received at port j after being transmitted from port i . Thus, S11 is a reflection measure.

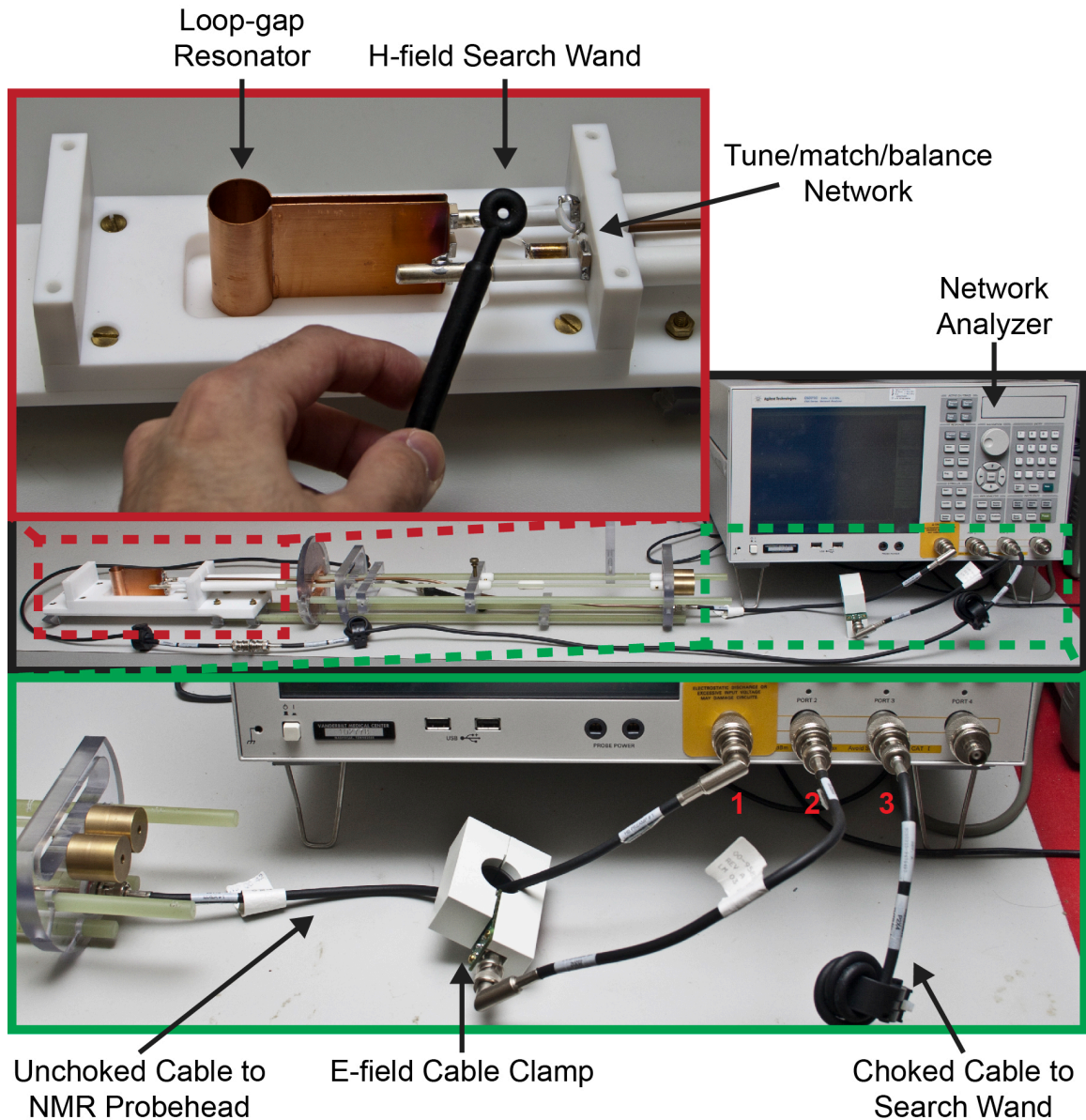


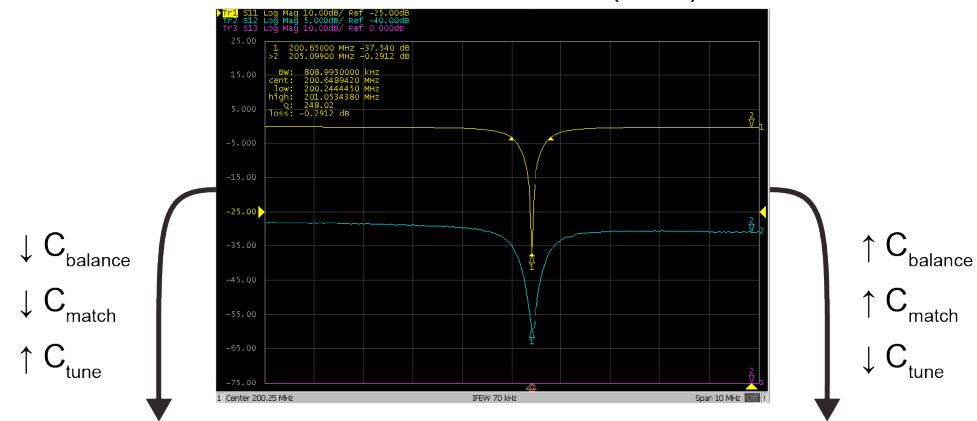
FIGURE AI.2 *Bench-top setup for probehead testing with a 4-port network analyzer. Overall setup is shown at middle, with search wand use at top and connection details at bottom insets (network analyzer port numbers are labeled in red). It is important to have a clean, non-conductive bench free of excess cabling to avoid confounding stray couplings.*

The first step of initial coil setup is to identify the main coil resonance. Resonance may not be obvious in the S11 readout trace if the coil is not matched, as it will reflect power comparably across a broad bandwidth. In this case, the search wand can be positioned axially over the loop to pick up its resonance in the S13 trace; alternately, two search wands can be used (if available) with one as a transmitter, one as a receiver, and the loop-gap resonator placed in between. Once the main resonance is identified, the tuning trimmer capacitor should be adjusted to bring the resonance to the vicinity of the target NMR frequency. The matching capacitor should then be adjusted to provide a visible absorbance band in the S11 trace (if not already present). Finally, the balancing capacitor should be adjusted to minimize cable currents at the coil's resonant frequency in the S12 trace. Since the tuning and balancing capacitors are placed in electrical symmetry on the legs of the loop-gap, they will need to be counter-rotated to maintain a stationary resonance frequency. While adjusting tuning and balancing capacitors, the matching capacitor should be occasionally adjusted to maintain a visible absorbance peak on the S11 trace. This is an iterative 3-parameter optimization process, whereby the tune/match/balance capacitances are modulated until the coil is properly matched and balanced at the desired frequency (i.e. a solution is found). The optimization is somewhat simplified by the circuit design in Fig AI.1,

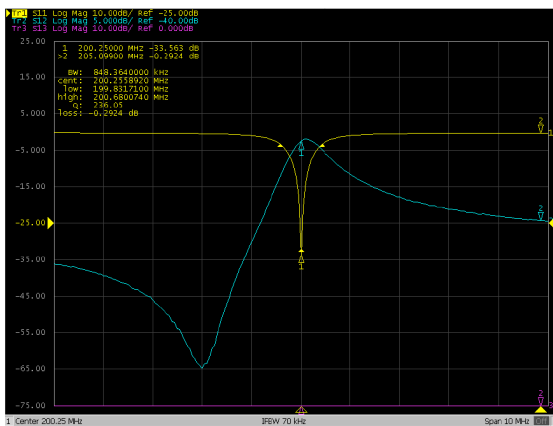
in which the matching capacitor does not strongly alter coil tuning (as it may in other types of coils and circuit designs).

Figure AI.3 shows traces from balanced and mildly unbalanced solutions. In practice, S11 trace values below -30 dBm at resonance are indicative of a good match (for 1 dBm of input power, translates to less than 0.1% of incoming power reflected by the coil and thus 99.9% of power reaching the probehead), and a Smith chart display can be used to check that coil impedance is purely resistive. A symmetric S12 trace with peak absorption (trace minimum) at the coil resonance frequency coincides with proper balancing, and the shape of the S12 trace indicates whether balancing capacitance needs to be increased or decreased (as shown in Fig AI.3). For a physically symmetrical circuit layout (as in Fig AI.1), balancing also coincides with the formation of a virtual ground at the midpoint of the loop, opposite the gap (3). Thus, balance can be checked alternatively by touching the tip of a grounded lead to this point on the resonator: if the coil is balanced, the shape of the S11 trace will not change as no significant energy is lost from the resonator; if the coil is unbalanced, the position of the virtual ground can be found by probing different points on the resonator, and the balance can be adjusted until this point shifts to the middle of the loop.

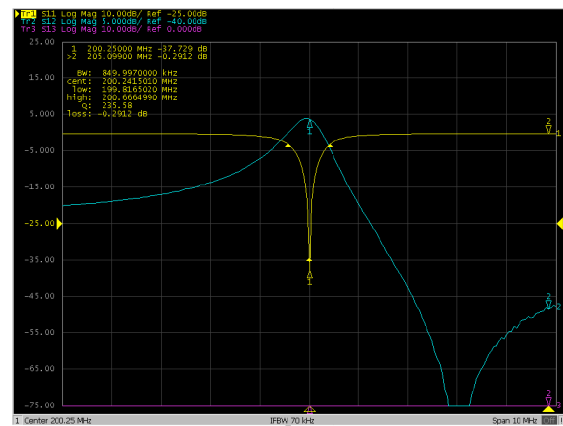
Balanced Probehead (Ideal)



Underbalanced Probehead



Overbalanced Probehead



↑ Cable Currents
 ↓ Q-factor
 ↓ Tuning Stability

FIGURE AI.3 Network analyzer traces from the 20mm, 200.25 MHz loop-gap for tuning, matching, and balancing. S11 (coil reflectance) and S12 (cable currents) traces are shown in yellow and blue, respectively, for a properly balanced state (top) and under- or overbalanced states (middle). Adequate matching was achieved in all cases. Proper balancing gives a minimum in S12 at the coil resonance frequency. Relative to this state, an underbalanced condition is created (left) by decreasing the balancing capacitance ($C_{balance}$) while decreasing the matching (C_{match}) and increasing the tuning (C_{tune}) capacitances to maintain resonance frequency and impedance matching. Reciprocal capacitance changes create an overbalanced condition (right). The antisymmetric S12 trace shapes (middle left/right) transition to the symmetric shape (top) as balance is restored, providing a clue as to which direction the balance capacitor should be adjusted. Consequences of poor balancing are shown at bottom. Note that these are mildly under/overbalanced states; extreme cases result in a dramatic Q decrease and broader S12 antisymmetric shapes. (Top traces have ≈ 400 kHz of inadvertent detuning.)

The low electric field flux in the homogenous region of the loop-gap (middle third of axial height) results in poor coupling to dielectric samples contained in this region. Consequently, the coil tuning/matching/balancing solution is relatively insensitive to these sample loads, and balancing only needs to be performed once on the bench. In practice, only small adjustments to the tune and match capacitors are necessary as samples are exchanged between NMR measurements, and common users should not adjust the balancing capacitance unless a multiport network analyzer is available. Note that the in-house, yellow “Morris Sweeper” tuning box is a one-port scalar network analyzer that gives an S11 trace and is not sufficient for balancing via the cable current monitoring method. However, it could be used for balancing with the virtual ground point method.

AI.3 – Final Checks

Once the coil is completely set up on the bench and tuned/matched/balanced, it is worthwhile to check for faulty solder joints or loose connections. A simple, brute-force way of doing this consists of monitoring the S11 trace while tapping on various coil components with a long, insulated prod (so hands are kept far enough away from the coil to minimize capacitive coupling). Alternately, the

whole coil can be gently knocked with a palm or knuckle, simulating vibrations from imaging gradients. Also, transmission lines should be jiggled, and tuning rods should be wobbled. (This is affectionately called the “Ken Wilkens” procedure). Loose connections will manifest as momentary blips or jagged transients in the S11 trace, and capacitor instability will result in a permanent drift of coil resonance that requires retuning. Any transient effects in S11 should be immediately investigated, as the coil may exhibit considerable B_1 magnitude or phase instability during NMR measurements in the presence of vibrations. It is much less frustrating to find problems at the RF bench than once the coil is in the magnet and the NMR experiment is set up or running!

AI.4 – References

1. Mispelter J, Lupu M, Briguet A. NMR Probeheads for Biophysical and Biomedical Experiments: Theoretical Principles & Practical Guidelines. London: Imperial College Press; 2006. 596 p.
2. Mispelter J, Lupu M. Homogeneous resonators for magnetic resonance: A review. *Comptes Rendus Chimie* 2008;11(4-5):340-355.
3. Gor’Kov P, Chekmenev E, Li C, Cotten M, Buffy J, Traaseth N, Veglia G, Brey W. Using low-E resonators to reduce RF heating in biological samples for static solid-state NMR up to 900 MHz. *J Magn Reson* 2007;185(1):77-93.
4. Gor’Kov P, Witter R, Chekmenev E, Nozirov F, Fu R, Brey W. Low-E probe for ^{19}F - ^1H NMR of dilute biological solids. *Journal of Magnetic Resonance* 2007;189(2):182-189.

APPENDIX II

Considerations for Processing Human Cortical Bone Tissue

It is of utmost importance to follow proper biosafety protocols when handling human bone tissue, especially when cutting or machining cortical bone. Bone dust is not only a respiratory tract irritant, it is an airborne vector for disease transmission. Thus, a lab coat with a full-sleeve moisture barrier, double-sets of gloves, eye protection, and an N95 (or better) dust mask should be donned prior to the bone tissue processing steps described below.

For the studies described in previous chapters, bone tissue processing began in the unembalmed cadaver lab after obtaining appropriate authorization from the Vanderbilt Anatomical Donation Program. Anterior surfaces of right and left femurs were exposed by dissecting surrounding muscle and fat, a task ideally performed by the morgue technicians. Then, 15-20 cm spans centered on the femoral midshafts were marked for cutting (a grease pencil was most effective for marking the bone *in situ* due to its high blood content). Femur shafts were cut with either a Stryker vibrating saw equipped with a semicircular blade or a Dewalt reciprocating saw equipped with a 6" rip blade, depending on availability. In practice, the vibrating saw generated considerable amounts of

bone dust and fine sprays but gave clean and controlled cuts, while the reciprocating saw gave rougher and faster cuts with less bone dust generation. Therefore, if these cuts are not intended to be final, the reciprocating saw was preferred. Frequently with both saws, it was not possible to cut entirely through the femurs if implant rods or underlying soft tissues provided too much obstruction. In these cases, it was necessary to manually fracture the partially cut femurs to separate them from the cadaver.

During cutting, it was important to keep track of bone orientation. Distal midshaft ends were wrapped in gauze immediately after excision, and right/left femurs were placed in appropriately labeled biohazard bags (note: make sure to bring large enough bags to accommodate entire midshafts). With knowledge of the femur's distal end and side of the body, it was straightforward to deduce medial, lateral, and anterior sides using the prominent posterior process. To maintain a record of femurs and processing steps, proximal and distal ends were traced onto white printer paper with pencil (more effective than pen/sharpie).

Although cadaverous tissue was typically stored for several weeks at 1-4°C prior to femoral midshaft extraction, care was taken to promptly place excised midshafts in ≈10 mL of 1x phosphate buffered saline and store them at -20°C for the short-term or at -80°C for the long term. This avoided unintentional

fluid loss. One freeze-thaw cycle typically separated initial femur harvesting and subsequent processing steps.

For the studies herein, pure cortical bone strips of ≈ 2 mm thickness and ≈ 70 mm length were required (width was limited by cortical thickness and was typically ≈ 5 mm). Strips were cut from intact midshafts using a diamond saw with custom-fabricated clamping vise (Fig AII.1).

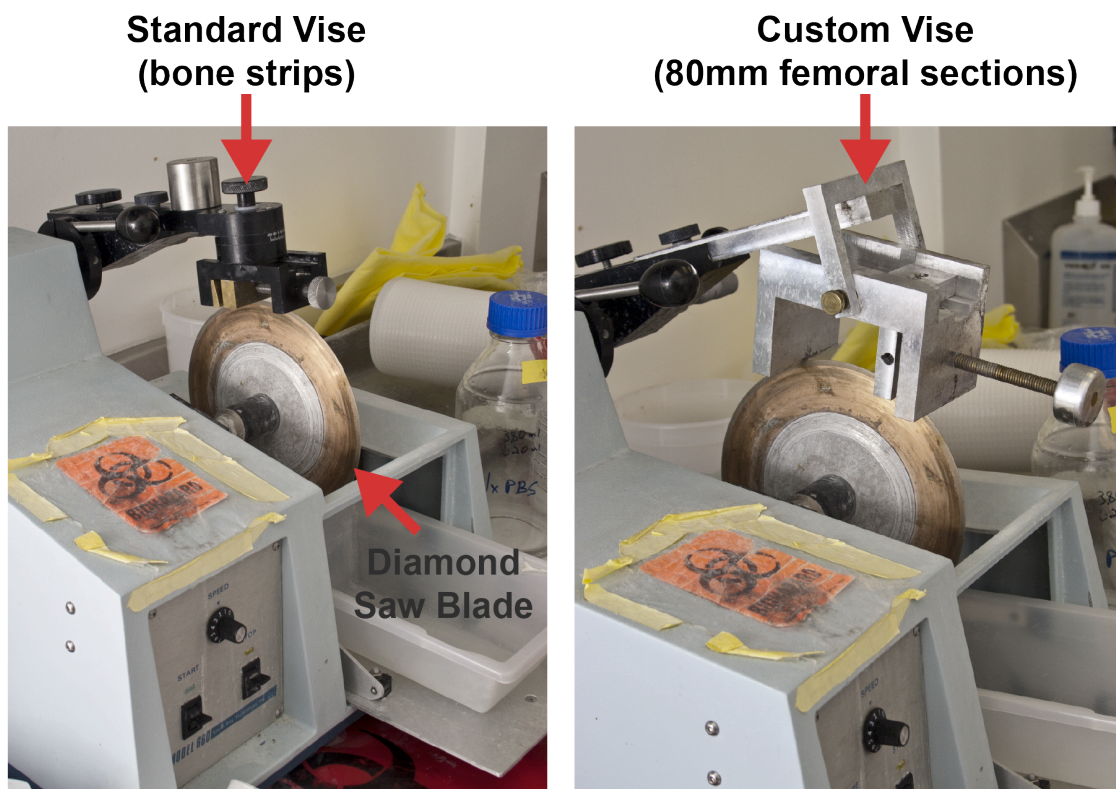


FIGURE AII.1 *Diamond saw setup.* Standard (left) and custom-fabricated vises (right) are shown mounted to the diamond saw. The water bath reservoir is visible beneath the blade and should always be filled with deionized water during cutting. During operation, care should be taken to avoid cutting into the vises, which will introduce aluminum powder into the bone specimen as well as degrade the vise edges. Saw blade speed should be minimized (settings 5-8) to avoid splashing, which can be contained with a plastic drape placed over the entire saw (not shown).

Since the vise and saw blade cutting depth only accommodated ≈ 80 mm-long spans, midshafts were first cut in half and were then mounted with the long axis parallel to the diamond blade. Two cuts were then made through the cortical wall, traversing the blade between cuts by 2 mm plus the blade width to form ≈ 2 mm-thick cortical bone strips. The standard clamping vise was subsequently used to mount and trim strips to the desired 70 mm length. These cutting steps were greatly facilitated by first removing the bone marrow, which allows the cutting blade to be easily visualized in the hollowed-out medullary cavity and avoid cutting into the opposing cortical wall. Marrow in thawed bones ranges in consistency from that of medium oil to that of toothpaste, and a lengthy spatula is usually required to remove innermost marrow.

Rough cortical bone strips formed by the diamond saw were machined to remove exterior periosteum and interior endosteum and to create uniform beams for mechanical testing. This machining was performed with a drill press-mounted 3/16" endmill bit and custom-fabricated router jig, described in Fig AII.

2. The jig traversed smoothly across the drill press table and was manually manipulated to address the cortical bone with the revolving endmill, similar to a router table setup. The endosteum was typically much rougher than the periosteum and was machined first, which placed the relatively flat periosteal

surface against the jig tenon for the first machining pass. The strip was reversed after the first pass to remove periosteum via a second pass. During machining, a drip of deionized water was maintained to avoid dust formation and provide cooling and lubrication.

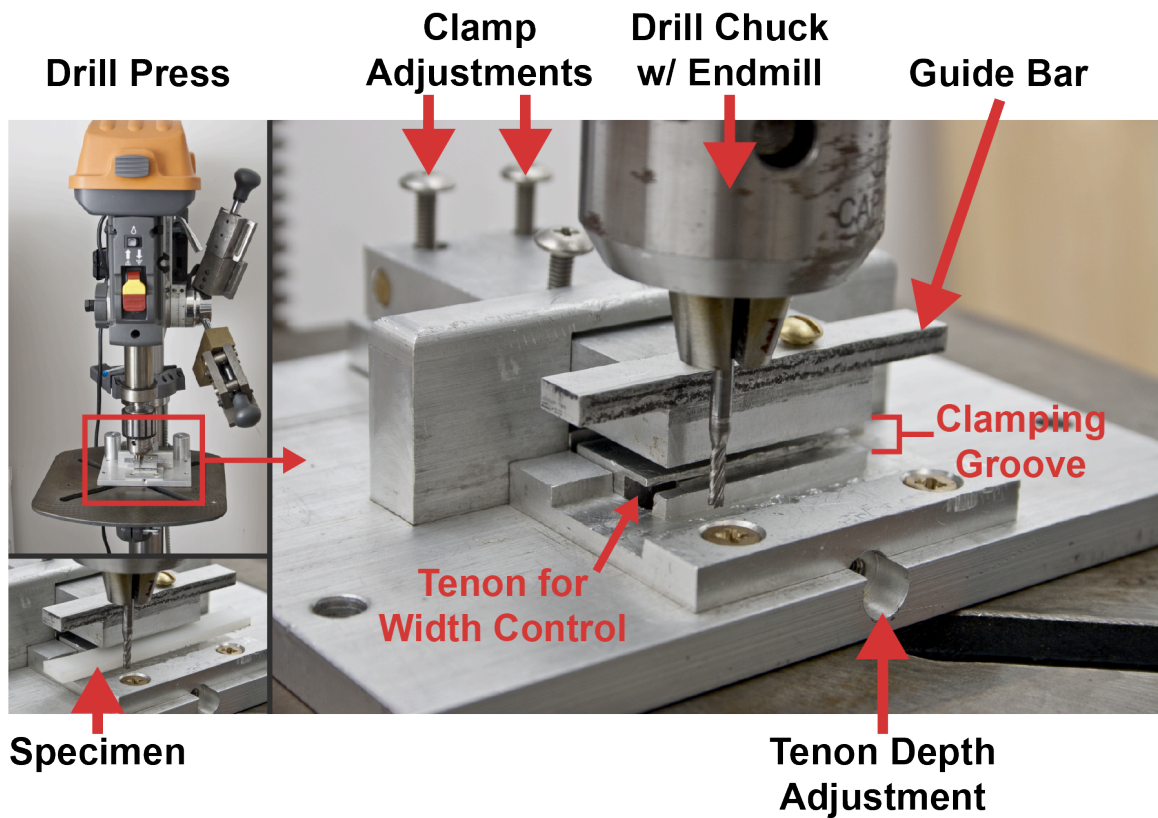


FIGURE AII.2 *Drill press setup.* A free-standing drill press (top, left) was used with a custom router jig (right) for machining uniform cortical bone beams. The jig was equipped with a guide bar, which engages the smooth shank of the endmill bit above its flutes to create a straight pass. The jig also contained a clamping mechanism, capable of accommodating 1-8 mm-thick strips. A tenon with adjustable depth was situated in the clamping groove (labeled above, right) to control the ultimate strip width. The jig is shown loaded with a white plastic beam at bottom left, representative of a cortical bone strip.

Final cortical bone strips were measured with digital calipers to verify beam uniformity. Deviations of 0.1 mm or less across full beam width and thickness were typically achieved with this machining setup. After machining, strips were packaged in saline-saturated gauze within 15 mL Falcon centrifuge tubes and placed in frozen storage.

As an alternative to the cadaver lab, the Musculoskeletal Tissue Foundation was a useful source of intact femurs. However, these tissues were rejected for implantation because of underlying pathology, so extra care should be taken with biosafety protocols. Processing intact femurs followed the steps described above, however joint endplates and bulk muscle tissue were first removed with an 8" bench top bandsaw. This cutting step is considerably easier if tissue is first frozen and clean-up proceeds before debris fully thaws. Frozen tissue did not require water lubrication if cutting was performed swiftly. As with any bandsaw, finger, hand, and forearm placement should be carefully and deliberately controlled to avoid the blade path.

APPENDIX III

Applying Cortical Bone Water Characterization Methods to Other Tissues: A Case Study of Myelinated Nerves

Recently developed uTE MRI techniques have enabled clinical imaging of short-lived ^1H NMR signals with $T_2 < 1$ ms in a variety of tissues. In previous chapters, these techniques were utilized to characterize human cortical bone from micro-anatomical and biomechanical bases. Previously, these techniques have also shown novel signal enhancement in myelinated tissues, although the source of this enhancement has not been identified. Herein, we report studies of the nature and origins of ultra-short T_2 (u T_2) signals ($50 \mu\text{s} < T_2 < 1$ ms) from amphibian and mammalian myelinated nerves. NMR measurements and comparisons with myelin phantoms and expected myelin components indicate that these u T_2 signals arise predominantly from methylene ^1H on/in the myelin membranes, which suggests that direct measurement of u T_2 signals can be used as a new means for quantitative myelin mapping.

AIII.1 — Background and Introduction

Quantitative myelin imaging is of widespread interest for both clinical and research studies of a number of neurological disorders, including Multiple

Sclerosis, Alzheimer's Disease, various leukodystrophies, and numerous psychiatric disorders. For almost two decades the MRI research community has pursued the development and experimental validation of quantitative myelin mapping, primarily through one of three approaches: diffusion tensor imaging (DTI), quantitative magnetization transfer (qMT), and multi-exponential T_2 (MET_2). In lieu of a detailed discussion of these efforts, we direct the reader to a comprehensive review article by Laule and colleagues (1). Briefly though, while DTI has great sensitivity to white matter microstructure, it has not been found to be specific to myelin. Both qMT and MET_2 have shown greater promise to be more specific, but neither has been widely adopted because of the remaining ambiguity in interpretation and difficulty of fast, multi-slice or 3D implementation. Another approach, which has thus far garnered relatively little attention, is the imaging of ultra-short T_2 (< 1 ms) signals using ultra-short Echo Time (uTE) imaging (2), or related methods (3,4). uTE methods have demonstrated relatively greater signal in white matter compared to gray (5,6), but no studies (to our knowledge) have yet evaluated the origins of this signal or its relationship to myelin. Presented here are 1H NMR measurements and isotopic perturbations on both central and peripheral nerves as well as on myelin phantoms, which were used to characterize and determine the biophysical

origins of ultra-short T_2 (uT_2) signals ($50 \mu\text{s} < T_2 < 1 \text{ ms}$) in myelinated tissue.

Results indicate that uTE MRI has promise as a specific measure of myelin content.

AIII.2 — Experimental Methods: NMR

^1H NMR measurements were performed at 200 MHz in a 31-cm horizontal bore 4.7T magnet, equipped with a Varian DirectDrive Console (Varian Medical Systems, Palo Alto, CA). An in-house built 10-mm diameter loop-gap RF coil with Teflon structural support and low background ^1H signal (similar to the lowest-proton design described in (7)), was used for all measurements.

The Carr-Purcell-Meiboom-Gill (CPMG) (8) pulse sequence was used to measure transverse relaxation in each sample with the following experimental parameters (based on a previous study of cortical bone (9)): 10000 echoes, 100 μs echo spacing (first echo at 100 μs), $\approx 6.5/13 \mu\text{s}$ ($90^\circ/180^\circ$) RF pulse durations, 40 μs signal acquisition time per echo, 15 s TR, 16 averaged excitations and a four-part $90_{(x,-x,x,-x)}/180_{(y,y,-y,-y)}$ phase cycling scheme. Free induction decays (FIDs) were also collected using $\approx 6.5 \mu\text{s}$ -duration 90° -pulse, 2.5 MHz bandwidth acquisition, 15 s TR, and 64 averaged excitations with a $90_{(x,y,-x,-y)}$ phase cycling scheme. After receiver dead time and coil ringing, the first FID sample was acquired 10.4 μs after the midpoint of the 90° -pulse.

From each CPMG acquisition, a T_2 spectrum was estimated by forming a linear system equating the signal (10,000 echoes) to a sum of 128 exponential functions (time constants log-spaced between 10 μ s and 1 sec), reducing the system dimension by singular value decomposition (10), then fitting exponential amplitudes in a non-negative least-squares sense and subject to a minimum curvature regularization (10,11). The regularization was adjusted to a conservative level by matching T_2 spectral features in the 10-300 ms range to those in previous studies (12,13). T_2^* spectra were estimated similarly from the first \approx 500 μ s of the FIDs and with time constants between 5 and 2000 μ s. Because previous studies of a model membrane system similar to myelin have demonstrated non-exponential free induction decays (FIDs) (14,15), (which would appear similarly in a CPMG measurement), non-exponential decay characteristics were also investigated in the deuterated myelin extract and phantom measurements. Fitted CPMG and FID components with T_2 (or T_2^*) $>$ 200 μ s were subtracted from the original signals to isolate the shortest-lived signal components, which were then fitted to a Gaussian function by nonlinear regression.

T_2 - T_2 relaxation exchange spectroscopy (REXSY) (16,17) was used to identify magnetization exchange between T_2 components, and was implemented

with the following experimental parameters: 15 s TR, 53 different CPMG preparation times pseudo log-spaced between 100 μ s and 1 s, a 200 ms mixing time, and a CPMG acquisition as described above (10000 echoes at 100 μ s echo spacing, etc). Four excitations were collected with a 2-step phase cycle of the storage pulse, resulting in a total scan time of \approx 60 min. REXSY echo magnitudes were reduced by singular-value decomposition prior to two-dimensional non-negative least squares fitting (18,19) to the aforementioned range of decaying exponentials, producing a so-called T_2 - T_2 spectrum.

All measurements were made at bore temperature (\approx 20°C) and all data processing (REXSY and CPMG) was performed using MATLAB (The Mathworks, Natick, MA) and the freely-available MERA_Toolbox (Multi-Exponential Relaxation Analysis, http://vuiis.vanderbilt.edu/~doesmd/MERA/MERA_Toolbox.html).

AIII.3 — Experimental Methods: Nerve Tissue Processing

Immediately following euthanasia, a pair of sciatic nerves were excised from each of three frogs (adult African clawed toads—*Xenopus laevis*) to characterize peripheral nerve, and a pair of optic nerves were excised from each of two rats (adult Sprague-Dawley) to characterize nerve more similar to the central nervous

system. All animal handling protocols were approved by the Vanderbilt University Institutional Animal Care and Use Committee.

From each frog, ≈ 20 mm of sciatic nerve was extracted from each hind limb using blunt dissection techniques. Samples were cleaned of blood and connective tissue and stored in buffered isotonic solutions. One nerve sample was placed in amphibian Ringer's solution (Fisher Scientific, Waltham, MA) and the other in a mixture of D_2O (99.9% isotopic purity, Sigma-Aldrich Corp., St. Louis, MO) and electrolytes (by mass proportion: 73 NaCl : 2 KCl : 1 $CaCl_2$: 2 $NaHCO_3$) consistent with amphibian Ringer's solution. From each rat, ≈ 5 mm from each optic nerve was extracted from a span between the skull and optic chiasm, cleaned of blood and connective tissue and stored in buffered isotonic solutions. One nerve sample was placed in a standard phosphate buffered saline (PBS) solution (Mediatech Inc., Manassas, VA) and the other in a deuterated solution made by mixing D_2O (above) with the appropriate mass PBS electrolyte tablets (MP Biomedicals, Solon, OH).

Both sciatic and optic nerve samples were maintained on a shaker table at $4^\circ C$ and agitated at 20 RPM. Periodically, over a three-hour duration, samples were removed from the buffer and placed in a 5-mm o.d. NMR tube filled with Fomblin (a 1H -free oil, Solvay Solexis, West Deptford, NJ) for CPMG

measurements (≈ 5 min). Following data collection, the samples were returned to the appropriate buffer. After three hours, the sciatic nerve samples that were stored in regular Ringer's solution were again placed in a 5-mm o.d. NMR tube filled with Fomblin for REXSY measurements (≈ 60 min).

AIII.4 — Experimental Methods: Tissue Phantom Preparations

In addition to the study of freshly excised nerve, three tissue phantoms were studied: I) a biologically-derived myelin extract phantom, II) a synthetic myelin lipid phantom, and IIIa/b) two protein phantoms. All tissue phantoms were prepared in both hydrated and deuterated states and studied with CPMG, as described above.

Phantom I, biologically-derived myelin extract, was formulated from bovine brain myelin extract as follows: Folch Fraction I (Type-I bovine brain extract, Sigma-Aldrich Corp., St. Louis, MO), an organophilic extract of predominantly myelin-related brain lipids (20), was lightly milled with mortar and pestle into a fine powder and lyophilized at 0.05 mBar for 24 hours to remove water and residual solvents. The remaining powder (50 mg) was then combined via high-speed vortexer with 35 μ L of either deionized water or D₂O, forming paste-like phantoms with the solid-liquid mass ratio = 3:2, as expected in physiological myelin.

Phantom II, synthetic myelin lipid, was formulated to approximate the non-protein portion of biological myelin, and consisted of 50% (w/w) deionized water (or D₂O), 13.5% cholesterol, 13% galactocerebroside, 19.3% phosphatidylcholine, and 4.2% sphingomyelin (all lipids obtained from Sigma-Aldrich Corp., St. Louis, MO). The solid lipid mixture (50 mg) was co-solvated in 150 μ L of a 2:1 (by volume) mixture of chloroform:methanol to uniformly incorporate all components. The resulting solution was then lyophilized for 48 hours to remove all solvents and residual water, and the recovered residue was combined with the appropriate amount of either water or D₂O via high-speed vortexer.

Two aqueous protein phantoms were prepared: Phantom IIIa consisted of 20% w/w Type-1 collagen, purified from bovine tendon (Sigma-Aldrich Corp., St. Louis, MO), and Phantom IIIb consisted of a gel of 20% w/w bovine serum albumin (99.9% purity, Sigma-Aldrich Corp., St. Louis, MO), crosslinked with 25 μ L/mL of 50% aq. glutaraldehyde (Electron Microscopy Sciences, Hatfield, PA).

AIII.5 — Experimental Findings

Typical T₂ spectra from nerve samples \approx 1.5 hr in control and deuterated buffer, and from tissue phantoms, in hydrated and deuterated states, are shown in Fig AIII.1.

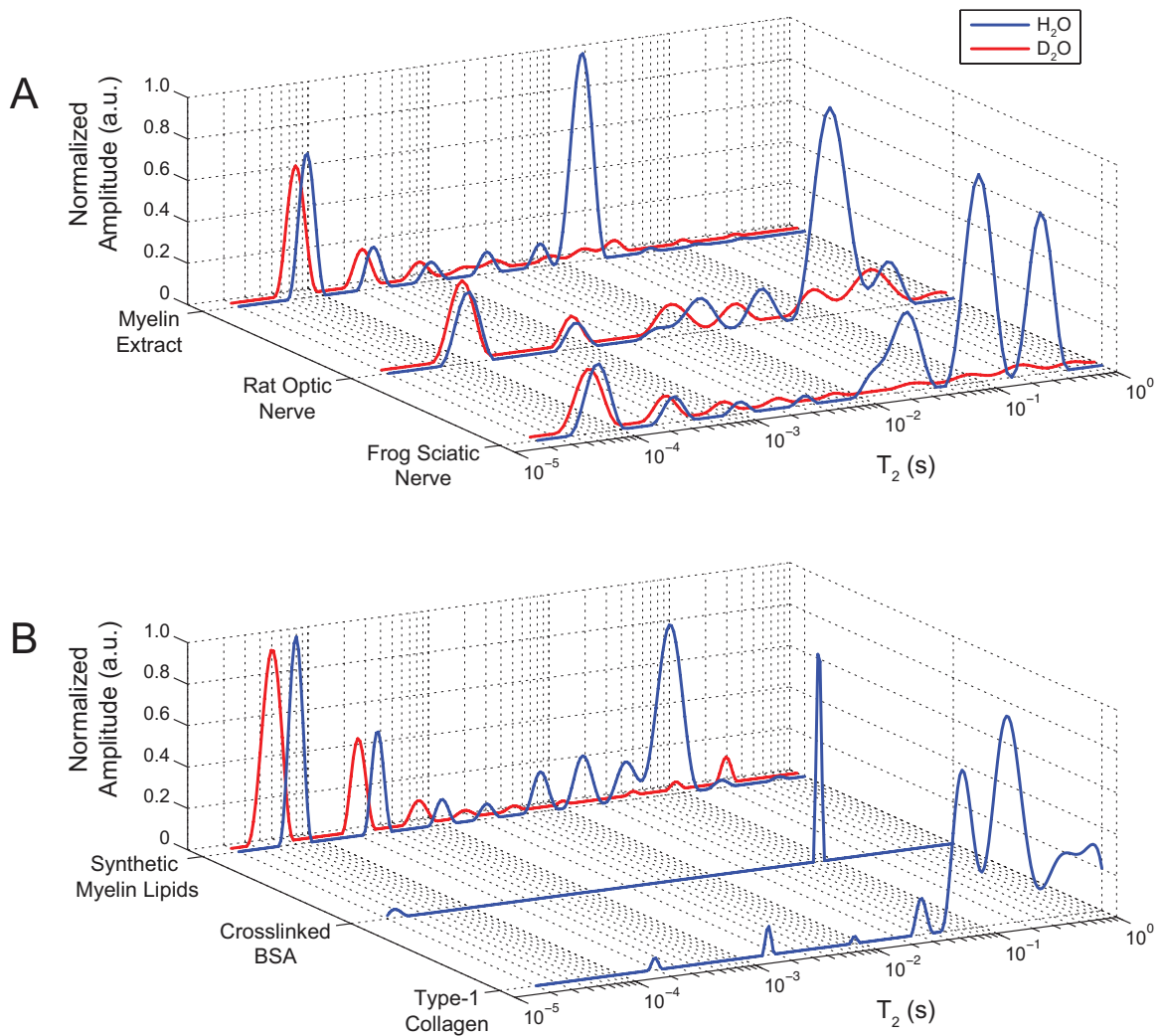


FIGURE AIII.1 *Representative T_2 spectra from:* biological sources (A) of frog sciatic nerve, rat optic nerve, and bovine brain myelin extract (Phantom I); and T_2 spectra from synthetic sources (B) of refined myelin lipids (Phantom II) and collagen/BSA proteins (Phantoms IIIa/b, respectively), in naturally abundant water (blue/black) or after prolonged D_2O immersion (red/gray). D_2O immersion dilutes 1H capable of chemical exchange with water, so only methylene 1H signals effectively survive D_2O immersion. In all sources except the pure protein phantoms (IIIa/b), a large μT_2 component (≈ 60 - 100 μs) was consistently observed with at least one other longer-lived μT_2 component. All μT_2 components effectively survived D_2O immersion and are attributed predominantly to methylene 1H . Long-lived T_2 s (> 1 ms) are attributed primarily to water 1H , in agreement with previous studies.

Note that although the vertical scales in Fig AIII.1 are in arbitrary units, we know from previous experience with this experimental set-up that the inter-sample variation in ^1H NMR signal amplitude between like samples is $\approx 5\%$ (9), so it is reasonable to compare spectra from control and deuterated samples on the same scale. Control nerve T_2 spectra are generally similar to previously published results for frog sciatic (12) and rat optic (13) nerve, with a few exceptions. Most importantly, previous studies did not investigate the sub-millisecond T_2 domain where Fig AIII.1 shows two signal components in both frog sciatic ($T_2 \approx 50 \mu\text{s}$ and $\approx 250 \mu\text{s}$) and rat optic nerve ($T_2 \approx 80 \mu\text{s}$ and $\approx 700 \mu\text{s}$) spectra. As also seen in Fig AIII.1, these uT_2 signals did not wash out during immersion of nerves in deuterated buffer, despite the loss of $\approx 95\%$ of frog sciatic nerve long- T_2 s ($>1 \text{ ms}$, as consistent with a previous study (21)) and $\approx 68\%$ of rat optic nerve long- T_2 s. Repeat CPMG measures during immersion confirmed that a steady-state condition was reached in frog sciatic nerve within the first 1.5 hr of D_2O immersion. The long- T_2 s in the rat optic nerve did not reach a clear steady-state within two hours of immersion, at which point the nerve had begun to visibly disintegrate, so one additional rat optic nerve was fixed in glutaraldehyde/formalin and followed over a 10-day period of D_2O immersion. These data (not shown) indicated that 82% of the initial long- T_2 s were removed by D_2O

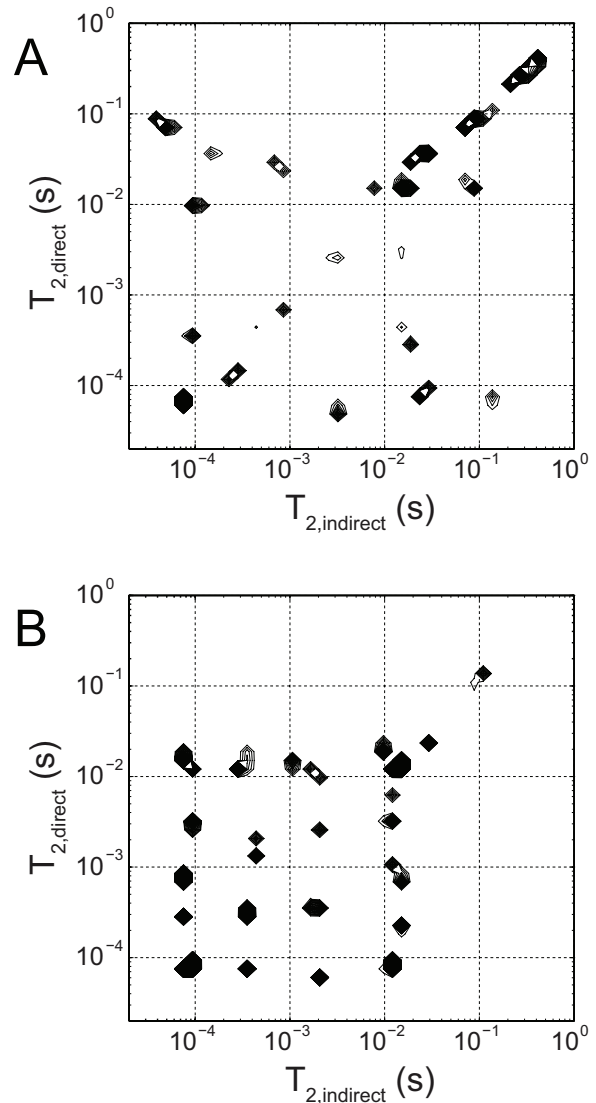
immersion, while uT_2 s remained unchanged. The remaining long T_2 signal from deuterated rat optic nerve was on the same order of magnitude as the known background signal from the coil and ambient water vapor (7), which is negligible compared to the much larger signals from the sciatic nerves and phantoms.

The resilience of the uT_2 signals in nerve to the deuterated buffers indicate that they are *not* derived from water protons or chemically-exchangeable amide/hydroxyl protons, but rather must predominantly arise from carbon-bound methylene protons. Similar uT_2 signal components which are also present in both hydrated and deuterated states, are seen in Phantom I (myelin extract) and Phantom II (myelin lipids), which suggests that myelin and/or other membrane lipids may be the source of these methylene protons which give rise to the uT_2 signals. Conversely, the absence of uT_2 components from Phantom III (protein solutions) suggests that tissue proteins are not a likely source. (Due to the absence of uT_2 signals, Phantom III preparations were not further studied in a deuterated state.)

Figure AIII.2 shows the T_2 - T_2 spectra from REXSY measurements of a frog sciatic nerve (representative of both frogs studied). Although this T_2 - T_2 spectrum is unregularized, it is readily apparent that the main diagonal is similar to the CPMG-derived T_2 spectrum from frog nerve in Fig AIII.1. The off-diagonal

components indicate exchange of magnetization between corresponding main-diagonal T_2 components during the 200 ms mixing period.

FIGURE AIII.2 T_2 - T_2 exchange spectroscopy (REXSY) spectra from frog sciatic nerve (A) and the bovine brain myelin extract phantom (B). In these contour plots of spectral intensity, components appearing on the main diagonal represent stationary ^1H that do not exchange with other sites during the REXSY mixing period. Off-diagonal cross-peaks indicate spins that undergo exchange between corresponding main-diagonal components and are labeled accordingly. Thus, in frog sciatic nerve, ^1H exchange occurs among uT_2 components and both the ≈ 25 ms (myelin water) and 90 ms (extra-axonal water) components. Exchange is also observed in the myelin extract phantom between uT_2 components and the main water T_2 (≈ 15 ms), indicating that myelin/water interactions may give rise to the majority of uT_2 -related exchange observed in myelinated frog nerve.



As such, Fig AIII.2 indicates exchange between the dominant uT_2 component and both the 25 ms and 90 ms T_2 components. Possible exchange between the 20 ms and the 90 ms T_2 components is indicated by the presence of one cross peak,

while the 300 ms component apparently does not exchange with any components on the timescale of the 200 ms mixing period. REXSY measurement of the myelin extract phantom (Fig AIII.2) also indicates magnetization exchange between its uT_2 and ≈ 15 ms T_2 water component.

Figure AIII.3A-C shows FID and CPMG signals (3A) and corresponding multi-exponential fits (3B) from the deuterated myelin extract (Phantom I). When stripped of long-lived components (T_2 or $T_2^* > 200 \mu\text{s}$), the signals fitted to both exponential and Gaussian functions are shown in Fig AIII.3C. These fits indicate that if the short-lived CPMG signal decayed according to a Gaussian function, then the exponential fitting used here could overestimate this component amplitude by as much as $\approx 2.5x$. However, the FID did not reveal such a prominent Gaussian decay characteristic and restricted this overestimation to $\approx 10\%$. The residual second moments from Gaussian fits did not exceed $1.1 \times 10^9 \text{ s}^{-2}$ across all nerves and myelin phantoms, which is consistent with a dipolar-broadened liquid crystalline lipid system (15). Such a system is theoretically described by a super-Lorentzian lineshape, as previously experimentally shown for non-aqueous signals from whole cells (14). The super-Lorentzian deviates from an exponential shape to a lesser extent than the Gaussian, so while it is generally inaccurate to model a dipolar-broadened spin system with exponential

basis functions, the inaccuracy in fitted signal amplitudes is small in this case. To be clear, we are not arguing that a dipolar-broadened non-aqueous tissue signal is theoretically described by Lorentzian lineshape. In Fig AIII.3D&E, FID data and exponential fits are shown for a representative sciatic nerve and phantoms, and it is clear that the sciatic nerve possesses a uT_2 component ($\approx 70 \mu\text{s}$) similar to the myelin phantoms, as well as shorter-lived component ($< 20 \mu\text{s}$) similar to the two protein phantoms.

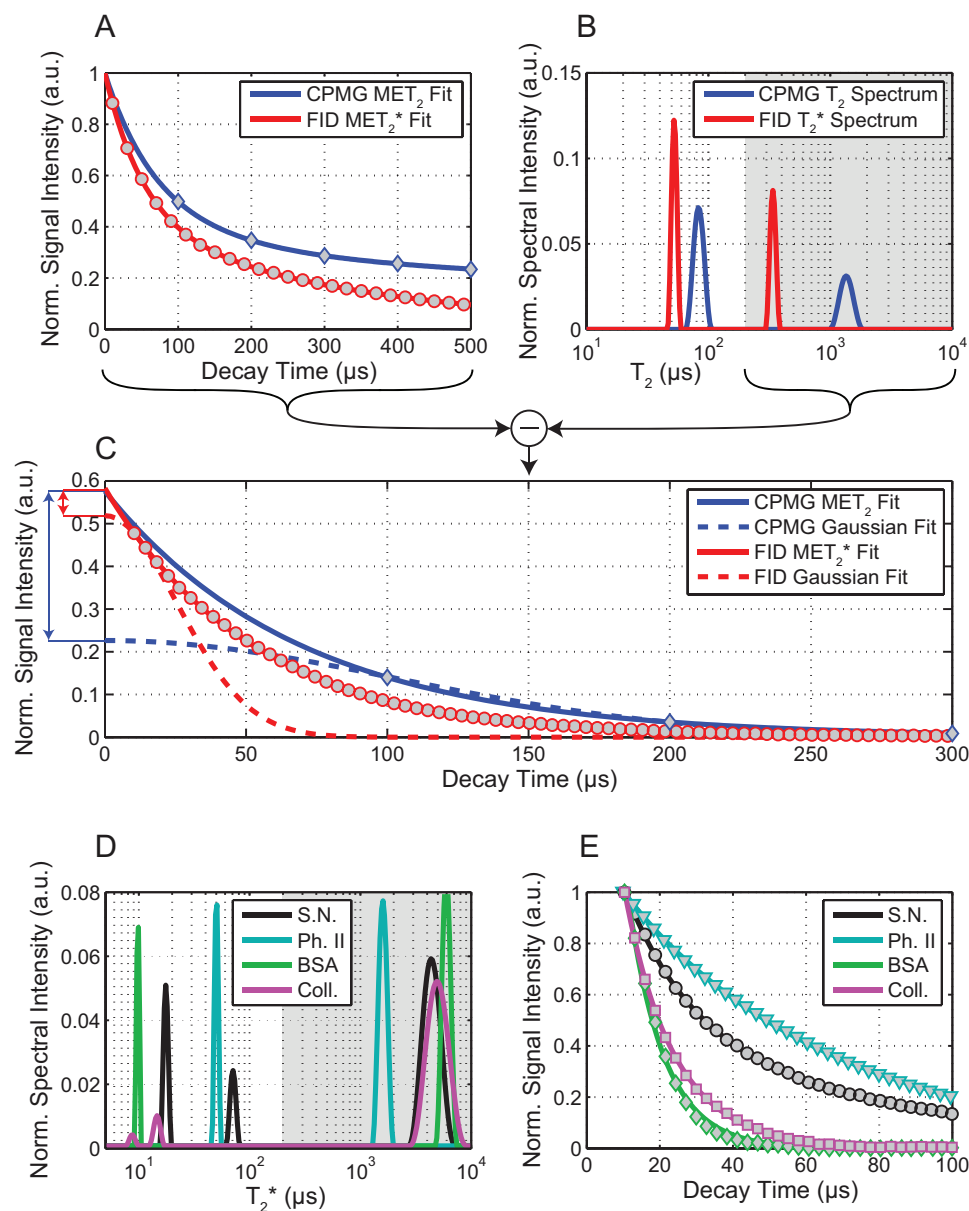


FIGURE AIII.3 *Rapid relaxation in myelin extract (A-C) and in sciatic nerve and phantoms (D,E).* (A) CPMG (diamonds) and FID (circles) signal magnitudes from deuterated Phantom I (myelin extract); multi-exponential fits are displayed as solid lines and (B) in the T_2 (or T_2^*) domain. Fitted long- T_2 (or T_2^*) components (gray: $T_2 > 200 \mu\text{s}$) were subtracted from the original data to isolate the (C) shortest-lived signals. Short-lived CPMG data were fitted with exponential (solid blue) and Gaussian (dashed blue) functions; the exponential fit overestimates the Gaussian signal amplitude by $\approx 2.5\times$ (blue arrow). Short-lived FID data were fitted with exponential (solid red) and Gaussian (dashed red) functions; the exponential fit overestimates the Gaussian signal amplitude by only $\approx 1.1\times$ (red arrow). (CPMG and FID signal amplitudes (A&C) are normalized to 1 at $t = 0$ for display purposes.) Multi-exponential fits of early FIDs from a sciatic nerve (S.N.), Phantom II (synthetic myelin lipid, Ph. II), BSA protein phantom, and collagen gel

phantom (Coll.) are shown in the T_2^* (D) and time (E) domains. As before, fitted long- T_2^* components (D, gray) have been subtracted from FIDs to isolate shortest-lived signals (E). Very short-lived decays ($T_2^* < 20 \mu\text{s}$) were seen in sciatic nerve and the protein phantoms, although such decays were clearly non-exponential. Additionally, a uT_2 component ($\approx 70 \mu\text{s}$) was observed in sciatic nerve, similar to the myelin phantoms I & II. (*FID amplitudes in (E) are normalized to 1 at the first datum for display purposes.*)

AIII.6 — Discussion: Ultrashort- T_2 s from the Myelin Membranes

In amphibian and mammalian myelinated nerves, previous studies have thoroughly characterized T_2 components with relaxation times greater than 1 ms, and our observations over this T_2 domain are in good agreement with these studies (12,13). In these, the $T_2 \approx 20$ ms component has been attributed to myelin water; consequently, in this study, signals with $1 \text{ ms} < T_2 < 50 \text{ ms}$ are defined as arising from myelin water. In contrast, uT_2 signals ($50 \mu\text{s} < T_2 < 1 \text{ ms}$) from myelinated tissues have not been well studied. Previous uTE imaging studies have demonstrated greater signal in white matter compared to grey matter (5,6), and numerous magnetization transfer (MT) studies have modeled white matter as having a greater reservoir of solid/semi-solid protons (typically modeled with $T_2 \approx 10 \mu\text{s}$) compared to grey matter (22-25), but, to our knowledge, no previous study has directly measured a range of sub-millisecond T_2 components and attempted to determine their biophysical origins. (Again, describing these signal

components with T_2 time constants is done for convenience and not to imply that they are truly governed by exponential decay functions.)

The finding that uT_2 components survive D_2O immersion in all nerves (Fig AIII.1) but still exchange magnetization with known water components on a 200 ms time scale (Fig AIII.2) indicates that uT_2 signals cannot predominantly arise from water or water-exchangeable 1H , including those found on mobile and bound water in the intra/extra-axonal or myelin spaces. If the uT_2 components were to arise from water, it is not conceivable how they could both survive D_2O immersion and directly exchange with water that is lost to D_2O immersion. Rather, we suggest that the nerve uT_2 signal primarily arises from the methylene 1H , for which there are two broad sources: phospholipid membranes and various intra- and extra-cellular proteins.

The biological myelin extract phantom (I) exhibited a similar methylene uT_2 1H signal to that found in the myelinated nerves (Figs AIII.1&3). This observation demonstrates that myelin is a source for the uT_2 signal, but does not itself discriminate lipid from protein sources, nor does it define the relative contribution of myelin to the uT_2 signal. Although known to be predominantly lipids, the exact chemical composition of Phantom I was not determined and thus it cannot be used to rule out a protein source. However, in comparing the

observations from Phantoms II and III, we see that both hydrated and deuterated lipids known to exist in myelin membrane exhibited uT_2 signals, while no such signal in the 50-1000 μs domain was found from either the Type-I collagen or BSA phantoms (Fig AIII.3D&E). Of course, there are many proteins in tissue, but collagen is representative of a large fraction of extra-cellular matrix proteins in nerve, and BSA is a common model for intra-axonal and membrane proteins. It is possible that methylene protons in nerve proteins contribute to an even shorter-lived $\approx 10 \mu s$ T_2 component, which has been previously characterized through MT measurements (22,23,25) and through wideline FIDs (24). As shown in Fig AIII.3, such a component was observed in the FIDs acquired from nerves and protein phantoms (III a/b) but not from the myelin extract (I) or lipid phantoms (II). Additionally, the deuterated forms of phantoms I and II were prepared from anhydrous starting materials, so their sizeable uT_2 signals cannot originate from a trapped water compartment that is D_2O -inaccessible. Combining this with the noted uT_2 similarities between nerves and phantoms I/II further suggests that the nerve uT_2 s do not arise from water. With these findings, we conclude that the uT_2 signal from nerve is predominately derived from membrane lipids.

To evaluate the relative contribution of myelin to the uT_2 signal, consider the relative sizes of the uT_2 and myelin water signals. In both sciatic and optic

nerve, the methylene uT_2 signal is approximately equal to the size of the myelin water signal (Fig AIII.1 and Table AIII.1). While there is no known source of lipid outside the myelin that alone can account for such a significant tissue volume, it is possible that some uT_2 signal is derived from non-myelin lipid sources. These sources include plasma and organelle membranes, which represent a minor fraction of the total lipid content in myelinated nerve, so we expect the observed uT_2 signals in myelinated nerves to be strongly myelin-specific.

TABLE AIII.1 *Observed uT_2 1H signal size in myelinated nerves and myelin extract, compared to expected mammalian myelin membrane 1H content.* Total observed uT_2 1H and expected 1H are normalized to the 1H content of myelin water and are also subdivided into non-methylene (D_2O -exchanging) and methylene portions. Total expected myelin membrane 1H is further divided into lipid and protein components. It is apparent that observed uT_2 signals are similar in size to the 1H pools expected in myelin lipids and bulk myelin (see Fig AIII.3). Nerve results are reported as mean \pm one standard deviation across all three frogs or as the range for both rats.

	1H Source	$[^1H] / [Myelin\ water\ ^1H]$		
		<i>Total</i>	<i>Non-Methylene</i>	<i>Methylene</i>
Observed NMR uT_2 Signals	Frog Sciatic Nerve	1.01 \pm 0.07	0.03 \pm 0.04	0.98 \pm 0.11
	Rat Optic Nerve	1.09 - 1.13	< 0.01	\approx 1.09 - 1.13
	Bovine Brain Myelin Extract	1.12	0.01	1.11
Expected Myelin Membrane 1H	Myelin Lipids	1.14	0.07	1.07
	Myelin Proteins	0.21	0.07	0.14
	Total Myelin Membrane	1.35	0.14	1.21

Additionally, because the chemical composition of myelin has been well studied, the postulate of a uT_2 myelin methylene proton origin can be evaluated by comparing the relative sizes of observed uT_2 and myelin water signals to the expected relative amounts of myelin membrane-associated 1H and myelin water. To this end, the 1H content of model myelin can be estimated from established compositional information. Assume i) that myelin contains 40% water and 60% solids (by mass) (1,26); ii) that the solid portion of myelin contains 20% protein and 80% lipids (by mass) (1,26); iii) the composition of the protein portion to be a 3:5 mixture (by mass) (1) of myelin basic protein ($C_{471.3}H_{834.8}N_{152}O_{142.7}S_{1.2}$ with 304.5 non-methylene 1H) and proteolipid protein ($C_{486.5}H_{846.1}N_{115.8}O_{138.9}S_{5.9}$ with 256.7 non-methylene 1H), respectively (non-stoichiometric empirical formulas are derived from bovine myelin shown in (27)); and, iv) from (26), the composition of the lipid portion to be: 27% cholesterol ($C_{27}H_{46}O$ with one non-methylene 1H), 26% gangliosides (assume GM1: $C_{73}H_{131}N_3O_{31}$ with 20 non-methylene 1H), 20% phosphatidylethanolamine ($C_{37}H_{75}NO_8P$ with four non-methylene 1H), 10% phosphatidylcholine ($C_{40}H_{81}NO_8P$ with one non-methylene 1H), 8.5% phosphatidylserine ($C_{38}H_{74}NO_{10}P$ with four non-methylene 1H), and 8.5% sphingomyelin ($C_{38}H_{78}N_2O_6P$ with three non-methylene 1H); palmitate fatty acids were assumed for the phosphatidyl- and sphingomyelin structures.

Then, from this model myelin composition, the relative proportions of each myelin component's expected ^1H pool size were derived and are shown in Fig AIII.4. From these proportions, it is straightforward to calculate the expected ratio of myelin methylene ^1H to myelin water (≈ 1.21 , Table AIII.1), which is similar to the observed values of ≈ 1.11 (bovine myelin extract), ≈ 1.12 (rat optic nerve) and ≈ 0.98 (frog sciatic nerve). Further, if we consider only the lipid contribution, as argued by observations from Phantoms I-III, this expected ratio drops from 1.21 to 1.07, which is even closer to the observed ratios and further suggests that proteins do not significantly contribute to the uT_2 signals. Hence, the assertion that the uT_2 signal from nerve is predominantly due to myelin is consistent with the comparison of the uT_2 signal amplitude and the known composition of myelin. And, while the reported uT_2 signal sizes are subject to experimental error and possible modest overestimation due to non-exponential decay characteristics (see Fig AIII.3), there are clearly *enough* methylene ^1H in myelin membranes to account for the observed uT_2 signal sizes.

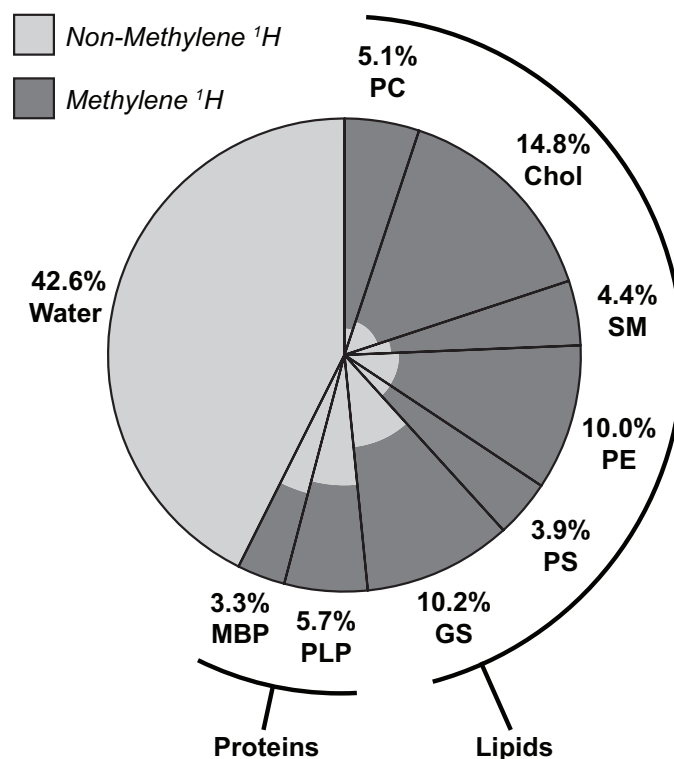


FIGURE AIII.4 *Expected biological myelin ^1H fractions, by molecular source.* Clockwise, lipid ^1H sources are phosphatidylcholine (PC), cholesterol (Chol), sphingomyelin (SM), phosphatidylethanolamine (PE), phosphatidylserine (PS), and gangliosides (GS); protein sources are proteolipid proteins (PLP) and myelin basic protein (MBP); finally, the water source includes surface-bound and interstitial membrane water. Light and dark shading indicate the portions of each molecular source representing non-methylene and methylene ^1H , respectively. For example, 5.1% of total myelin ^1H is found on phosphatidylcholine, which is predominantly methylene ^1H . In bulk myelin, there is a similar amount of expected methylene ^1H (all darkly-shaded regions) as compared to myelin water ^1H , which is reported in Table AIII.1.

Results from REXSY measurements offer further insight into the nature of the uT_2 signals components in nerve. REXSY spectra (Fig AIII.2) from both sciatic nerve and myelin extract demonstrate exchange of magnetization between the uT_2 signal and the myelin water signal (as well as some longer-lived T_2 components in nerve). This exchange must be mediated at some point by a

through-space dipolar interaction, since the methylene ^1H responsible for uT_2 signals will not chemically exchange with water ^1H . Previous work has demonstrated such an interaction between methylene ^1H and water (28). However, other studies have presented compelling evidence that commonly observed MT in myelinated tissue is mediated by chemical exchange of water protons with head-group $-\text{OH}$ protons on cholesterol (29) and, more significantly, on membrane lipids such as galactocerebroside (30). We postulate that the relatively large membrane lipid methylene ^1H pool, responsible for the uT_2 signal, acts as a spin reservoir that supplies the less abundant surface $-\text{OH}$ proton pool with magnetization via spin diffusion from the membrane interior to the water-accessible surface groups. The extent to which this magnetization exchange pathway contributes the commonly observed MT contrast in white matter is not clear, but the REXSY observations indicate that a two-pool MT model containing a $T_2 \approx 10 \mu\text{s}$ solid ^1H pool as the only submillisecond- T_2 species is probably incomplete for characterizing MT in myelinated tissue.

In comparison to other myelin imaging methods, quantitative imaging of the uT_2 signal is potentially more myelin-specific and easier to measure. As noted above, the uT_2 signal likely contributes to qMT measures of the solid pool size (M_{0b}), but it is additional to and distinct from the $T_2 \approx 10 \mu\text{s}$ signal, which was

observed in FIDs from whole nerve but not myelin extract. This suggests that the uT_2 signal is derived from a sub-set—possibly more myelin-specific—of spins that contribute to M_{0b} , and simple two-compartment modeling (semisolid & liquid spin pools) may be inadequate. Also, current qMT methods require several acquisitions and non-linear signal modeling, e.g., (25,31), but the similarity between T_2 and T_2^* spectra from myelin extract (Fig AIII.3b) indicates that the uT_2 signal ($T_2 \approx 50\text{-}150 \mu\text{s}$) is accessible to standard uTE methods with minimal signal processing. In comparison to myelin water fraction (MWF) derived from multi-exponential analysis of water signal (32), it is much easier in principle to distinguish a uT_2 signal from tissue water signals ($T_{2s} = 10\text{-}100 \text{ ms}$) than it is to distinguish “myelin water” ($T_2 \approx 20 \text{ ms}$) from non-myelin water ($T_2 \approx 80 \text{ ms}$). Also, the much shorter T_2 of the uT_2 signal makes its amplitude less sensitive to magnetization exchange with other spin pools. Inter-compartmental water exchange, as affected by myelin thickness, appears to contribute to the MWF in rat spinal white matter (33), although the effect in brain remains unknown. Ultimately, the relationship between the uT_2 signal and other MRI measures of myelin, and to myelin content and structure itself, will require further studies.

AIII.7 — Conclusions

In summary, methylene ^1H NMR signals with $T_2 = 50 \mu\text{s}$ to 1 ms and similar in amplitude to the myelin water signal ($T_2 = 10\text{-}50 \text{ ms}$) are reported in both amphibian and mammalian myelinated nerves. Combined evidence from ^1H isotopic manipulation, relaxation-based exchange spectroscopy, and measurements of multiple tissue phantoms indicates that these signals predominantly originate from methylene ^1H on/in the myelin membranes. As such, the uT_2 signals likely provide a direct measure of myelin content that is more accessible than the myelin water signal because of T_2 isolation. We expect the uT_2 signals reported herein to be present in all myelinated tissues, and it is likely that such signals are the source of previously reported white matter contrast enhancement in uTE images.

AIII.8 — Acknowledgements

The authors would like to acknowledge financial support from the NIH, Grant # EB001744, and the NSF, Grant # 0448915, as well as useful conversations with Dr. Alex L. MacKay, Dr. Daniel F. Gochberg and Dr. Elizabeth A. Louie.

AIII.9 — References

1. Laule C, Vavasour IM, Kolind SH, Li DKB, Traboulsee TL, Moore GRW, MacKay AL. Magnetic resonance imaging of myelin. *Neurotherapeutics* 2007;4(3):460-484.
2. Robson MD, Gatehouse PD, Bydder M, Bydder GM. Magnetic resonance: An introduction to ultrashort TE (UTE) imaging. *J Comput Assist Tomogr* 2003;27(6):825-846.
3. Wu YT, Ackerman JL, Chesler DA, Graham L, Wang Y, Glimcher MJ. Density of organic matrix of native mineralized bone measured by water- and fat-suppressed proton projection MRI. *Magn Reson Med* 2003;50(1):59-68.
4. Idiyatullin D, Corum C, Park JY, Garwood M. Fast and quiet MRI using a swept radiofrequency. *Journal of Magnetic Resonance* 2006;181(2):342-349.
5. Gatehouse PD, Bydder GM. Magnetic resonance imaging of short T-2 components in tissue. *Clinical Radiology* 2003;58(1):1-19.
6. Waldman A, Rees JH, Brock CS, Robson MD, Gatehouse PD, Bydder GM. MRI of the brain with ultra-short echo-time pulse sequences. *Neuroradiology* 2003;45(12):887-892.
7. Horch RA, Wilkens K, Gochberg DF, Does MD. RF Coil Considerations for Short-T₂ MRI. *Magn Reson Med* 2010;64(6):1652-1657.
8. Meiboom S, Gill D. Modified Spin-Echo Method for Measuring Nuclear Relaxation Times. *Review of Scientific Instruments* 1958;29(8):688-691.
9. Horch RA, Nyman JS, Gochberg DF, Dortch RD, Does MD. Characterization of ¹H NMR Signal in Human Cortical Bone for Magnetic Resonance Imaging. *Magn Reson Med* 2010;64(3):680-687.
10. Lawson CL, Hanson RJ. Solving least squares problems. Philadelphia: SIAM; 1995. xii, 337 p. p.
11. Whittall KP, Mackay AL. Quantitative interpretation of NMR relaxation data. *Journal of Magnetic Resonance* 1989;84(1):134-152.
12. Does MD, Beaulieu C, Allen PS, Snyder RE. Multi-component T-1 relaxation and magnetisation transfer in peripheral nerve. *Magn Reson Imaging* 1998;16(9):1033-1041.
13. Bonilla I, Snyder RE. Transverse relaxation in rat optic nerve. *Nmr Biomed* 2007;20(2):113-120.

14. Bloom M, Holmes KT, Mountford CE, Williams PG. Complete Proton Magnetic Resonance in Whole Cells. *Journal of Magnetic Resonance* 1986;69(1):73-91.
15. MacKay AL. A proton NMR moment study of the gel and liquid-crystalline phases of dipalmitoyl phosphatidylcholine. *Biophys J* 1981;35(2):301-313.
16. Lee JH, Labadie C, Springer CS, Harbison GS. Two-dimensional inverse Laplace transform NMR: altered relaxation times allow detection of exchange correlation. *J Am Chem Soc* 1993;115:7761-7764.
17. Callaghan PT, Arns CH, Galvosas P, Hunter MW, Qiao Y, Washburn KE. Recent Fourier and Laplace perspectives for multidimensional NMR in porous media. *Magn Reson Imaging* 2007;25(4):441-444.
18. English AE, Whittall KP, Joy MLG, Henkelman RM. Quantitative 2-dimensional time correlation relaxometry. *MagnResonMed* 1991;22(2):425-434.
19. Venkataramanan L, Song YQ, Hurlimann MD. Solving Fredholm integrals of the first kind with tensor product structure in 2 and 2.5 dimensions. *Ieee Transactions on Signal Processing* 2002;50(5):1017-1026.
20. Folch J. Brain cephalin, a mixture of phosphatides. Separation from it of phosphatidyl serine, phosphatidyl ethanolamine, and a fraction containing an inositol phosphatide. *Journal of Biological Chemistry* 1942;146(1):35-44.
21. Wachowicz K, Snyder RE. Assignment of the T-2 components of amphibian peripheral nerve to their microanatomical compartments. *Magn Reson Med* 2002;47(2):239-245.
22. Morrison C, Henkelman RM. A Model for Magnetization-Transfer in Tissues. *Magn Reson Med* 1995;33(4):475-482.
23. Stanisz GJ, Kecojevic A, Bronskill MJ, Henkelman RM. Characterizing white matter with magnetization transfer and T-2. *Magn Reson Med* 1999;42(6):1128-1136.
24. Bjarnason TA, Vavasour IM, Chia CLL, MacKay AL. Characterization of the NMR behavior of white matter in bovine brain. *Magn Reson Med* 2005;54(5):1072-1081.
25. Gochberg DF, Gore JC. Quantitative magnetization transfer imaging via selective inversion recovery with short repetition times. *Magn Reson Med* 2007;57(2):437-441.
26. Gennis RB. *Biomembranes : molecular structure and function*. New York: Springer-Verlag; 1989. xvii, 23 p.

27. Greenfield S, Brostoff S, Eylar EH, Morell P. Protein composition of myelin of the peripheral nervous system. *Journal of Neurochemistry* 1973;20(4):1207-1216.
28. Gore JC, Brown MS, Armitage IM. An analysis of magnetic cross-relaxation between water and methylene protons in a model system. *Magn Reson Med* 1989;9(3):333-342.
29. Koenig SH. Cholesterol of myelin is the determinant of gray-white contrast in MRI of brain. *Magn Reson Med* 1991;20(2):285-291.
30. Kucharczyk W, Macdonald PM, Stanisiz GJ, Henkelman RM. Relaxivity and magnetization transfer of white matter lipids at MR imaging: importance of cerebroside and pH. *Radiology* 1994;192(2):521-529.
31. Sled JG, Pike GB. Quantitative imaging of magnetization transfer exchange and relaxation properties in vivo using MRI. *Magn Reson Med* 2001;46(5):923-931.
32. Mackay A, Whittall K, Adler J, Li D, Paty D, Graeb D. In vivo visualization of myelin water in brain by magnetic resonance. *Magn Reson Med* 1994;31(6):673-677.
33. Dula AN, Gochberg DF, Valentine HL, Valentine WM, Does MD. Multiexponential T2, magnetization transfer, and quantitative histology in white matter tracts of rat spinal cord. *Magn Reson Med* 2010;63(4):902-909.